Dissertation

submitted to the

Combined Faculties of Natural Sciences and Mathematics

of the Ruperto-Carola University of Heidelberg, Germany

for the degree of

Doctor of Natural Sciences

Put forward by

David E. Sosa Corral

Born in: Chihuahua, Mexico

Oral Examination: November 2, 2016

Search for New Physics in the Fully Hadronic $t\bar{t}$ Channel at $\sqrt{s} = 13$ TeV with the ATLAS Detector at the LHC

Referees: Prof. Dr. André Schöning

Prof. Dr. Tilman Plehn

Abstract

A search for heavy resonances where two high transverse momentum top quarks decay hadronically and produce two large jets is carried out using data collected with the ATLAS Detector at the Large Hadron Collider during 2015 at $\sqrt{s} = 13$ TeV. The HEPTopTagger algorithm is used to reconstruct the $t\bar{t}$ invariant mass and to reduce the large multijet background. The large jets must contain exactly one b-tagged jet. The b-tagging performance is studied with track and calorimeter jets. The use of track jets for b-tagging increases the $t\bar{t}$ invariant mass tagging efficiency by a factor between 1.3 and 2 and $S/\sqrt{B}$ by 40%. After the HEPTopTagger application, large jets where a top quark candidate is found, are cleaned from underlying event and pile-up activity and used for the $t\bar{t}$ invariant mass reconstruction. Using the cleaned large jets instead of the top quark candidate improves the $t\bar{t}$ invariant mass resolution. The multijet production is estimated using control regions in data. The $t\bar{t}$ invariant mass distribution is compared for data and Monte Carlo simulation and no significant deviations from the Standard Model predictions are found. Upper limits are set on the production cross section times branching fractions of Z' bosons resonances with masses between 0.75 TeV and 1.65 TeV at 95% C.L. Expected upper limits using an integrated luminosity of 11.5 fb^{-1} collected during 2016 are set on the production cross section times branching fractions of Z' boson with masses between 0.83 TeV and 2.37 TeV at 95% C.L.

Kurzfassung

Eine Suche nach schweren Resonanzen die zu Top Quarks mit hohem Transversalimpuls zerfallen und dabei zwei große Jets erzeugen wird vorgestellt. Sie basiert auf Daten die mit dem ATLAS Detektor am Large Hadron Collider während der Proton-Proton Kollisionen im Jahr 2015 bei $\sqrt{s} = 13$ TeV aufgenommen wurden. Der HEPTopTagger Algorithmus wird verwendet um das $t\bar{t}$ System zu rekonstruieren und den großen Multijet-Untergrund zu reduzieren. Die großen Jets müssen genau einen kleinen Jet mit einem b-tag enthalten. Die Leistugsfähigkeit des b-taggings wird mit Spur- und Kalorimeter-Jets untersucht. Die Verwendung von Spur-Jets für b-tagging erhöht die Selektionseffizienz $t\bar{t}$ invariante Masse um den Faktor zwischen 1.3 und 2 und $S/\sqrt{B}$ um 40%. Nach Anwendung des HEPTopTaggers werden die großen Jets, in denen ein Top-Quark-Kandidat gefunden wurde, von "Underlying Event" und Pile-up Aktivität bereignit und für die $t\bar{t}$ invariante Masse verwendet. Die Verwendung der bereinigten großen Jets verbessert die $t\bar{t}$ invariante Masse Auflösung. Der Multijet-Untergrund wird aus Kontrollregionen in Daten ermittelt. Die $t\bar{t}$ invariante Massverteilung für Daten und Monte Carlo Vorhersage wird verglichen und keine signifikante Abweichung von Standard Modell werden gefunden. Grenzwerte werden auf das Produkt aus Wirkungsquerschnitt und Verzweigungsverhältnis von der Z'-Boson gesetzt. Die Erzeugung von Z'-Bosonen mit einer Masse zwischen 0.75 TeV und 1.65 TeV wird mit 95% C.L. ausgeschlossen. Erwartete Grenzwerte bei einer Integrierte Luminosiät von 11.5 fb^{-1} mit Bedingungen der 2016 Datenhame werden gesetzt. Der erwartete ausgeschlossen Massenbereich liegt zwischen 0.83 TeV und 2.37 TeV mit 95% C.L.

Contents

1 Introduction **1**

2 Theoretical Context **2**

2.1 The Standard Model of Particle Physics 2

2.2 The Electromagnetic Interaction 3

2.3 The Strong Interaction 6

2.4 The Weak Interaction 7

2.4.1 The Electroweak Theory 8

2.5 The CKM Matrix 9

2.6 The Top Quark in the Standard Model 10

2.6.1 Introduction 10

2.6.2 Top Pair Quark Production 10

2.6.3 Top Quark Decay 11

2.7 Beyond the Standard Model 12

2.7.1 Technicolor 14

3 The Large Hadron Collider **16**

3.1 Introduction 16

3.2 Luminosity 18

3.3 Pile-Up 21

3.4 Phenomenology of *pp* collisions 22

3.4.1 Parton Density Functions and Factorization 24

3.4.2 Parton Showers 26

3.4.3 Hadronization 27

3.4.4 Underlying Event 28

3.5 Monte Carlo Generators 28

4 The ATLAS Detector **30**

4.1 Introduction . . . 30

4.2 Magnet System . . . 32

4.3 Inner Detector . . . 32

4.3.1 Pixel Detector . . . 33

4.3.2 Insertable *B*-Layer . . . 34

4.3.3 Semiconductor Tracker . . . 35

4.3.4 Transition Radiation Tracker . . . 35

4.4 Calorimeters . . . 36

4.4.1 Electromagnetic Calorimeters . . . 37

4.4.2 Hadronic Calorimeters . . . 38

4.5 Muon Spectrometer . . . 38

4.5.1 Track Reconstruction . . . 39

4.5.2 Fast Muon Chambers . . . 40

4.6 Luminosity Determination and Forward Subdetectors . . . 41

4.7 Trigger and Data Acquisition . . . 43

4.8 The ATLAS Simulation . . . 45

4.9 The ATLAS Fast Simulation . . . 46

4.10 Computing LHC Data . . . 46

5 ATLAS Reconstruction and Performance **48**

5.1 Tracks and Vertices . . . 48

5.2 Electrons . . . 49

5.3 Muons . . . 50

5.4 Jets . . . 51

5.5 *b*-jets . . . 53

5.5.1 Identification . . . 53

5.5.2 Calibration . . . 57

5.6 Missing Energy . . . 57

6 The HEPTopTagger **59**

6.1 Jets and Jet Substructure . . . 59

6.1.1 Sequential Recombination Algorithms . . . 59

6.1.2 Boosted Physics and Jet Substructure . . . 62

6.1.3 Trimming . . . 63

6.1.4 Filtering . . . 64

6.2 The HEPTopTagger Algorithm . . . 64

6.2.1 HEPTopTagger Steps . . . 66

6.2.2 Improved $m_{t\bar{t}}$ Reconstruction . . . 69

6.3 Other Top-tagging Approaches . . . 70

6.3.1 Substructure-variable taggers . . . 71

7 HEPTopTagger Performance at ATLAS **73**

7.1 Event Selection . . . 73

7.2 HEPTopTagger Top Tagging Efficiency . . . 74

7.3 HEPTopTagger Mistag Rate . . . 78

7.4 MC-only Top Tagging Performance . . . 84

7.5 Conclusion . . . 87

8 Fully Hadronic $t\bar{t}$ Resonance Search **91**

8.1 Introduction . . . 91

8.2 Improvements . . . 92

8.2.1 b-tagging with Track Jets . . . 92

8.2.2 $m_{t\bar{t}}$ Reconstruction with Filtered C/A R=1.5 jets . . . 94

8.3 Event Selection . . . 96

8.4 Multijet Estimate . . . 98

8.5 Control Distributions . . . 101

8.6 Systematic Uncertainties . . . 107

8.6.1 b-tagging . . . 107

8.6.2 Luminosity . . . 109

8.6.3 Jet Energy Scale and Resolution . . . 111
8.6.4 Multijet Estimate Uncertainty . . . 112
8.6.5 $t\bar{t}$ Cross Section Uncertainty . . . 112
8.6.6 Hard Scatter Generation . . . 113
8.6.7 Parton Shower Model . . . 113
8.6.8 Initial and Final State Radiation . . . 113
8.6.9 Parton Distribution Function . . . 114
8.6.10 Higher Order Electroweak Correction . . . 114
8.7 Resuls . . . 117
8.7.1 Expected Limits with 2016 data . . . 124

9 Conclusion and Outlook **129**

A Systematic Smoothing **132**

1 Introduction

The Standard model of Particle Physics is a framework which describes elementary particles and their interactions. Since its final formulation, the Standard Model has predicted the existence of many particles and achieved an experimental precision unmatched in any other areas of scientific inquiry. Despite its outstanding successes, several mysteries remains. These include, dark matter, the hierarchy problem, neutrinos with masses, etc. These mysteries are the main motivation for building machines complex as the Large Hadron Collider and the ATLAS experiment and looking for New Physics and new undiscovered phenomena.

The structure of this thesis proceeds as follows. Section 2 presents a detailed overview of the Standard Model with all its particular components. The most recent measurements carried out by the ATLAS detector are discussed. Our main character in this thesis, the top quark is introduced. The particular New Physics model studied for this thesis, the top-color assisted technicolor Z' boson is also introduced. An overview of the Large Hadron Collider, the instrument used to smash proton against each other at the highest-ever reached energies is given in Section 3 along with a review of the phenomenology of proton-proton interactions. The ATLAS experiment, detailed in Section 4, is the complex instrument used to look at the aftermath of the proton-proton collision. Particles passing through the ATLAS detector deposit energy which in turn are converted into raw electrical signals. The reconstruction of physics objects and its performance is given in Section 5. The HEPTopTagger algorithm, used to find and reconstruct hadronically decaying top quarks for the fully hadronic resonance search is introduce in Section 6. A series of studies to measure the HEPTopTagger top quark tagging efficiency and mistag rate with the data collected in 2012 at $\sqrt{s} = 8$ TeV are detailed in Section 7. The main analysis presented in this thesis, the fully hadronic $t\bar{t}$ resonance search performed with 2015 and 2016 dataset at $\sqrt{s} = 13$ TeV is given in Section 8. The conclusions and outlook of the results presented in this thesis are given in Section 9.

2 Theoretical Context

2.1 The Standard Model of Particle Physics

The Standard Model (SM) is a $SU_C(3) \times SU_L(2) \times U_Y(1)$ gauge theory that describes the fundamental matter particles and their interactions. Developed between the 1960s and 1970s, it explains all the known fundamental particles and their interactions, except for gravity. In the SM there are two types of particles which constitute the building blocks of matter: quarks and leptons. There are six quarks (known as quark flavors: up, down, charm, strange, top, bottom) and six leptons (electron, electron neutrino, muon, muon neutrino, tau, tau neutrino). In total, there are twelve spin-$\frac{1}{2}$ particles or fermions and they are classified into three families (see Figure 1). Each family consists of 2 leptons (one charged and one neutral) and two quarks. For all of these fundamental particles, a corresponding antiparticle exists. The first generation of quarks and leptons forms all stable matter. The second or third generation can only be generated in high energy particle collisions or in cosmic ray events because they are unstable and decay immediately to the first generation particles. Neutrinos of the three generations do not decay and they can oscillate between generations. Quarks form bound states called hadrons with integer electrical charge. The top quark cannot hadronize because it decays before hadronization is possible. Hadrons exist either as baryons, made from three quarks, such as protons and neutrons, or mesons made from a quark anti-quark pair such as pions. The interactions of the particles with each other are determined by particle mediators of spin 1, called gauge bosons. Quantum electrodynamics (QED), quantum chromodynamics and the weak interaction theory explain how the gauge bosons interact with other particles. The weak interaction theory and QED are unified into a single theory called the electroweak theory. They are the theory pillars of the the Standard Model.

Since its formulation, it has survived stringent experimental tests that have validated it with a high degree of accuracy. The measured cross sections compared to the predictions for many different processes are shown in Fig. 2. The figure shows an excellent

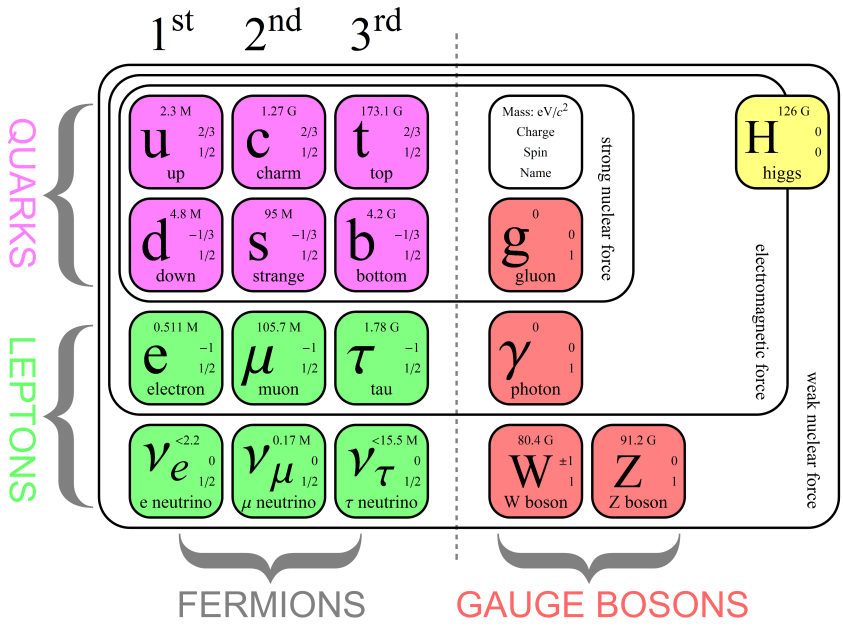

Figure 1: Organization of the fundamental particles in the Standard Model. Name, generation, mass, spin, charge are listed [1].

agreement for many different processes. However it has some limitations and open questions remain, the amount of experimental results it has predicted and explained make it the best theory to explain the interactions of fundamental particles. Unless stated otherwise the bibliographic references used in the chapter come from [2, 3].

2.2 The Electromagnetic Interaction

Electromagnetic interactions take place between electrically charged particles. The force carrier or mediator of the electromagnetic interaction is the photon (γ). It is a massless particle, electrically neutral and therefore does not interact with itself. A basic interaction between an electron and a positron in shown in Fig. 3.

Quantum Electrodynamics (QED) is the relativistic quantum field theory of the electromagnetic interaction. The theory of QED has achieved a remarkable level of compatibility with experimental observations. QED is based on a local $U(1)$ symmetry. As with any quantum field theory the kinematics and dynamics of the theory can be

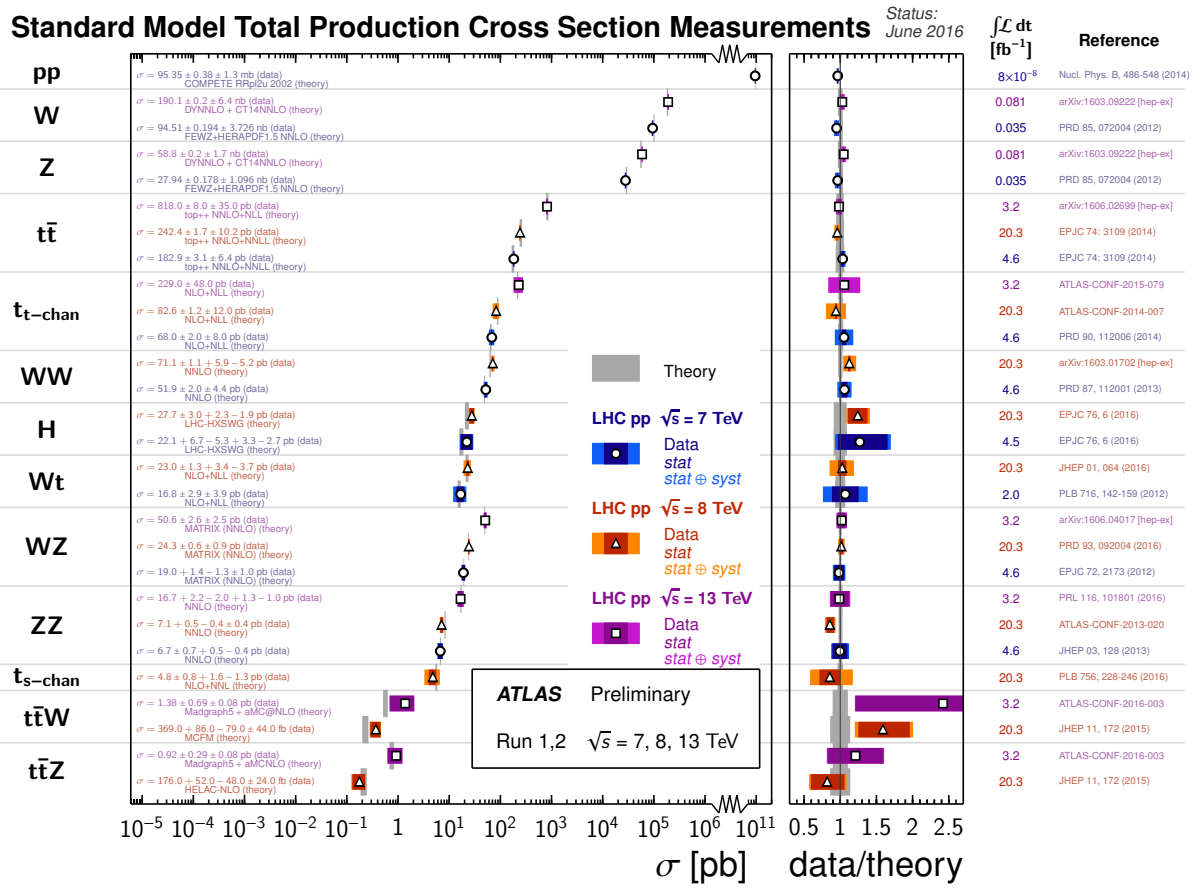

Figure 2: Standard Model cross sections predictions and measurements comparison in the ATLAS experiment. The measured cross sections match the Standard Model predictions within uncertainties [4].

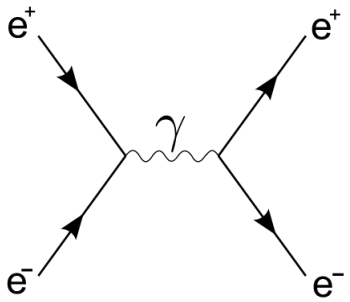

Figure 3: Photon exchange by two an electron and a positron [5].

deduced from the Lagrangian ($\mathcal{L}$),

$$\mathcal{L} = \bar{\psi}(i\gamma^{\mu}D_{\mu} - m)\psi - \frac{1}{4}F_{\mu\nu}F^{\mu\nu}. \tag{1}$$

The QED Lagrangian describes the couplings between a charged fermion with field ψ to the boson field A^{μ}. The covariant derivative (i.e, the derivate that transforms in the same as the field) D_{μ} and the field strength $F_{\mu\nu}$ are given by:

$$D_{\mu} = \partial_{\mu} - ieA_{\mu} \tag{2}$$

$$F_{\mu\nu} = \partial\mu A\nu - \partial\nu A\mu. \tag{3}$$

The $\mathcal{L}_{QED}$ is invariant under local $U(1)$ gauge symmetry, $\psi \rightarrow e^{i\theta(x)}\psi$. This gauge invariance implies that the electrical charge is conserved locally. The addition of the mass term of type $m^2A_{\mu}A^{\mu}$, leads to a violation of the gauge invariance. Therefore, the QED gauge boson needs to be massless and it can be directly associated with the photon. The elementary charge e corresponds to the elemental charge and is given by:

$$e = \sqrt{4\pi\alpha_{QED}} \tag{4}$$

where α_{QED} is the electromagnetic coupling constant. It is a fundamental parameter of the theory and it determines the strength for the EM interaction. In QED, observables are usually expressed as function of α_{QED}. Using perturbation theory to calculate these observables, one encounters divergences involving the Feynman diagrams in loops with virtual particles. A technique called renormalization is used to get rid of these divergences. The renormalization technique consists in redefining measurable observables at a given energy scale (called renormalization scale μ_0) to include virtual particle corrections, absorbing in this way the infinities. Imposing the independence of the physical observable from μ_0 reveals that α_{QED} depends on the energy scale (Q^2) at which one observes the process. $\alpha_{QED}(Q^2)$ increases as energy increases, from 1/137 at $Q^2 = 0$ to

1/127 at energies corresponding to the mass of the Z boson.

2.3 The Strong Interaction

The strong interaction is responsible for holding hadrons together. The strong interaction is described by a quantum field theory called Quantum Chromodynamics (QCD). QCD is represented by the non-abelian asymmetry $SU(3)$. In this representation color is the charge of QCD. Gluons are the elementary particles that act as the exchange particles for the strong force between quarks, being analogous to the photons in QED. They are massless and electrically neutral. However, as opposed to the photons, they do interact with themselves i.e they are not color neutral. Gluons carry color charge and this fact makes the strong interaction different and more complex from the electromagnetic where the photon has no electrical charge. The strong color charge comes in 3 types: red, green and blue. Anti-quarks have a corresponding anti-color. Leptons do not carry color charge and do not participate in the strong interaction.

The strong coupling constant decreases logarithmically with increasing energies. Hence, quarks and gluons behave as quasi-free particles at high energies (short distances), while at low energies (large distances) quarks are confined into hadrons. These behaviors are called asymptotic freedom and color confinement, respectively. An overview of measurements of α_s as a function of Q^2 is shown in Fig. 4. In the following, an overview of asymptotic freedom and color confinement is given.

- **Asymptotic freedom:** This property causes the bonds between strongly interacting particles to become asymptotically weaker as energy increases (or distance decreases). This makes perturbation theory calculations possible for QCD at high energies. The energy at the LHC is sufficiently high to describe pp collision and production of particles i.e. $t\bar{t}$ production using perturbative QCD. However, once the protons have collided and new particles are created, quarks and gluons lose energy, the strong coupling constant increases and perturbation theory is no longer applicable.

- **Color Confinement:** When quarks reach a separation distance of around 10^{-15} m, the running coupling constant is so large that new quark-antiquark pairs are produced from the radiated gluons. That is why quarks and gluons cannot exist in isolation in nature, i.e. confinement. These and anti-quarks join together in myriad combinations to make the mesons and baryons actually observed in collision. In all this debris, there is an unmistakable footprint left behind by the original quark-antiquark pair as sprays of collimated hadrons or jets emerge along the direction of the primordial quarks/gluons.

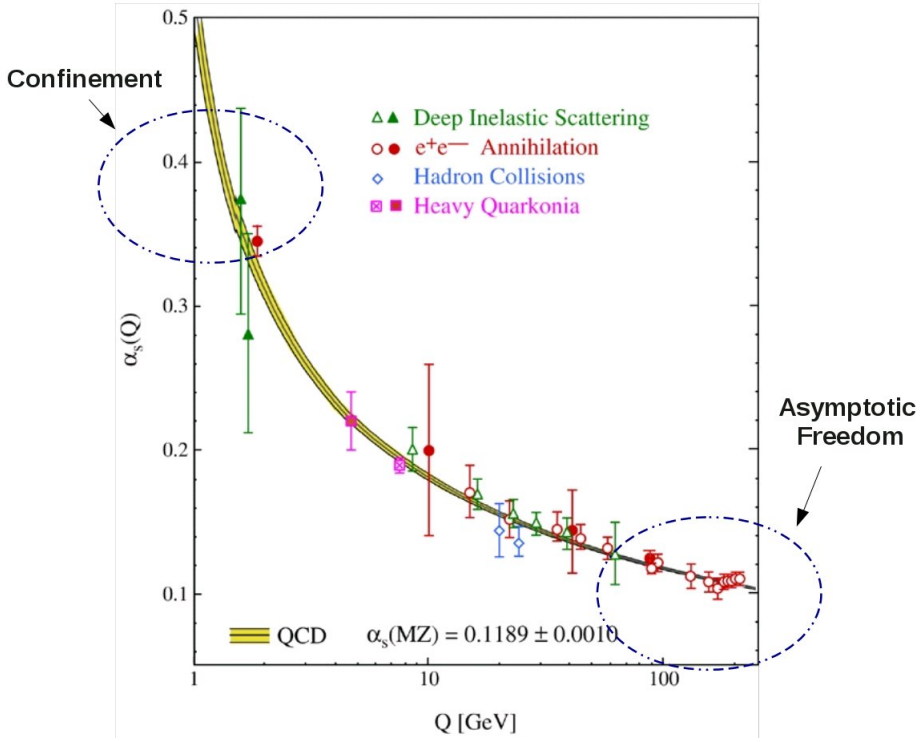

Figure 4: Overview of measurements of α_s at different scale energy scales Q. The dotted circles show the energy scale at which asymptotic freedom and color confinement take place [6].

2.4 The Weak Interaction

The weak interaction theory was initially devised to explain beta decays. Unlike the electromagnetic and strong mediators, the weak force mediators are massive. The Z^0

and $W^{\pm}$ bosons have a mass of 91.2 and 80.4 GeV respectively. and mediate the neutral and charged weak currents, respectively. Being massive mediators, the weak force has a very short range of interaction. Because the lifetime of a particle is proportional to the inverse square of the coupling constant of the force causing the decay, the lifetime of particles decaying through the weak force is large. The weak interaction is the only force capable of changing the flavor of a quark or a lepton. Moreover, it also breaks parity symmetry since $W^{\pm}$ bosons couple only to left-handed particles i.e. particles with spin and momentum of opposite direction, and right-handed antiparticles.

2.4.1 The Electroweak Theory

The weak and electromagnetic interaction were successfully described as different manifestations of the same fundamental interaction by Glashow, Weinberg and Salam in the 60s. The gauge theory describing both interactions is called unified electroweak theory and is based on the $SU_L(2) \times U_Y(1)$ symmetry group. The local gauge invariance requirement leads to the existence of bosons: $W^i_\mu (i = 1, 2, 3)$ from $SU(2)$ and B_μ for $U(1)$. g and g' are the coupling constants associated to $SU(2)$ and $U(1)$, respectively. They are related by $e = g \sin\theta_W = g' \cos\theta_W$. θ_W is known as the weak mixing or Weinberg angle.

The photon like the gluon, are massless because of the exact conservation of the corresponding symmetry generators: the electric charge and the eight color charges. The fact that the weak bosons are massive indicates that the corresponding symmetries are broken. In 1964, Brout, Englers and Higgs proposed a mechanism to explain the breaking of the electroweak gauge symmetry, now called Brout-Englers-Higgs mechanism. It predicts the existence of a spin 0 particle, known as Higgs boson. On July 4^{th} 2012, the ATLAS and CMS collaborations presented evidence for a neutral boson with a measured mass of $126.0 \pm 0.4(\text{stat}) \pm 0.4(\text{sys})$ [7] and $125.3 \pm 0.4(\text{stat}) \pm 0.5(\text{sys})$ [8], respectively. Both results are compatible with the SM Higgs boson. However, more data is needed to confirm if the neutral boson has all the properties ascribed to the SM Higgs boson.

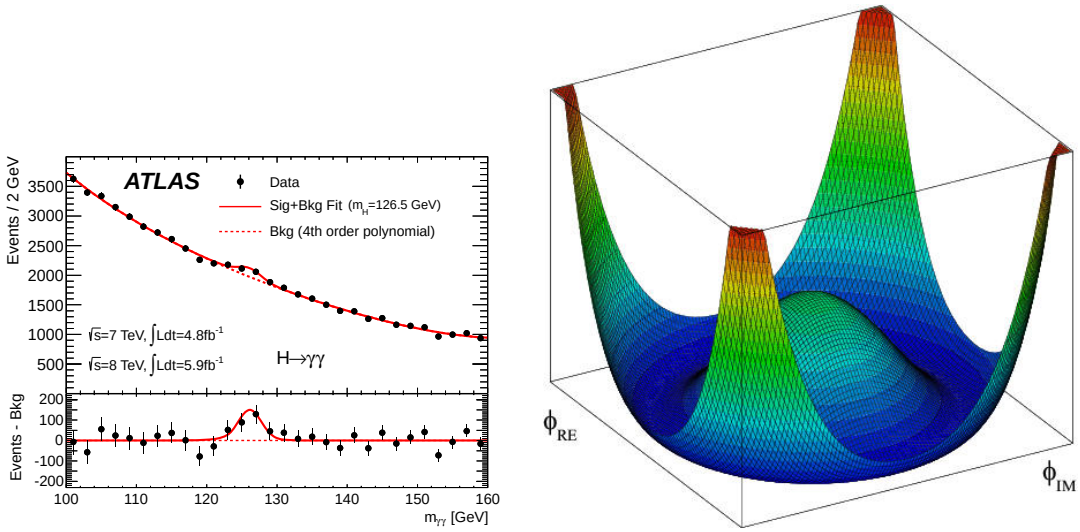

(a) (b)

Figure 5: (a) The Higgs potential for $\mu < 0$, $\lambda > 0$, Higgs boson mass of 126.8 GeV and a vacuum expectation value of 246 GeV(b) The Higgs signal observed in the diphoton mass spectrum. The fit is consistent with a Higgs hypothesis with mass 126.8 GeV [7].

2.5 The CKM Matrix

As mentioned in the previous section, weak charged currents are the only interactions that change the flavor of fermions. The mass eigenstates of fermions are not identical to the weak eigenstates. The transformation between them is described by a 3×3 unitary matrix, the Cabibbo-Kobayashi-Maskawa (CKM) matrix which describes the mixing of the quark eigenstates. The probability for a quark of flavor i to be transformed to a quark of flavor j and emitting a W boson is proportional to $|V_{ij}|^2$ as given by,

$$V_{CKM} = \begin{pmatrix} |V_{ud}| & |V_{us}| & |V_{ub}| \\ |V_{cd}| & |V_{cs}| & |V_{cb}| \\ |V_{td}| & |V_{ts}| & |V_{tb}| \end{pmatrix} = \begin{pmatrix} 0.97428 & 0.2253 & 0.00347 \\ 0.2252 & 0.97345 & 0.0410 \\ 0.00862 & 0.0403 & 0.999152 \end{pmatrix} [6] \quad (5)$$

The CKM matrix elements are free parameters of the SM and need to be determined experimentally. The CKM matrix determines that the top quark decays to a W and b-quark practically in all instances.

2.6 The Top Quark in the Standard Model

2.6.1 Introduction

The top quark is the heaviest known elementary particle. With a mass five orders of magnitude greater than the first generation quarks, it is close to the electroweak symmetry breaking scale. With a Yukawa coupling $\mathcal{O}(\sim 1)$, the top quark has the strongest coupling and (therefore the highest mass) of all quarks to the Higgs boson. Therefore, it is hypothesized that new heavier particles would couple to both Higgs boson and top quark often. This fact makes the top quark an important tool for BSM searches. The existence of a third generation of quarks was postulated in 1973 by Makoto Kobayashi and Toshihide Maskawa to explain the CP violations in kaon decay. After its prediction it was actively sought and finally discovered in 1995 at Tevatron. Since then, the world average measurement of the top quark has reached an accuracy of less than 1 GeV,

$$m_{\text{top}} = 173.34 \pm 0.27\ (\text{stat}) \pm 0.71\ (\text{syst})\ [9]$$

The production of the top quark in the SM framework as well as its decay modes is described in the following sections.

2.6.2 Top Pair Quark Production

After the shutdown of Tevatron in April 2012, the LHC became the only accelerator able to produce sufficiently high energies to produce top quarks. The several QCD processes that contribute to the $t\bar{t}$ production at hadron colliders are shown in Fig. 6. At the LHC the main production mechanism is the gluon fusion accounting to 85% percent of the the top total top quark cross section. The rest is produced in quark-antiquark annihilation.

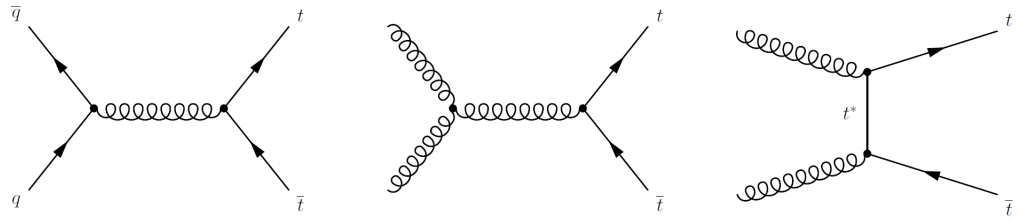

Figure 6: The leading order Feynman diagrams for top quark production.The left diagram shows quark-antiquark annihilation. The center and left diagrams show gluon-gluon fusion [10].

	σ_{NLO}(pb)	$q\bar{q} \to t\bar{t}$	$gg \to t\bar{t}$
Tevatron ($\sqrt{s} = 1.96$ TeV, $p\bar{p}$)	6.77 $\pm$ 9%	85%	15%
LHC ($\sqrt{s} = 14$ TeV, pp)	833 $\pm$ 15%	10%	90%

Table 1: Cross sections at next-to-leading order for $t\bar{t}$ production via the strong interaction at the LHC and Tevatron [9]. Errors in the cross section come mostly from parton distribution function uncertainties.

2.6.3 Top Quark Decay

The top quark has a life-time of approximately $5.0 \times 10^{-25} s$. With such a low lifetime, it is the only quark to decay before hadronization, which has a time scale of around $3 \times 10^{-24} s$. In the Standard Model and as prescribed by the CKM matrix, the only possible decays for the top quark, are $t \to bW^+$, $t \to sW^+$ and $t \to dW^+$. The probability of these decays is given by $|V_{tq}|^2$ with $q = b, s, d$, respectively. As given by the CKM matrix, approximately 99.8% of the top quarks decay into a W boson and a b-quark, with other decays having a negligible contribution. The top decay final states are therefore determined by the decay of the W boson (see Figures 7 to 9). About 33% of the times the W boson decays into a charged lepton and a neutrino (leptonic decay) and about 67% into a quark-antiquark pair (hadronic decay). As a result, there are three kinds of top pair decays: fully hadronic, lepton+jets, and dileptonic (see Figures 10 and 11). The branching ratios of the top quark decay follow from the individual branching ratios of the W boson decay modes.

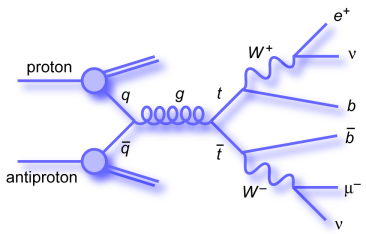

Figure 7: Top pair decay in the leptonic channel [11].

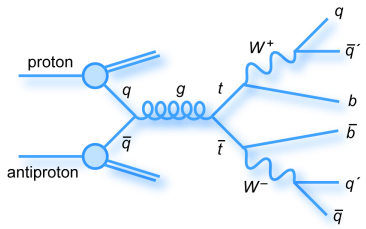

Figure 8: Top pair decay in the lepton+jets channel [11].

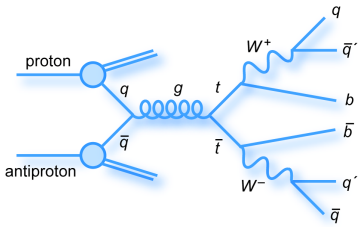

Figure 9: Top pair decay in the all-hadronic channel [11].

2.7 Beyond the Standard Model

So far there is no experimental evidence that contradicts SM predictions. However, there are unresolved issues with the theory. Some of the theoretical limitations include:

- The Standard Model describes all of the known forces but the gravitational force. At the Plank scale, $M \approx 10^{19}$, gravity becomes important at the level of fundamental particles. It is believed that the validity of the SM stops at these energies.

- It predicts massless particles. To give mass to particles spontaneous symmetry breaking is included in an unnatural way. The SM offer no explanation for this mechanism.

- The hierarchy problem is also another indication of the incompleteness of the Standard Model. Due to divergent loop corrections to the Higgs mass, renormalization needs to be applied to calculate its mass. At first order the Higgs mass is,

$$m_H^2 = (m_H^2)_0 - \frac{\lambda_f^2 \Lambda^2}{8\pi^2} \tag{6}$$

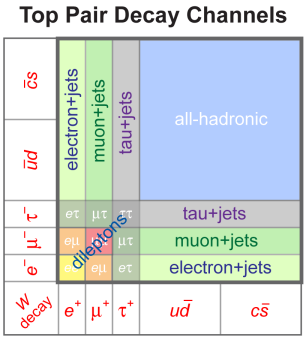

Figure 10: Top pair channel decays [11].

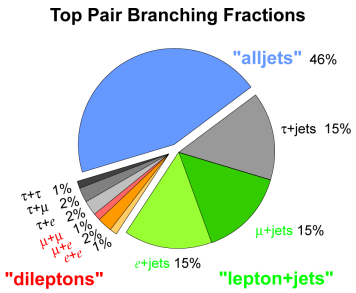

Figure 11: Top pair branching ratios [11].

where the first term is just the bare Higgs mass and the second term is the one-loop quantum correction at first order involving a fermion. λ_f^2 corresponds to the Yukawa coupling. The size of the correction depends on Λ, the scale of the process. If the SM is valid up to the Plank scale and $m_H = 125$ GeV there has to be an ad-hoc fine-tuning to balance the correction term with respect to the first term. This fine-tuning makes the universality of the theory at all energies doubtful and said to be "unnatural". The hierarchy problems arises because of the great difference between the strengths of the electroweak and the gravitational force.

The experimental limitations include:

- Gravitational effects on visible matter, radiation, and the large scale structure of the universe point to the existence of a new type of matter referred to as dark matter. Dark matter accounts for for 84% of the mass of the Universe and it is believe to be composed by previously unseen massive, weakly interacting, stable particles. Visible matter and dark matter account for about 30% of the mass-energy in the Universe. The rest is composed by an unknown energy "dark energy", believed to be responsible for the acceleration of the expansion of the Universe. Neither dark matter nor dark energy are explained by the SM.

- In the SM, the neutrinos are massless and do not oscillate between generations. However in recent years, experiments have shown that neutrinos do oscillated be-

tween generations, indicating that they have a finite mass.

These and other gaps have lead physicists to propose extensions to the Standard Model. These theories are commonly known as Beyond the Standard Model (BSM) theories. The LHC is in a position to test the validity of such theories. Since the top quark is the heaviest particle in the SM and its mass is around the EW scale, it has been suggested that it offers a special window to BSM physics [12]. The top quark decays before hadronization, offering a very clean signature to study its properties, such as mass, spin, charge, etc.

2.7.1 Technicolor

Technicolor [13, 14] is a theory that addresses the Higgs Mass Fine Tuning problem by postulating a new gauge interaction which would couple to new massless fermions called techniquarks. In the massless limit the techniquarks can be arranged in a doublet with a Lagrangian which in invariant under the transformation of the chiral symmetry $SU(2)_L \times SU(2)_R$. At high energies the interaction is asymptotically free, but forms a quark condensate at the EW scale. Therefore technicolor, like QCD, is constructed as a confining theory. If the quark condensate is expanded about the VEV, three massless quark-antiquark pairs arise which are identified with the three pions. The basic idea behind technicolor is that the Higgs is not a fundamental particle but a quark condensate. At EW energies the techniquarks condensate to a scalar field, which breaks the technicolor symmetry. The technipions are subsequently eaten by the W and Z bosons. Since the Higgs would be composed of two quarks, which are fermions and therefore have their mass protected by a custodial symmetry, there is no need for introducing any Higgs Mass fine tuning.

Topcolor Assisted Technicolor The large mass of the top quark is indicative of a special role in EWSB. The following summary is based on [15, 16, 17, 18]. Topcolor is a proposed new force of nature with $SU(3)_1 \times SU(3)_2$. Here $SU(3)_1$ couples to the first quark generations and $SU(3)_2$ to the third generations. Topcolor generates a large

top mass by forming a dynamical $t\bar{t}$ condensate. The breaking of $SU(3)_1 \times SU(3)_2$ to the SM $SU(3)_C$ gives rise to eight NGB referred to as topgluons which mostly to $t\bar{t}$ and $b\bar{b}$. In order to make the top quark heavy and b-quark light a tilting mechanism a $U(1)$ symmetry is introduced. The $U(1)$ is broken analogously to the one giving rise to $SU(3)_C$: $U(1)_1 \times U(1)_2 \rightarrow U(1)_Y$. This broken symmetry give rise to new neutral gauge boson, a Z'. The Z' solves the $t\bar{t}$, $b\bar{b}$ degeneracy by having an attractive interaction between $t\bar{t}$ and a repulsive interaction with $b\bar{b}$. It is possible to obtain different Z' models with changes to the assignment of the generations. In this thesis a leptophobic, topphylic (i.e. mostly coupling to top quarks) Z' is studied. The widths of the Z' searched for in this thesis are $\Gamma/m = 1.2\%$ and $3.0\% \times m_{Z'}$.

3 The Large Hadron Collider

3.1 Introduction

The Large Hadron Collider (LHC) [19] is a two-ring-superconducting accelerator and proton-proton (pp) collider[1] designed for high energy particle physics research. It is located at the European Center for Nuclear Research (CERN), at the Franco-Swiss border near Geneva, Switzerland. The LHC is the longest and and most powerful ring-accelerator in the world and it is designed to reach center-of-mass ($\sqrt{s}$) collision energies of up to 14 TeV and a luminosity of up to 10^{34} cm^{-2}s^{-1}. It is situated in a 26.7 km circular tunnel originally constructed for the Large Electron-Positron Collider that reaches a depth underground of up to 175 meters (Fig. 3.12).

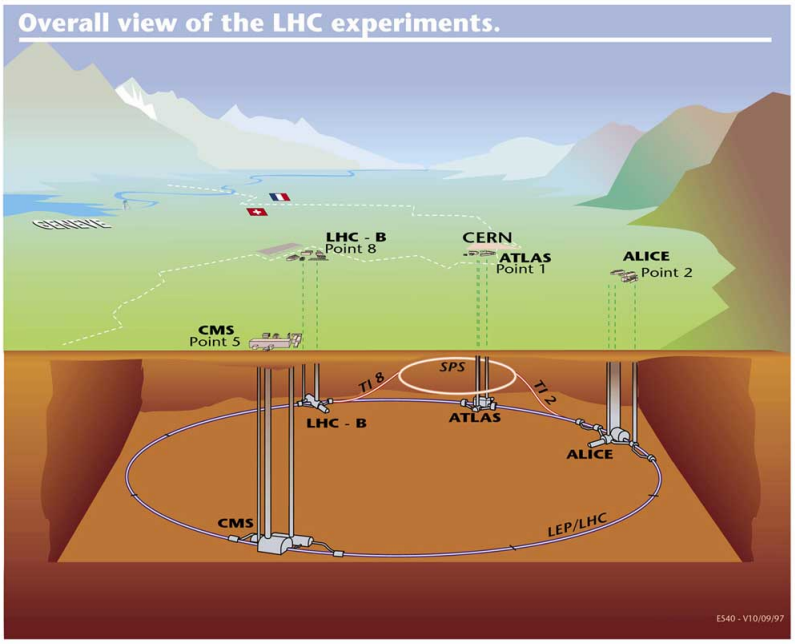

Figure 3.12: The LHC and the four main detectors: ALICE, ATLAS, CMS and LHCb [20].

The LHC consists of two adjacent parallel beamlines which intersect at four points. Through the beamlines, the proton beams travel in opposite directions and collide at

[1] Occasionally heavy ions, such as lead, are also collided for heavy ion research.

the interaction points. The four main LHC experiments, ALICE [21], ATLAS [22], CMS [23], and LHCb [24] are located at these interaction points. Protons need to undergo a pre-acceleration process before entering the LHC. First, hydrogen gas is fed into a duo-plasmatron to ionize it. Next, the bare protons go through a linear accelerator (LINAC2), the PS Booster, and the Proton Synchrotron and the Super Proton Synchrotron where they are accelerated to 50 MeV, 1 GeV, 26 GeVand 450 GeV, respectively (Fig. 3.13). The LHC can maintain a stable beam at a minimum energy of 450 GeV. Protons are accelerated in the ring for about 20 minutes before reaching their maximum energy of 7 TeV. To maintain the proton beam on a circular path, 1232 dipole magnets are used. They are cooled down to 1.8 °K by a cryogenic system using liquid helium and provide a magnetic field of up to 8.33 T. 502 quadrupole magnets along the straight sections of the beam keep the beams focused to maximize the rate of pp interactions. With these magnets the protons are accelerated close to the speed of light and guided to collision. The beams have a lifetime of approximately 10 hours. During this time, collisions take place and data are taken inside the four LHC experiments. As the intensity of the beam decreases below a certain level, it is "dumped" and directed to collide with a metal block. The field strength of the magnets is then decreased to 0.54 T for 20-40 minutes. The beam injection is then repeated and the magnets field strength again increased to 8.3 T for another cycle. This beam cycle is called a "fill".

The first beams on the LHC were circulated successfully on September 10th 2008. However on of September 19th, an electrical fault caused a magnetic quench. This in turn, caused a helium gas explosion that damaged over 50 superconducting magnets and contaminated the vacuum pipe halting the operation almost for a year. On November 2nd 2009, proton beams were again successfully circulated and the first collision recording took place at 450 GeV. Later on March 2011, the LHC set a world record for the highest energy on man-made particle collision, at 7 TeV. It continued running at this energy until the end of 2011. On March 2012, the $\sqrt{s}$ was increased to 8 TeV and it continued running at this energy until December 2012. From December 2012 up to June 2015, the LHC was in shutdown (called Long Shutdown 1 (LS1)) in which it underwent substantial

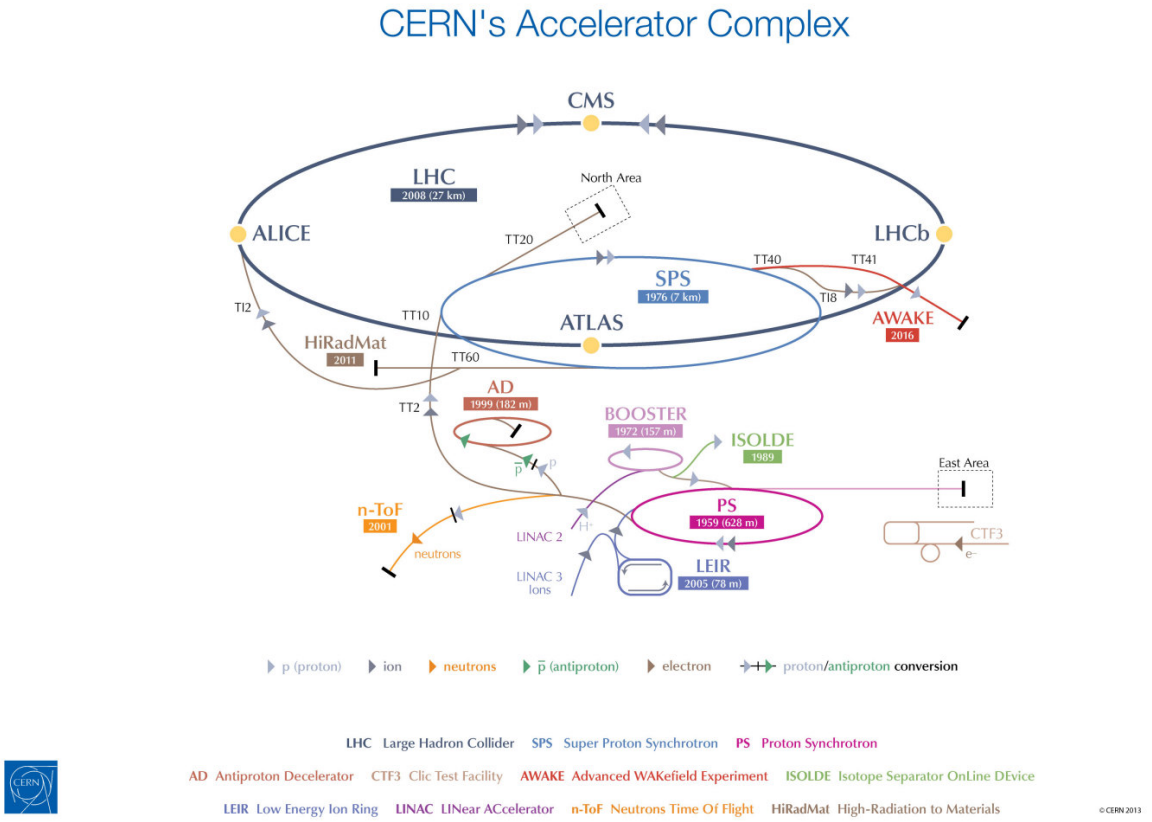

Figure 3.13: The accelerator complex at CERN [25].

upgrades and renovations. In June 2015 Run 2 of the LHC began and the accelerator reached $\sqrt{s}$. After the winter break, the LHC was turned on again and at the time of writing it is still successfully running.

3.2 Luminosity

The instantaneous luminosity is an important parameter for any particle accelerator. It basically indicates how many protons can be squeezed in a given area per unit time [$\mathrm{cm}^{-2}\mathrm{s}^{-1}$]. At the LHC, the pp beams are not continuous, but they come in "bunches". Each proton beam consists of 2808 bunches each containing around 1.15×10^{11} protons at LHC design value. To maximize the chances to observe rare physics processes, it necessary to increase the instantaneous luminosity as much as possible as shown in the

equation,

$$\frac{dN_{events}}{dt} = \sigma_{events} \cdot L, \tag{3.7}$$

where σ_{events} is the the cross section of a particular process and N_{events} is the number of events at a certain $\sqrt{s}$. Usually, the number quoted to measure the progress in data taking of an accelerator is the integrated luminosity,

$$\int \frac{dN_{events}}{dt} dt = \sigma_{events} \cdot \int L dt. \tag{3.8}$$

Figs. 3.14a and 3.14b show the total integrated luminosity for the data-taking periods in 2012, 2015 and 2016 respectively, where 20.3 fb^{-1} and 3.2 fb^{-1} are datasets good for physics analyses. At the moment of writing, the LHC is running and successfully increasing the integrated luminosity shown in Fig. 3.14c. The instantaneous luminosity is determined entirely by beam parameters as given by,

$$L = f_{LHC} \frac{nN_1N_2}{A} F \approx f_{LHC} \frac{nN_1N_2}{4\pi\epsilon\beta^*} F \tag{3.9}$$

where f_{LHC} is the crossing rate of the bunches, n is the number of bunches, N_1 are N_2 is the number of protons in each bunch. The beam cross sectional area A is related to the beam emittance, ϵ and to the beam cross sectional size at the interaction point β^*. Therefore, increasing the luminosity can be achieved by increasing the crossing rate, increasing the number of bunches, increasing the number of protons per bunch or decreasing the beam cross sectional area between the two beams.

During the Run-1 the frequency of the LHC bunch crossing at the ATLAS interaction point was 50 ns. At the beginning of Run-2 only a small set of data was taken at 50 ns, mainly to ensure the stability of the collider at the increased $\sqrt{s}$ of 13 TeV. In Run-2 the luminosity has been also increased by increasing the number of particles per bunch. Figs. 3.15, 3.16a and 3.16b show the peak luminosity during Run-1, Run-2 (2015) and Run-2 (2016) respectively. The changes in beam parameters from 2010 to 2016 are shown

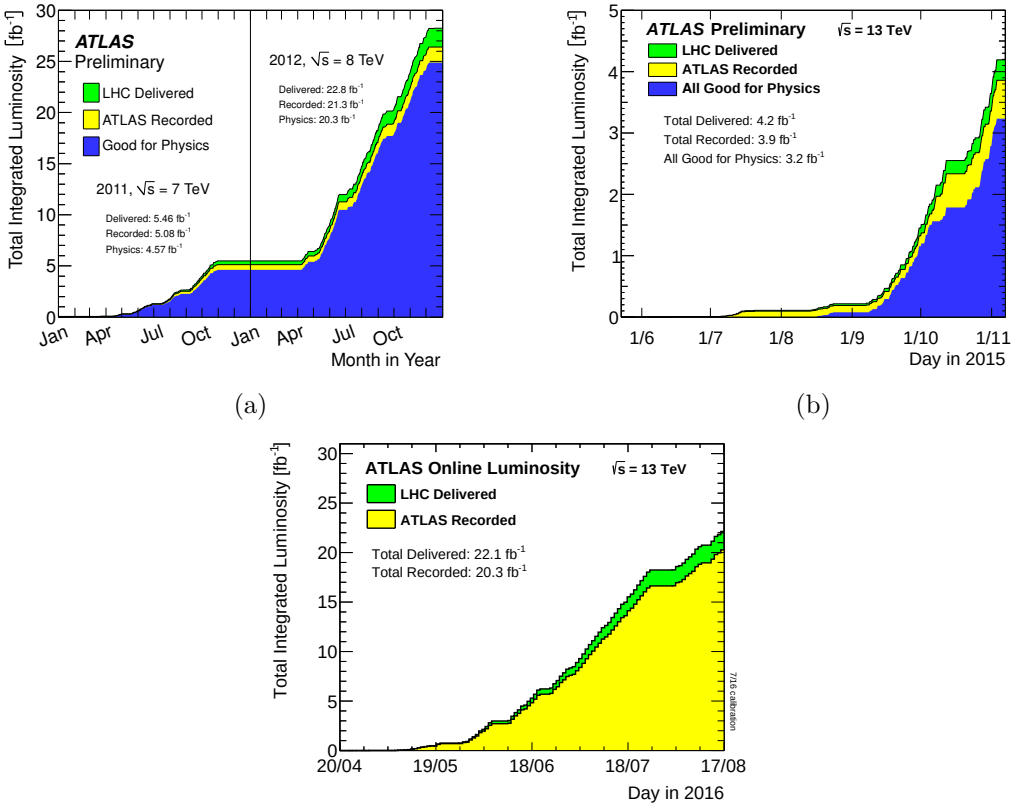

Figure 3.14: Total integrated luminosity for (a) 2012 [26] and (b) 2015 and (c) 2016 [27]. The LHC delivered, ATLAS and good for physics luminosity are indicated in different colors.

in Table 3.2.

Machine Parameter	2010	2011	2012	2015	2016	Design Value
$\sqrt{s}$ [TeV]	7	7	8	13	13	14
β^*	3.5,2.0	1.5,1.0	0.6	0.8	0.75	0.55
f_{rev}	150	75,50	50	50,25	25	25
Max number of bunches	368	1380	1380	2244	2748	2808
Max number of protons [10^{11}/bunch]	1.2	1.45	1.7	1.2	1.2	1.15
Peak Luminosity [cm^{-2},s^{-1}]	2.1×10^{32}	3.7×10^{33}	7.7×10^{33}	0.5×10^{34}	1×10^{34}	1×10^{34}
Max $\langle\mu\rangle$	4	17	37	20	40	19

Table 3.2: LHC beam parameters from 2010 to 2016. LHC design values are included in the last column [28, 29, 30, 30, 19].

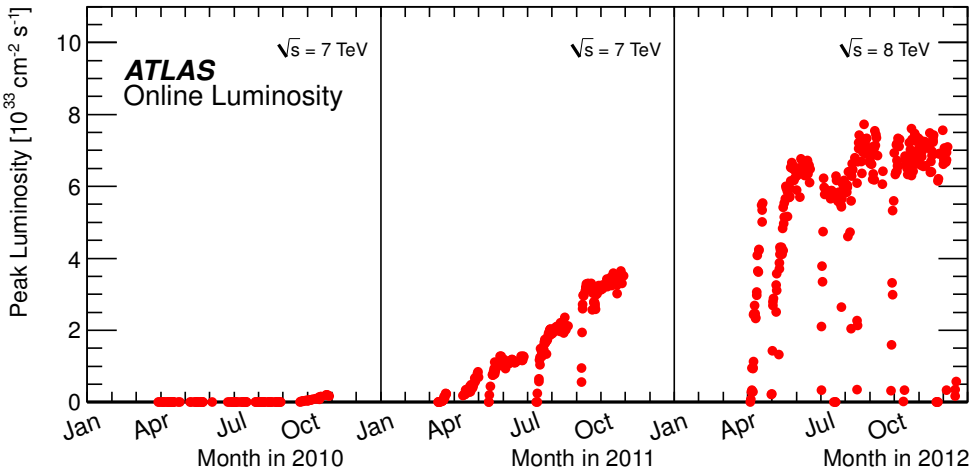

Figure 3.15: Peak luminosity per fill as a function of time 2012 [26].

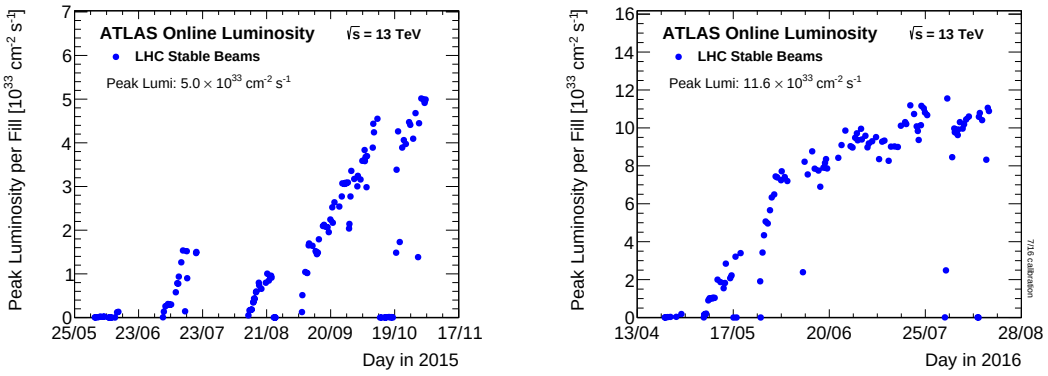

(a) (b)

Figure 3.16: Peak Luminosity per fill as a function of time for Run-2 in years(a) 2015 and (b) 2016 [27].

3.3 Pile-Up

Increasing the luminosity increases the chance of additional *pp* interactions other than the primary vertex or hard interaction. Increasing pile-up worsens physics measurements and new methods must be devised to removed and correct for this additional, unrelated energy. There are two types of pile-up: extra *pp* interactions within the same bunch crossing (in-time pile-up) and *pp* interactions coming from a different bunch crossings (out-of-time pile-up). The number of reconstructed vertices (N_{PV}) can be used to es-

timate the in-time pile up. Another measure of pile-up sensitive to both, in-time and out-of-time pile-up, is the mean number of pp collisions per bunch crossing at the time of the recorded event $\langle\mu\rangle$. $\langle\mu\rangle$ is formally defined as,

$$\langle\mu\rangle = \frac{L_{bunch} \times \sigma_{\text{inel}}}{f_{LHC}} \tag{3.10}$$

where L_{bunch} is instantaneous luminosity per bunch, σ_{inel} is the pp inelastic cross section and f_{LHC} is the revolution frequency of the protons at the LHC. Fig. 3.18 shows the recorded luminosity as a function $\langle\mu\rangle$ for Run-1 (left) and Run-2 (right). As an example, reducing the cross sectional beam area by reducing the β^* parameter, leads to noticeable increase in $\langle\mu\rangle$ as shown in Fig. 3.17.

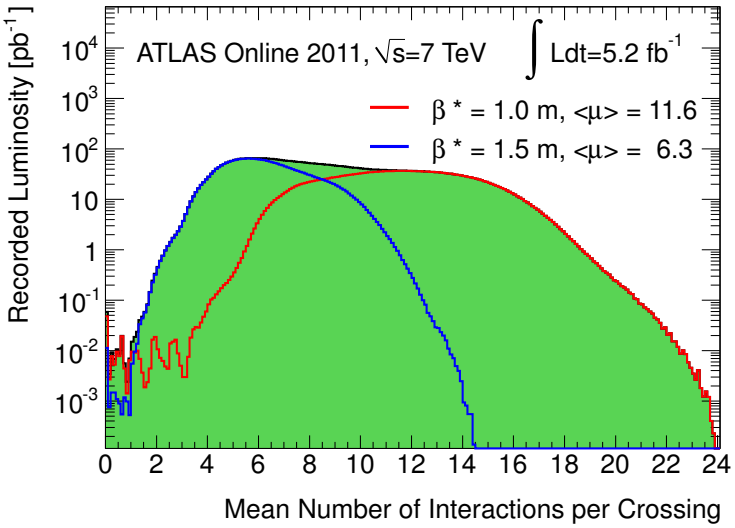

Figure 3.17: Recorded luminosity as a function of $\langle\mu\rangle$. The blue and the red lines indicates the different values of β^* [26].

3.4 Phenomenology of *pp* collisions

The proton is not a fundamental particle, such as the electron, but it possesses internal structure. The structure of the proton was revealed in a similar fashion to the structure of the atom 70 years earlier by Rutherford. The process used for this discovery was

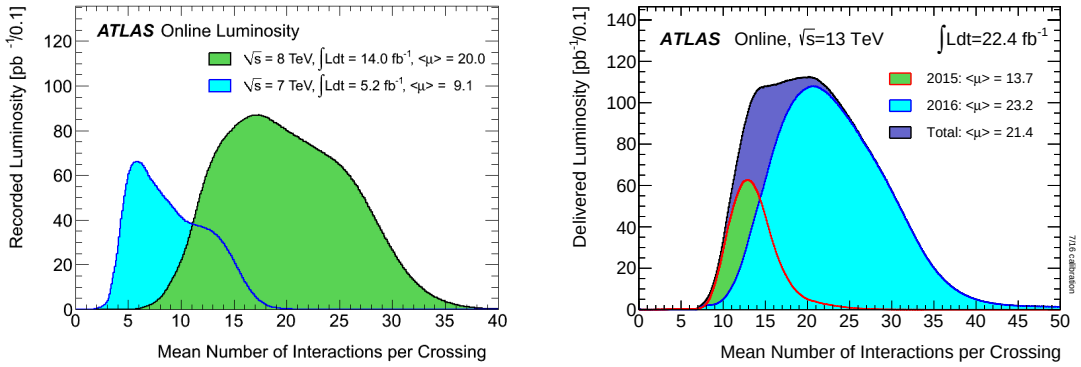

(a) (b)

Figure 3.18: ATLAS $\langle\mu\rangle$ distributions (a) 2012 and (b) 2015 and 2016 [26, 27].

scattering an electron off a proton in the so-called deep inelastic scattering experiments (DIS). The typical scattering experiment proceeds as $ep \to e'X$ and it's illustrated in Fig. 3.19. The variables used to described DIS are:

$$Q^2 = -q^2 \quad (3.11) \qquad \nu = P \cdot q \quad (3.12) \qquad x = \frac{Q^2}{2M\nu} \quad (3.13) \qquad y = \frac{q \cdot p}{k \cdot P} \quad (3.14)$$

where x is commonly referred as Bjorken-x and interpreted as the fraction of proton's momentum carried by the struck quark in the proton's infinite-momentum frame. The inelasticity y, interpreted in the proton rest frame as the fraction of energy transferred from the lepton to the proton.

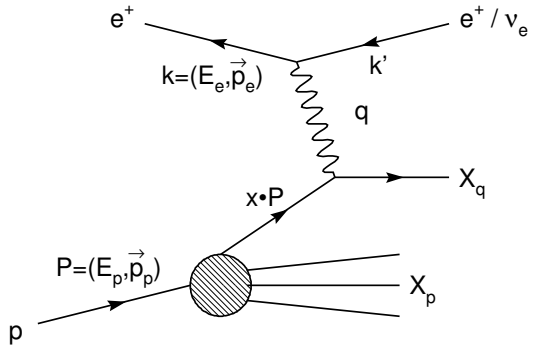

Figure 3.19: Kinematics of Deep Inelastic Scattering [31].

The inelastic electron-proton scattering cross section can be written as

$$\frac{d^2\sigma}{dxdQ} = \frac{4\pi a^2}{xQ^2}[(1-y)F_2(x,Q^2) + xy^2F_1(x,Q^2)] \tag{3.15}$$

where F_1 is the purely magnetic structure function and F_2 is the electromagnetic structure function. Structure functions describe the momentum distribution of the quarks within the proton. The structure of hadrons can be at a first approximation described by the parton model, where the structure functions do not have any dependence with Q^2. The parton model states that the protons are formed three quarks. One of the consequences of the parton model is Bjorken scaling. Bjorken scaling states that the structure functions for a fixed x must be independent of Q^2 or experimentally observed hadrons behave as collections of virtually independent point-like constituents. However as more experiments were conducted, a violation of Bjorken scaling was observed indicating that the parton model was incomplete and that there were many other particles inside of the proton (see Fig. 3.20).

3.4.1 Parton Density Functions and Factorization

Parton distribution functions (PDFs) are defined as the probability of finding a particle within a longitudinal momentum fraction x and $x + dx$, at a given energy scale Q^2. In the parton model of QCD , the hadronic cross section of two colliding hadrons h_1, h_2 is given by the factorization theorem,

$$\sigma_{h_1,h_2} = \sum_{a,b} \int_0^1 dx_1 \int_0^1 dx_2 f_{a/h1}(x_1,\mu_F) f_{a/h2}(x_2,\mu_F) \int_0^1 d\sigma_{a_1,a_2}(x_1,P_1,x_2,P_2,\mu_F) \tag{3.16}$$

where the functions $f_{a/h1}(x_1,\mu_F)$ are the parton density functions (PDF). The PDF's give the probability of finding a parton a of momentum $x \times P$ in a hadron h of momentum P. The factorization theorem states that the dynamics of the hadronic substructure can be described by PDF's independently of the hard scatter process. The Q^2 evolution is described by the Dokschitzer-Gribov-Lipatov-Altarelli-Paresi (DGLAP) equation PDF

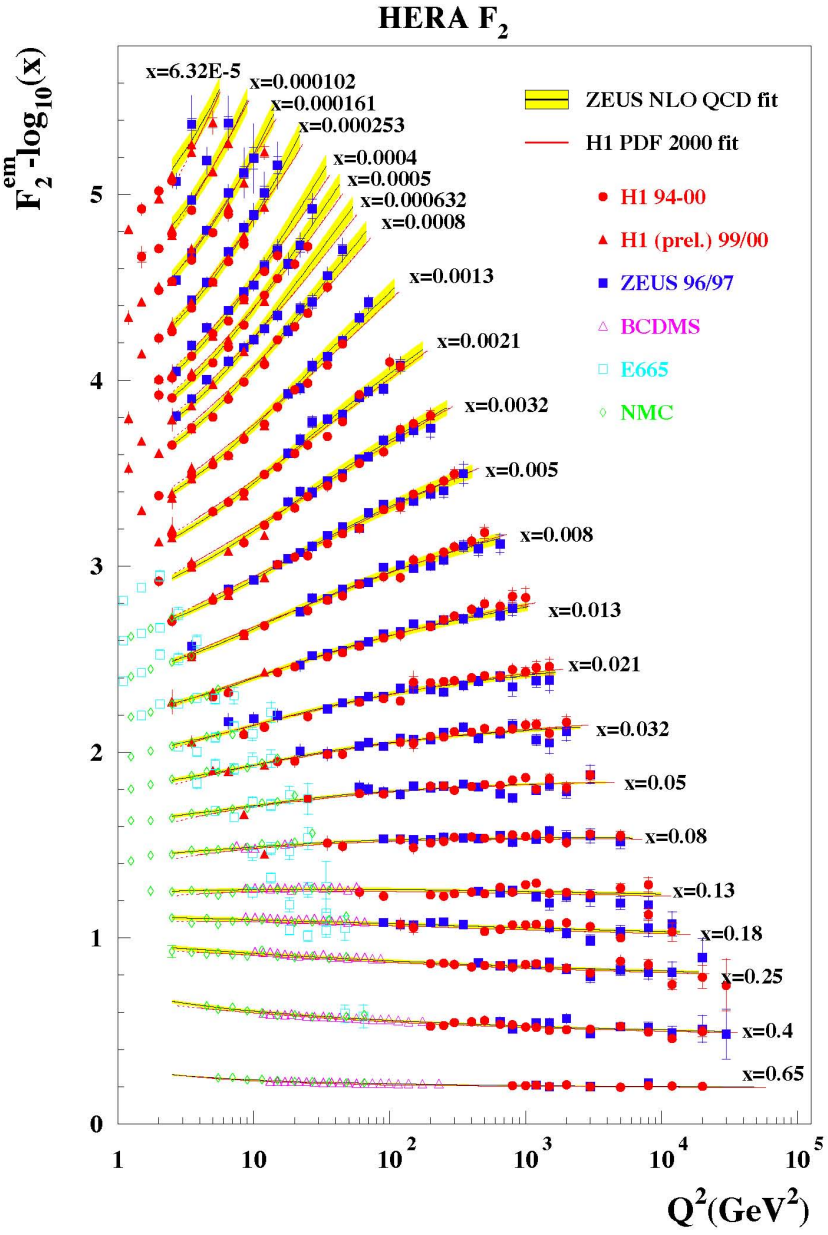

Figure 3.20: Structure function F_2 measured as a function of Q^2 at the HERA experiments, H1 and ZEUS and CERN experiments NMC and BCDMS and Fermilab experiment E665. At low Bjorken-x values the structure function shows a strong Q^2 dependence indicating violation of Bjorken scaling [32].

cannot be calculated in perturbative QCD, therefore they are extracted from data. The PDF's obtained from the collaboration HERAPDF are shown for two different Q^2 scales as a function of x are shown Fig. 3.21. Several other collaborations such as CTEQ[33, 34], MSTW[35] and NNPDF[36] perform fits to datasets with differences in the exact choice of input data and chosen parametrization.

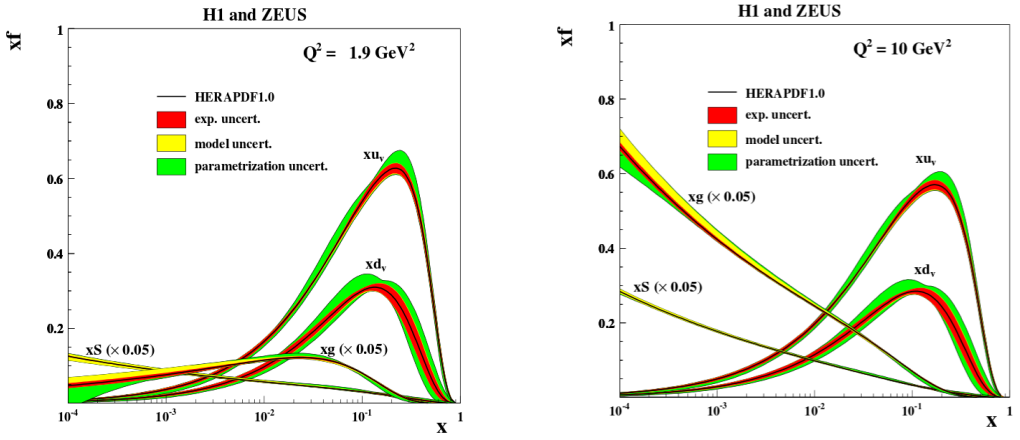

(a) (b)

Figure 3.21: (a) Parton Distribution Functions from HeraPDF at (a) $Q^2 = 1.9$ GeV and (b) $Q^2 = 10$ GeV. The gluon and sea quark distributions are scaled down by a factor of 20 [37].

3.4.2 Parton Showers

The rest of the successive emission of quarks and gluons from the partons in the initial or final state is simulated by the parton shower. This simulation assumes completely independent parton emissions and does not consider virtual corrections and therefore is only an approximation. In the almost collinear splitting of a parton, the $n+1$-parton differential cross section can be related to the n-parton cross section before splitting by:

$$d\sigma_{n+1} \approx d\sigma_n dP_i(z, q^2) \approx d\sigma_n \frac{\alpha_s}{2\pi} \frac{dq^2}{q^2} dz P_{ji}(z) \tag{3.17}$$

where $dP_i(z, q^2)$ gives the probability that parton i will split into two partons at a virtuality scale or invariant mass q^2, with parton j carrying a fraction z of the momentum

of parton i. There are three possible processes for QCD emission (splitting), $q \to gq$, $g \to gg$ and $g \to q\bar{q}$. In the simulation, the shower is evolved by repeatedly applying Eq. (3.17) iteratively, for each parton involved in the hard interaction. Parton showers are implemented in MC programs via the Sudakov form factors:

$$\Delta_i(q_1^2, q_2^2) = exp\left(\sum_j \int_{q_1^2}^{q_2^2} \int_{z_{min}}^{z_{max}} dP_i(z, q^2)\right). \tag{3.18}$$

The Sudakov form factors give the probability that a parton evolves from an initial scale q_1 to a lower scale q_2 *without* splitting. In the final-state showers the branching algorithm is implemented in the following steps:

1. Given the initial scale Q^2, partons emit radiation at scale q_2^2 determined by the Sudakov factors.

2. If the scale q_2^2 is below the hadronization scale (order of 1 GeV), the shower is terminated and hadronization is started

3. The procedure is repeated for each new parton produced by the splitting, taking q_2^2 as initial state.

For initial state showers, radiation is emitted by the colliding partons, and the final energy scale is the one that enters the hard interaction. MC generators use a backward-evolution which starts setting the correct parton momentum for the hard scatter and then develops the shower backwards, with the parent partons gaining energy at each emission.

3.4.3 Hadronization

As the partons evolve and radiate and the value of Q^2 become on the order of 1 GeV, the confining effects of QCD become more important and the dynamics enter a non-perturbative phase which leads to the formation of the observed final-state hadrons. As it is usually the case for non-perturbative physics, MC event generators rely on

phenomenological model to simulate these processes. The most common hadronization models used are the string model [38] and the cluster model [39].

In the string model gluonic strings represent the confinement of partons induced by the color force. When quark-antiquark pairs move apart the string is stretched ant the energy potential grows. When an energy of the order of hadron masses is reached, it is energetically favorable for the string to break and create a new quark-antiquark pair.

In the cluster model forces the final state gluons to split in quark-antiquark pairs. To achieve this groupings of partons forming colorless clusters are used. The heaviest clusters decay and split into lighter clusters. Most clusters have masses below 3 GeV and their decay is simulated with three body models with intermediate resonances.

3.4.4 Underlying Event

When protons collide, there can be other low energy collisions besides the hard interaction where only spectator partons participate [40]. Since these processes occur at very low energies, it is not possible to calculate them using perturbation theory. Therefore phenomenological models have to be used. The parameters of these models are usually tuned to experimental data, such as the number of charged particles.

3.5 Monte Carlo Generators

Monte Carlo generators are indispensable tools for the modeling and prediction of events in high-energy physics. In the following the most widely used tools for ATLAS experiment and for this thesis are discussed.

PYTHIA PYTHIA [41, 42] is a general purpose Monte Carlo Generator (GPMC) which calculates the hard $2 \to 2$ parton scattering at leading order (LO) in perturbative QCD. Higher orders are simulated using a parton shower (PS) . The emission of the PS are ordered in transverse momentum. The partons are hadronized using the Lund string model [38]. Pythia can also simulate the multiple interactions required for the UE. The hadronization and UE parameter can be tuned to data. The ATLAS tunes are described

in [43, 44]

HERWIG HERWIG [45] is a leading-order GPMC as well. The emissions from the PS are ordered in opening angle. For the hadronization and the UE, cluster fragmentation is used. HERWIG is usually combined with the JIMMY generator [46] to generate multiple interactions. HERWIG has a complete implementation of color coherence. The hadronization and UE can be tuned to data.

POWHEG POWHEG [47] combines a next-to-leading (NLO) QCD calculations with a parton shower without double counting. POWHEG can be interfaced with either PYTHIA or HERWIG for the simulation of the parton shower, hadronization and UE.

MC@NLO MC@NLO [48] also combines a next-to-leading (NLO) QCD calculations with a parton shower without double counting. It uses the HERWIG parton shower.

4 The ATLAS Detector

4.1 Introduction

The ATLAS (A Toroidal LHC ApparatuS) detector is one of two multipurpose particle physics experiments located at a collision point of the LHC. The layout of the detector with its major subsystems is shown in Fig. 4.1. The ATLAS detector is 25 m high and 44 m long and weights approximately 7000 tons. It has an almost 4π coverage with nominal forward-backward symmetry with respect to the interaction point. The ATLAS collaboration is formed by more than 2900 physicists and engineers from 172 institutions around the world. Four major components or sub-detectors compose the ATLAS detector: The magnet systems, the inner detector, the calorimeters and the muon spectrometer. A sophisticated trigger system is implemented to select only events that contain signatures with potential interesting physics. A slice of the ATLAS showing how the particles are identified in each subdetector is shown Fig. 4.2.

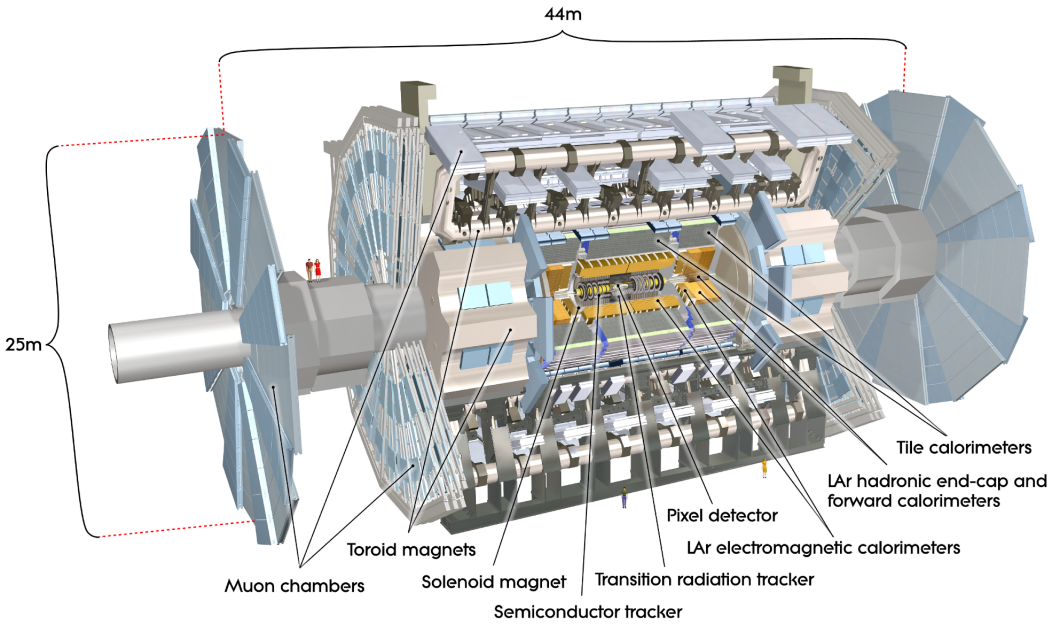

Figure 4.1: A layout of the ATLAS detector and its main components [22].

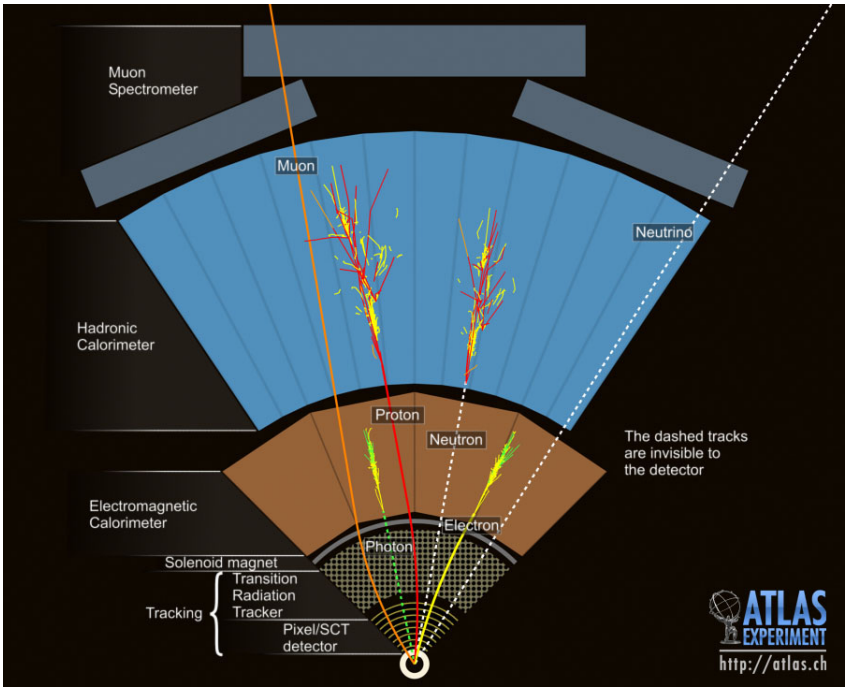

Figure 4.2: A slice of the ATLAS showing how the particles are identified in each sub-detector [22].

Coordinate System: The ATLAS Detector uses a Cartesian right-handed coordinate system, with the pp interaction point as the origin. The x-axis points to the center of the LHC ring, the z-axis points to the beam direction and the y-axis points upwards (Fig. 4.3). The azimuthal angle ϕ is measured from the positive z-axis. The polar angle θ is measured from the positive y-axis. The rapidity is defined as $y = 0.5 \times \ln[(E + p_z)/(E - p_z)]$ and the pseudorapidity as $\eta = -\ln(\tan(\frac{\theta}{2}))$. For massless objects the rapidity and the pseudorapidity are equivalent. These variables are extensively used in collider physics because of their invariance to Lorentz boosts along the z axis. In a pp collision, the boost along the z-axis is not known because the partons[2] that collide and give rise to new particles, carry an unknown fraction of the proton's momentum, as determined by the parton distribution function. Therefore, variables that are invariant to boosts along the z-axis are preferred in collision experiments. Likewise, the transverse momentum, p_{T}, transverse energy, E_T and transverse missing energy, E_T^{miss} (coming from

[2]A parton can be a quark or a gluon.

undetected particles) are all defined with respect to the $x-y$ plane. A distance between two points in the $\eta-\phi$ space is defined as $\Delta R = \sqrt{(\Delta\eta)^2 + (\Delta\phi)^2}$.

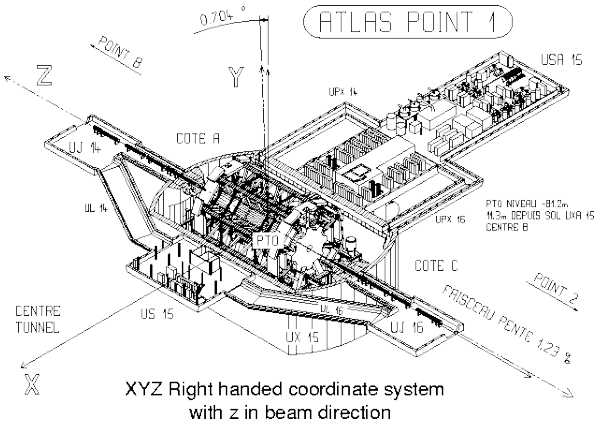

Figure 4.3: The ATLAS detector coordinates [22].

4.2 Magnet System

Two superconducting magnets are used to bend charged particles (Fig. 4.4). The inner solenoid provides a 2 Tesla magnetic field surrounding the Inner Detector. It has a longitude of 5.8 m and a diameter of 2.5 m. It operates with a nominal current of 7730 A. It is cooled down using liquid helium down to a temperature of 4.5 K. The outer toroidal magnetic field is produced by very large air-core superconducting barrel loops and two end-caps air toroidal magnets, all situated around the muon system. It provides a magnetic field of approximately 0.5 and 1.0 for the muon detectors in the central and end-cap regions respectively. The outer toroidal magnet measures 22 meters in diameter and 26 m long in length. With a stored energy of 1.6 GJ it provides the magnetic field over a volume of approximately 12,000 m^3.

4.3 Inner Detector

The inner detector (ID) starts a few centimeters from the beamline and continues radially up to 1.2 meters. It spans seven meters in length along the beamline. Its basic function is to track charged particles created from the *pp* collision. Tracking reveals the paths

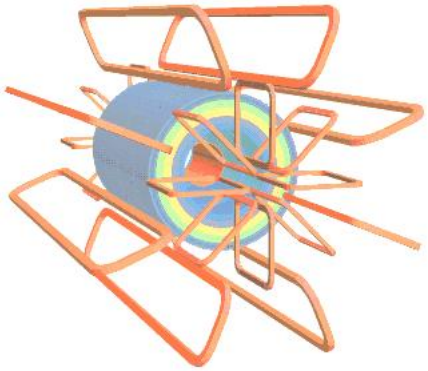

Figure 4.4: A computer generated image of the ATLAS Magnet System. The eight barrel toroid coils with the end-coil and inner solenoidal magnet are visible [22].

of charged particles. The curvature of the particle's track (caused by the presence of a magnetic field) is recorded and this allows for a measurement of its momentum via the sagita. The orientation of the track gives the particle's charge. The inner detector is also capable to identify secondary vertices coming from long-lived particles . The designed momentum resolution is,

$$\sigma_{p_{\mathrm{T}}}/p_T = 0.05\%\, p_{\mathrm{T}}\ \mathrm{GeV} \oplus 1\%. \tag{4.1}$$

During the LS1, a 4th pixel layer, called Insertable B-layer (IBL), was added to the ID. The increased number of pixels improves identification of b-quarks. The ID is composed of three parts: the Pixel Detector, the Semi-Conductor Tracker, and the Transition Radiation Tracker.

4.3.1 Pixel Detector

The Pixel Detector (PD) is the inner most part of the inner detector (see Fig. 4.5). It has a coverage up to $|\eta| = 2.5$ and complete ϕ coverage. The four pixel layers are located at a radial distance from the interaction point of 32.7, 50.5, 88.5, and 122.5 mm respectively. It provides four high resolution $3D$ space points with a spatial resolution of 10 μm in the $r-\phi$ direction and 110 μm in the z direction. The 1744 modules of the

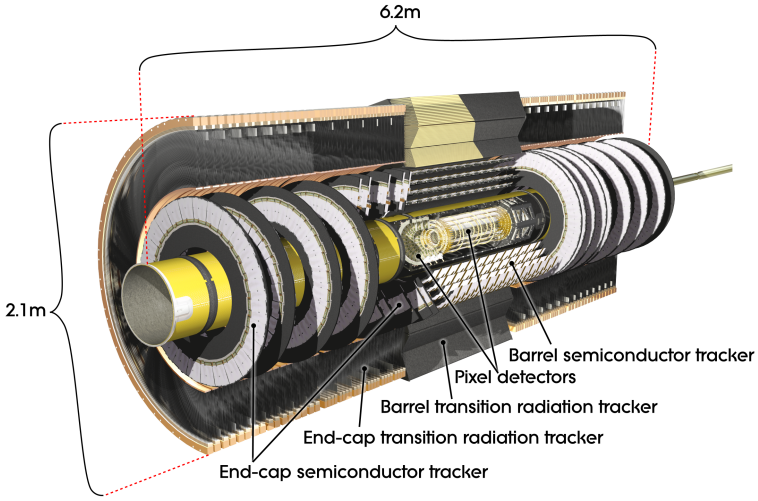

Figure 4.5: Detailed view of the Inner Detector [22].

detector are built from 250 μm thick silicon pixels connected to a read-out electronics. The pixels have dimensions of $50\mu m \times 400\ \mu m$. With this size, it is possible to achieve a very high granularity close to the interaction point. This high granularity is needed to detect primary vertices and secondary vertices coming from long lifetime decaying particles such as b-quarks and τ leptons.

4.3.2 Insertable B-Layer

The Insertable B-Layer is a fourth pixel added between a new beam pipe and the former innermost layer (B-layer) (see Fig. 4.6) [49]. The main motivations for the introduction of the IBL are:

- The B-layer and other pixel layer will have irreparable failures of modules with the passing of time. The IBL offers offers redundancy.
- Lower occupancy due to smaller pixel size. This will help at the time of the HL-LHC when the B-layer will suffer inefficiencies due to high occupancy.
- Closer distance to interaction point improves impact parameter resolution for tracks improving vertexing and b-tagging performance

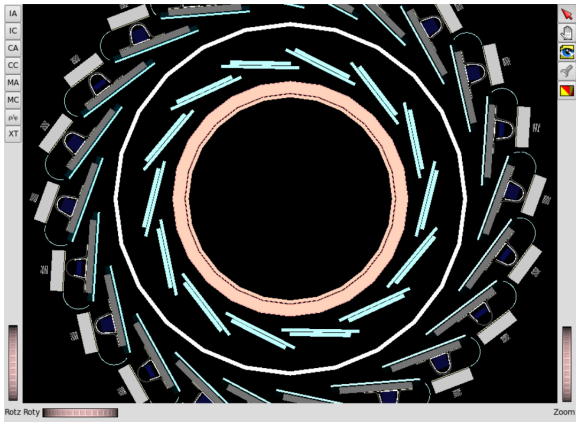

Figure 4.6: XY view showing the new (smaller) beam pipe, the IBL with modules, staves and support tube and the Pixel B-layer all implemented in the ATLAS geometry model [49].

In addtiion the previous beryllium beam pipe has been replaced by a new smaller beryllium beam pipe. *In situ* extraction of the beam pipe, where the beam pipe can be removed without having to remove the entire structure of the pixel detector was implemented as well. This makes any repairing in case of mechanical failure such as cracks or fatigue much easier.

4.3.3 Semiconductor Tracker

The Semi-Conductor Tracker (SCT) is the middle component of the ID. It has the same coverage as the PD. The design concept of the SCT is similar to the PD. However, due to a lower particle density, it is possible to use strips instead of pixels. It provides eight precision measurements per track and contributes to the measurements of momentum, impact parameter and vertex position.

4.3.4 Transition Radiation Tracker

The Transition Radiation Tracker is the outer component of the ID. It has η coverage up to 2.0 and only provides $r - \phi$ information. It uses gaseous straw tubes interspaced with transition radiation material. Charged particles crossing the straw tubes create

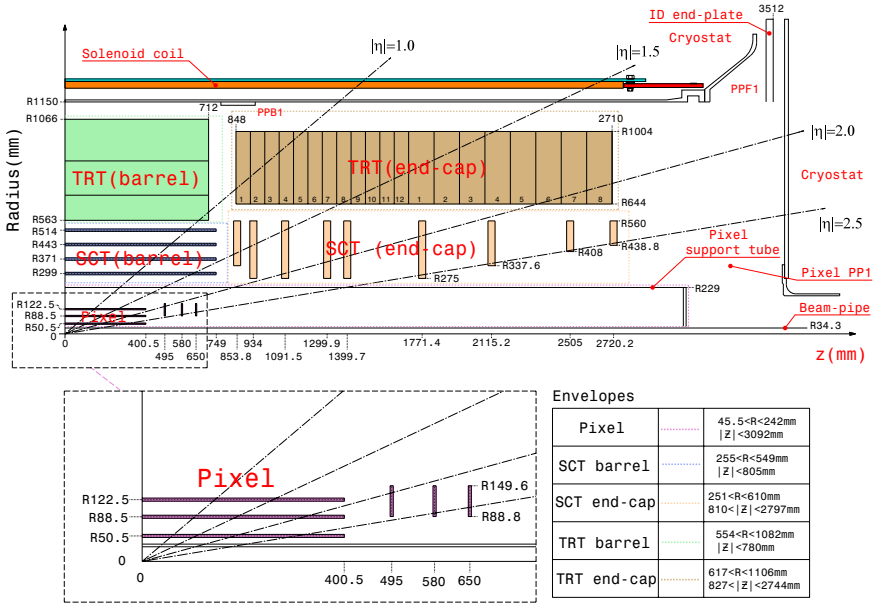

Figure 4.7: A quarter-sectional view of the ATLAS inner detector, showing each of the sub-detectors, their envelopes, and the geometrical space that they cover [22].

transition radiation[3] that is then absorbed by the xenon gas within. In the center of the straw there is a 30 μm gold covered tungsten wire that in turn collects the electrons coming from the xenon gas. The capability of transition radiation from the TRT provides stand-alone electron identification. The TRT provides around 36 measurements allowing a precise reconstruction of the particles trajectory. It contributes the most to the momentum measurement in the inner detector.

4.4 Calorimeters

The purpose of the calorimeters is to measure the particle's energy by totally stopping it. The calorimeter is designed to provide good energy resolution for electrons, photons and hadrons. There are two calorimeter systems: the inner electromagnetic calorimeter and the outer hadronic calorimeter. Both are sampling calorimeters, i.e. high-density material is used as an absorber while an active layer is placed in between to sample the

[3]Transition radiation is created when a highly relativistic particle crosses a material with different index of refraction. The amount of energy radiated is proportional to $\gamma = E/m$. For a given energy, electrons radiate 250 times more than pions.

shape from the particle shower. They are position sensitive, that is, they can measure energy depositions depending on their location. Large particle energies at the LHC make the calorimeter an indispensable tool. As seen from Eq. (4.1), the resolution of the ID decreases as the energy increases. The resolution of a sampling calorimeter is given by

$$\frac{\sigma_E}{E} = \frac{S}{\sqrt{E}} \oplus \frac{N}{E} \oplus C, \tag{4.2}$$

where the S represents the sampling or stochastic term. The choice of the absorber, active material and thickness of sampling layers among other factors contribute to this term. It affects the calorimeter resolution mostly in the range of $10 - 100$ GeV. N represents the noise term. It includes the electronic noise and the signal pile-up. Its contribution is significant at low energies. The constant term C takes into account the depth of the detector, detector non-uniformities and dead material among other factors. It dominates at high energies.

4.4.1 Electromagnetic Calorimeters

The electromagnetic calorimeters absorb mostly particles that interact electromagnetically. They have a resolution of $\frac{\sigma_E}{E} = \frac{10\%}{\sqrt{E}} \oplus 0.7\%$. The barrel covers $|\eta| < 1.475$ and the two coaxial end-cap wheels cover the region $1.375 < |\eta| < 3.2$. The energy-absorbing materials are lead and stainless steel with liquid argon (LAr) as the active medium. Full ϕ coverage is ensured by the calorimeter accordion shape. Liquid argon provides a good resistance to radiation and uniformity that translates into spatial uniformity in the energy measurement. Charged particles crossing the calorimeter ionize the LAr and the electrons drift towards the electrodes in the read out cell following the principle of a drift chamber. For argon to stay liquid it needs to be maintained at a temperature of 88 K. Therefore the EM calorimeter and the solenoid magnet share the same cryostat vessel in order to minimize inactive material. The EM calorimeter is designed to completely contain an electromagnetic shower. An important parameter to define the length of a given EM shower is the radiation length, X_0 of a material. It is defined as

the mean distance over which an electron loses all but $1/e$ of its energy. The particles going through the ATLAS EM calorimeter transverse 22 X_0 to 33 X_0.

4.4.2 Hadronic Calorimeters

Because the hadronic interaction length λ_{int}, is larger than the EM radiation length X_0, hadronic calorimeters need to be deeper to completely absorb hadrons and measure their energy. Hadronic showers are more complex than their electromagnetic counterparts. As an example, for a 5 GeV proton in a lead-scintillator calorimeter, the energy that goes through the hadronic calorimeter is distributed as follows:

- Ionization of charged particles (p, π, μ) (40%)
- Electromagnetic showers ($\pi^0 \to \gamma\gamma, \eta^0 \to \gamma\gamma$, e) (15%)
- Neutrons (10%)
- Protons from nuclear de-excitation (6%)
- Non-detectable energy (nuclear binding, neutrinos) (29%)

The resolution of the ATLAS hadronic calorimeter is $\frac{\sigma_E}{E} = \frac{50\%}{\sqrt{E}} \oplus 3\%$. The main reason for the lower resolution, is that the deposited energy that is absorbed in nuclear breakups and excitations (invisible energy) cannot be detected. The intrinsic response to EM showers and hadronic showers is not equal i.e. $(e/h \neq 1)$. Different responses can lead to faulty measurements. Therefore a compensation needs to be implemented to account for different responses. Compensation can be done with hardware (modifying thickness of sampling or absorbing material, etc.) or with software (adjusting the response, etc.). Once $e/h = 1$, the calorimeter is compensated.

4.5 Muon Spectrometer

The muon spectrometer (MS) starts at a radius of 4.25 meters around the calorimeters and ends at 11 m radial distance. It occupies a volume of around 16000 m^3. Such dimensions are required for accurate momentum measurements. Muons, being minimum

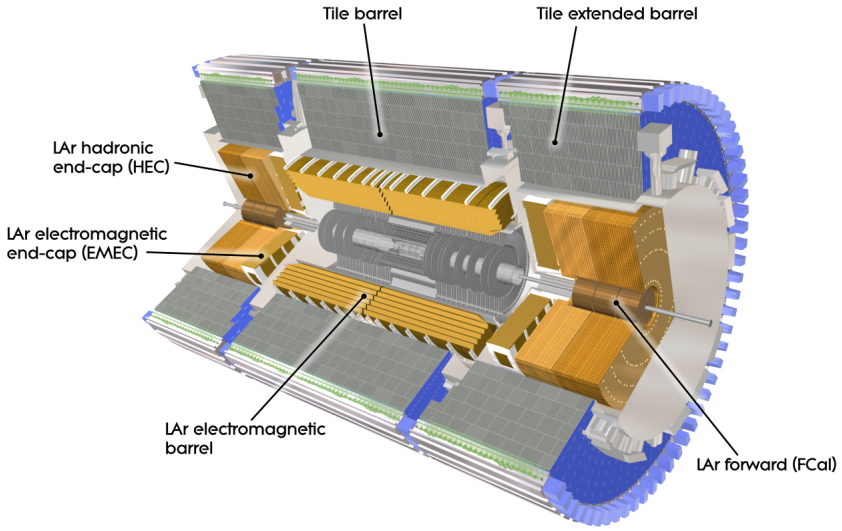

Figure 4.8: A computer generated cut-away of the ATLAS calorimeters [22].

ionizing particles pass through the inner detector and the calorimeters and reach mostly undisturbed the muon chambers. Its main function is to trigger on muons and identify and measure their momentum. The resolution on transverse momentum p_{T} is $\sigma_{p_{\mathrm{T}}}/p_{\mathrm{T}} = 10\%$ at $p_{\mathrm{T}} = 1$ TeV. The momentum reconstruction resolution is optimal around 100 GeVwith 2%. This resolution can be improved to 2% if track measurements coming from the MS are combined with those from the inner detector. Because the magnetic field bends the particles only on a plane of constant azimuth ϕ, which passes through the beam axis, no precise ϕ information is needed to reconstruct the muon momentum. Therefore, the precision chambers are built to measure the coordinate of interest η. The different parts of the MS are shown in Fig. 4.9 and discussed in the following.

4.5.1 Track Reconstruction

Monitored Drift Tubes Muon precision tracking is achieved by the Monitored Drift Tubes (MDT). They provide coverage in the range $|\eta| < 2.7$. The MDT is comprised of three layers located in the barrel region at $r = 5\mathrm{m}, r = 7.5\mathrm{m}, r = 10.0\mathrm{m}$ and four wheels at $|z| = 7.4\mathrm{m}, |z| = 10.8\mathrm{m}, |z| = 14.0\mathrm{m}$ and $|z| = 21.5\mathrm{m}$ in the end-cap region. Each

chamber consists consists of 3-8 layers of drift tubes, with an average resolution of 35 μm per chamber. The drift tubes have a long latency and therefore cannot be used for triggering.

Cathode Strip Chambers Cathode Strip Chambers (CSC) are used in the innermost layer in the range $2.0 < |\eta| < 2.7$. The CSC's are comprised of multi-wire proportional chambers. They have a precision of 40 μm in the bending and 5 mm in the transverse plane. In comparison with the MDT's, the CSC have a higher granularity and better time resolution, thus they are well suited for the harsh environment near the beam pipe.

4.5.2 Fast Muon Chambers

The fast muon chambers provide a very fast signal on the order of a few nanoseconds and thus can be used for triggering. To achieve this, a good spatial resolution, time resolution, measurement of the multiplicity and approximate energy range of muon tracks and bunch-crossing ID determination are required. Additionally, the fast muon chambers also provide coordinate measurement in the the direction orthogonal to the one measured by the tracking chambers. Two types of detectors are used: Resistive Plate Chambers (RPC) and Thin Gap Chambers (TGC).

Resistive Plate Chambers RPC provide fast trigger information and an additional azimuthal measurement to the MDT's in a coverage in the barrel-region ($|\eta| < 1.05$). The RPC is comprised of two parallel electrodes held at 2 mm. This gap is filled with by a gas mixture. Between the plates there is an electric field of 4.9 kV/mm with orthogonal segmentation to provide two-dimensional hits.

Thin Gap Chambers A TGC is multi-wire proportional chamber which provide fast trigger information and an additional hit for the coverage in the end-cap region ($1.0 < |\eta| < 2.4$). In the TGC's, the radial coordinate is measured by groups of wires, while the azimuthal coordinate is measured by radial cathode strips. An electric field of 2900 V provides a good time resolution.

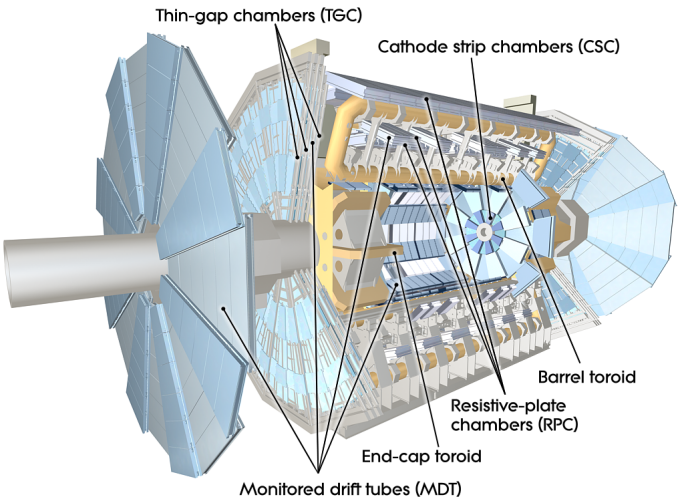

Figure 4.9: A computer generated image of the ATLAS Muon System [22].

4.6 Luminosity Determination and Forward Subdetectors

The luminosity is an essential parameter for the measurements of absolute cross-sections in any collider. The luminosity is determined by the equation:

$$\dot{N} = L \times \sigma \tag{4.3}$$

The luminosity is a quantity which is entirely dependent on the LHC machine. In the following the methods and subdetectors used for the luminosity determination are described. Broadly speaking there are two methods to determine the luminosity at the LHC: absolute methods and relative methods. Absolute methods include:

- van-der-Meer separation scans, where the beam size is measured by displacing the two beams against each other.
- Rate measurement for standard processes such as $pp \to Z/W \to \ell\ell/\ell\nu$ or the optical theorem

Relative methods or measurements of relative changes in instantaneous luminosity include:

- Currents drawn from the high voltage power supply in the forward electromagnetic calorimeter
- Particle counting for example with the LUCID detector.

Although several methods exist for determining the luminosity, only the most important are described in the following.

Van-der-Meer Separation Scan Van-der-Meer scans are the basic method to provide absolute luminosity calibration. The method consists of scanning the opposing beams against each other in the x and y directions and measuring the interaction rate. During the scan, the interaction rates are measured by the several ATLAS luminosity detectors.

LUCID LUCID (Luminosity Measurement using Cerenkov Integrating Detector) is a Cerenkov detector designed the luminosity delivered to ATLAS. LUCID is comprised by two components on each side of ATLAS located 17 meters away from the interaction point. Each component is made from 16 aluminum tubes surrounding the beam. They measure the number of inelastic pp collisions. With the measurement the online luminosity can be determined by counting the number of charged particles in the forward region. LUCID is designed to cope with luminosities of 10^{27} cm^{-2} s^{-1} up to 4×10^{33} cm^{-2} s^{-1}.

ALFA ALFA (Absolute Luminosity for ATLAS) is a subdetector which is only activated to measure the luminosity during special low luminosity (from 10^{27} to 10^{28} cm^{-2} s^{-1}) runs, the total pp cross section and absolute luminosity thus providing a calibration point for LUCID. ALFA measures the elastic scattering amplitude at very small scattering angles. The elastic scattering amplitude can be related to the total cross section by the optical theorem.

BCM The Beam Conditions monitor consist of 1 cm^2 diamond detectors located at $z = \pm184$ cm around the beam pipe. They have a fast readout and good time resolution

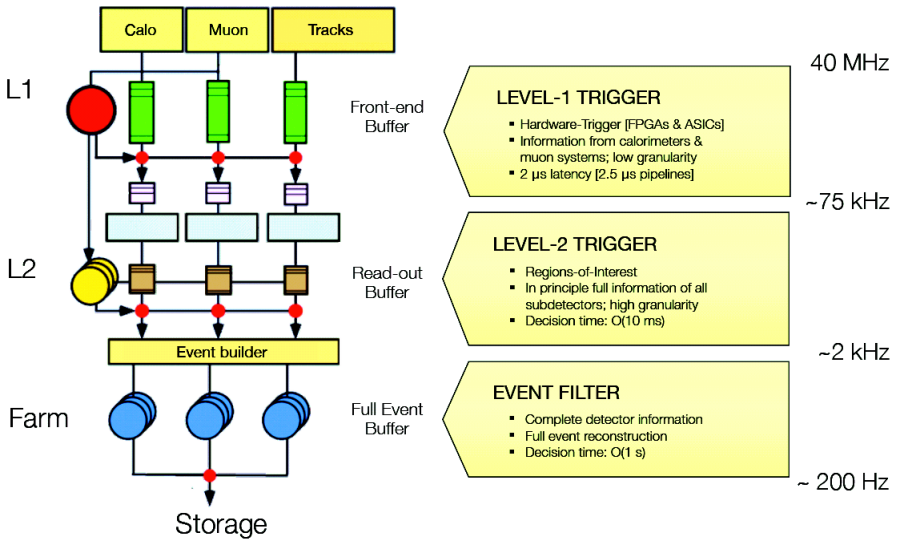

Figure 4.10: The ATLAS trigger levels [22].

which allow them to provide luminosity information for each bunch crossing. They also are used to trigger on beam losses and induce the dump of the beam, thus protecting the silicon detectors from damage that might result from an uncontrolled beam.

4.7 Trigger and Data Acquisition

At the LHC, a rate of pp interactions of 40 MHz is expected. Each reconstructed event in the ATLAS detector has a size of approximately 1.5 MB. If every event were to be recorded, 60 Tb/s would be needed. In terms of bandwidth, it is practically impossible to store all events. Since not all the LHC collisions are expected to contain useful information, a sophisticated trigger system has been devised in order to save to tape only those events which contain interesting physics information. The design and operation of the trigger is a crucial task for any detector recording hadron collisions. The trigger will decide which events will be used in the analysis. The ATLAS trigger system is organized in 3 levels:

Level-1 Trigger: The first-level trigger (L1) only uses a subset of information from the calorimeter and muon detectors. It reaches a decision within 2.5 μs. L1 is implemented

on hardware. All information is stored in pipeline memories until the L1 trigger decision is available. It is designed to accept a maximum of 75000 events/s, effectively reducing the event rate from 40 MHz to 75 kHz. The L1 trigger searches for high p_{T} muons, electrons, photons, jets, hadronically decaying τ-leptons and in general large E_T^{miss} and large total E_T. High p_{T} muons are identified with the trigger chambers (see Section 4.5) in the barrel and in the end-cap regions regions of the MS. The L1 trigger searches for local maxima of energy deposits in the calorimeter by using a fixed size sliding window algorithm working on *trigger towers* (see Fig. 4.11).

Resuls from the L1 calorimeter and muon triggers are processed by the central trigger processor. Pre-scaling of the trigger menu allows for optimal use of bandwidth as luminosity and background conditions change. During the LS1, a new element in the chain was added: the Topological Processor System (L1Topo System). The purpose of this system is to make a decision with more details than just p_{T} or E_T whose threshold was raised 2015. The system allows for determination of angular separation, invariant mass and hardness of radiation [50]. Regions-of-interest (ROI) are coordinates in η and ϕ where interesting features have been identified. The ROI's are identified and subsequently given to the higher level triggers.

Level-2 Trigger: Data from Level-1 trigger is transferred to read-out buffers until a Level-2 trigger is available. The L2 trigger selects the areas of interest identified by the L1 trigger and then refines this selection, using the full-granularity information from all the detectors, including the ID which is not used on L1. A latency of around 40 ms is expected from the L2 trigger.

Event Filter: The event filter is designed to reduce the event rate from 3.5 kHz to the 200-400 Hz. At this rate, events can be written to disk. It has similar reconstruction algorithms as the offline algorithms but with looser selection criteria. This reconstruction takes about 4 seconds per events with an event size of approximately 1.3 MB.

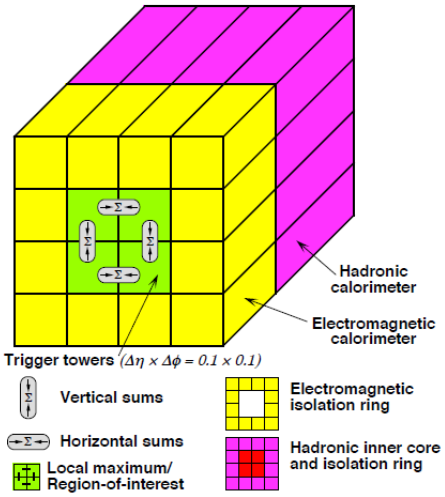

Figure 4.11: Sketch of the electron-photon and hadronic τ trigger algorithms at the L1 Level trigger [22].

4.8 The ATLAS Simulation

The ATLAS collaboration has developed a detailed simulation of the ATLAS detector based on Geant4 (G4) [51]. For any given hard process, a Monte Carlo (MC) generator will produce a set of events containing lists of final-state particles and their four-momenta with respect to the origin. These four-vectors are fed to the ATLAS G4 Model and then they are propagated through the ATLAS detector. The interactions with the detector material, such as charge deposits in the tracking detectors and showering of particles in the calorimeter material are modeled. Interactions between particles and inactive material such as support structures and cabling are also modeled. The energy deposited by particles in the active detector material is converted into detector signals with the same format as the ATLAS detector read-out. The simulated detector signals are in turn reconstructed with the same reconstruction software as used for the data. The Geant4 parameters are adjusted in accordance to match results coming from test-beam analyses.

4.9 The ATLAS Fast Simulation

A drawback of of the full simulation is that the CPU time required is around several minutes per event. More than 90% of this time is spent in the calorimeter systems. With increasing LHC luminosity, the CPU time will become a bottleneck for the production of large MC samples. A fast but accurate calorimeter simulation in therefore essential and will become more so in the future.

The FastCaloSim simulation package [52] in ATLAS is able to simulate events an order of magnitude faster. The combination of fast simulation for the calorimeter and the full simulation for the rest of the ATLAS detector is called ATLFastII of AFII. The AFII approach has already been used to simulate around half of the total ATLAS MC statistics in the 8 TeV simulations. In order to achieve the speedup in event simulation, ATLFastII makes the following simplifications:

- The simulation uses a reconstruction geometry that describes calorimeter cells as cuboids in η, ϕ and depth of the calorimeter. This is a reasonable assumption for the homogeneous regions of the EM calorimeter, but only an approximation for the other calorimeters or for the calorimeter edge regions.
- Particle showers replaced by parametrizations
- Only three types of particles simulated: electrons, photons and charged pions. The charged pion parametrization is used for all hadrons

4.10 Computing LHC Data

Even with triggering, around 15 petabytes of data per year at the LHC are expected. In view such amounts of data, the Worldwide LHC Computing Grid [53] (WLCG) has been developed. It is a network of computers, which analyze blocks of data and send it back to a centralized computer. This approach is called grid computing. The Tier 0 at CERN first processes and divides the data and divides it for its distribution. Twelve Tier 1 sites located in different countries take this data and further process it. The data

is then distributed to Tier 2 sites located in more than a 100 universities around the world. This approach allows for a versatile distribution and analysis of LHC data.

5 ATLAS Reconstruction and Performance

Before particles can be classified, "physics objects" such as electrons are reconstructed using raw detector signals. An overview of the ATLAS object reconstruction is given in the following section. Additionally, details of the reconstruction performance for the physics objects used in the analyses presented in this thesis are given. Also described are the improvements and changes that occurred during the LS1 where many reconstruction algorithms were improved, in particular the b- tagging algorithm. Unless stated otherwise, the following description follows closely the ATLAS technical design report [22].

5.1 Tracks and Vertices

Tracks Tracks are reconstructed by algorithms that hit information coming from the detector modules into three dimensional space points. Primary tracks emerge from charged particles coming from the pp collision with enough lifetime to travel through the ID. An INSIDE-OUT algorithm is the baseline track reconstruction algorithm for primary tracks with $p_{\mathrm{T}} > 400$ GeV. The algorithm builds tracks starting from the Pixel and SCT detectors and extrapolates them to the TRT using a combinatorial Kalman filter, taking into account the known magnetic field configuration and material geometry in the ID. Track segments of the TRT detector are subsequently merged with the seed tracks if they are compatible. An OUTSIDE-IN algorithm reconstructs secondary tracks which emerge from particles created at radii not allowed for the INSIDE-OUT algorithm, such as photons conversions and nuclear interactions. The OUTSIDE-IN algorithm is seeded in the TRT and the track candidate is extrapolated to the interaction point and merged with matching SCT and pixel hits. The transverse and longitudinal impact parameters d_0 and z_0, respectively, are calculated as the closest distance in the transverse and longitudinal planes between the track and the primary vertex at the point of closest approach in the transverse plane.

Vertices The position of the primary, hardest pp interaction is called the primary vertex. Vertices coming from pp interaction with lower energy are called secondary vertices. Vertices are reconstructed using the reconstructed tracks with an adaptive vertex fitting algorithm, using as input the distribution of z coordinates of reconstructed tracks at the beamline. They are constrained to be within the estimated position of the beam spot. After the vertices have been found, the tracks are re-fitted with the assumption that each track belongs to a given vertex. Generally more than one vertex is found per event. The vertex with the largest $\sum p_{\mathrm{T}}^2$ of the associated tracks is chosen as the primary vertex of the event, while others are considered pile-up.

5.2 Electrons

Electron candidates are selected by searching for localized clusters of energy in the EM calorimeter with at least one associated track [54]. The algorithm for the electron reconstruction is based on a sliding-window clustering algorithm. It performs a scan of the calorimeter, looking for local maxima of transverse energy within a window of dimensions 3×5 cells in units of 0.025×0.025 in the $\Delta\eta \times \Delta\phi$ plane [55]. If a window energy is above 2.5 GeV, then the region is marked as a seed. This threshold is chosen to optimize the reconstruction efficiency while minimizing the fake rate from electronic or pile-up noise [56]. If two clusters are too close, only the more energetic is used as seed. Electron reconstruction now proceeds to match the topocluster with a track in the ID. Tracks from the ID are extrapolated to the middle layer of the EM calorimeter and matched to the cluster seed. If a match is not possible, the cluster is tagged as an unconverted photon. If there is a match, but the track comes from a secondary vertex, then the cluster is tagged as converted photon. Finally, if the matched track comes from the primary vertex, the cluster is tagged as an electron [56]. To ensure that the electron comes from the primary vertex, electrons are required to have a transverse impact parameter of $d_0 < 1$ mm and a longitudinal impact parameter of $z_0 < 2$ mm. If the cluster is classified as an electron or a converted photon, clusters are rebuilt with a size of 3×7 central layer cells in the barrel [56]. For the present analyses, only

electrons within the tracker acceptance $|\eta| < 2.47$ are used. An isolation requirement, or mini-isolation [57] helps separate electrons coming from the hard-interaction from from non-prompt electrons and hadronic showers. The mini-isolation variable is defined as: the scalar sum of track transverse momenta within a cone of size $\Delta R = 10\ \text{GeV}/E_{\text{T}}^{\text{el}}$ around the electron track must be less than 5% of the electron transverse energy E_{T}^{el} (only tracks with $p_{\text{T}} > 1$ GeV are considered in the sum, excluding the track matched to the electron cluster).

5.3 Muons

For muon reconstruction and identification the MS and ID are used. It is possible for the calorimeters to also detect the muon as a minimum ionizing particle. The three main different reconstruction algorithms used in ATLAS for the muon reconstruction are:

- Stand-alone: uses MS information only. Tracks are extrapolated to the interaction point to obtain the impact parameters.
- Combined: uses information of both the MS and the ID taking into account the full covariance matrices of the two track fits. This algorithm provides the best muon reconstruction.
- Segment-tagged: muons are identified by ID tracks with an association to at least 1 segment track from the MS.

Additionally, there are calorimeter-tagged (CaloTag) muons. Muons are identified as such when track from the ID can be associated with an energy deposit in the calorimeter which is compatible with minimum ionizing particle. The muon reconstruction efficiency is close to 99% with in the range $|\eta| = 2.5$. Samples of $J/\Psi \to \mu_+\mu-$, $\Upsilon \to \mu_+\mu-$ and $Z \to \mu_+\mu-$ are used to calibrate the muon energy and determine its resolution. Similar to the electron isolation, a mini-isolation helps separate muons coming from the hard-interaction and muons originating from decay chains of b/c-hadrons or kaons. It is defined as the sum of the transverse momentum of all the tracks satisfying the relation,

$\Delta R_{(\mu,\text{track})} < 10\ \text{GeV}/p_{\text{T}}^{\mu}$ where p_{T}^{μ} is the transverse momentum of the muon. In a similar fashion to the electron, the mini-isolation must be less than 5% of the muon transverse momentum p_{T}^{μ}. This makes the mini-isolation cut less sensitive to pile-up effects and more efficient when the muon is close a jet.

5.4 Jets

As mentioned in Section 2.3, quarks and gluons are not directly observed, but they appear in the detector as collimated sprays of hadrons. Different jet combination schemes exist to group this spray and form jets. Jets can be built using truth stable particles (particle jets), tracks from the inner detector (track jets) or energy deposits in the calorimeters called topological clusters or topoclusters. Jets build from topo-clusters are the most commonly used in the ATLAS analyses and are usually referred just as jets. The clusters are treated as massless and are combined by adding their four-momenta which leads to massive jets.

Topological Clusters The topological clustering algorithm reconstructs three-dimensional clusters of energy deposits in the calorimeters. It is follows the shower development of single particles interacting in the calorimeter. Seed cells are chosen among cells which have signal-to-noise ratio of $|S/N| > 4$. Noise is defined as the expected RMS of the electronics noise for the current gain and conditions plus the contribution from pile-up added in quadrature. Neighboring cells in three dimensions are then added to the cluster if their signal-to-noise ratio is $|S/N| > 2$. Finally cells, with $|S/N| > 0$ in the perimeter are added to the cluster, to ensure that the tails of showers are not discarded.

Topological Cluster Calibration The energy deposited in topo-clusters is corrected to the truth MC using the Local Calibration weighting scheme [58]. The LCW scheme, shown in Fig. 5.1, first classifies topo-clusters as either electromagnetic or hadronic based on a likelihood ($\mathcal{P}_{\text{clus}}^{\text{EM}}$) which includes a measure energy density and the longitudinal shower depth. The following corrections types are then applied:

- Calorimeter non-compensation (only hadronic-like clusters);
- Signal losses due to energy outside of the topo-cluster ($w_{\text{cell}}^{\text{em-ooc}}$,$w_{\text{cell}}^{\text{had-ooc}}$) (all clusters);
- Signal losses due to energy deposited in inactive material ($w_{\text{cell}}^{\text{em-dm}}$,$w_{\text{cell}}^{\text{em-dm}}$) (all clusters);

If $\mathcal{P}_{\text{clus}}^{\text{EM}} = 1$ (completely EM cluster), the application of a hadronic calibration is suppressed and only the calibrations for EM signals are applied. If $\mathcal{P}_{\text{clus}}^{\text{EM}} = 0$ (completely hadronic cluster), all the corresponding calibrations are applied, including the hadronic calibration. The correction factors for EM and hadronic clusters are not exclusive, but follow:

$$w_{\text{cell}}^{\text{cal}} = \mathcal{P}_{\text{clus}}^{\text{EM}} \cdot w_{\text{cell}}^{\text{em-cal}} + (1 - \mathcal{P}_{\text{clus}}^{\text{EM}}) \cdot w_{\text{cell}}^{\text{had-cal}} \tag{5.1}$$

This approach reduces the possibility of inconsistent calibrations especially for low-energy or small (few cells only) clusters, as misclassification for these kinds of topo-clusters is more likely than for clusters with higher energies or larger size. These energy corrections are usually derived from the single charged and neutral pion MC simulations. Due to these corrections, it is sometimes possible to obtain topoclusters with negative energy, therefore at the analysis level only topoclusters with positive energy are used. These topoclusters are the inputs of the jet clustering algorithms presented.

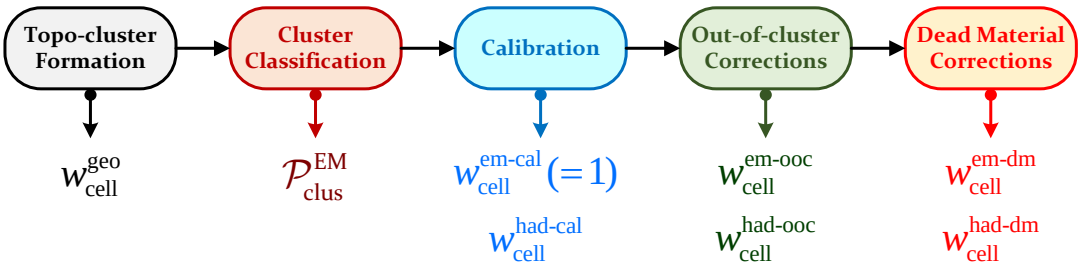

Figure 5.1: Overview of the local hadronic cell-weighting (LCW) calibration scheme for topo-clusters [59].

Jet Calibration Jets built using only EM clusters are said to be at the *EM Scale*, whereas jets built using the LCW clusters are at the *LCW Scale*. A second calibration is performed correcting the jet energy to the true energy of simulated hadron jets. This is done with simulated dijet events using a numerical inversion technique. Additionally the jet directions are corrected to point to the primary vertex. The calibration scheme used for both analyses presented is the so called *LC+JES*, where the numerical inversion is performed after clustering the jets with LCW-calibrated topoclusters.

5.5 *b*-jets

5.5.1 Identification

The large lifetime of b-hadrons, which lead to decay lengths of the order $\mathcal{O}$(mm), allows to identify jets containing b-hadrons. This technique is referred to as flavor tagging or b-tagging. b-tagging is of great importance in many analyses due to the large b-jet multiplicity. It is especially important for the $t\bar{t}$ fully hadronic resonance search in order to reduce the multijet backgrounds, which top-tagging alone cannot get rid of. In ATLAS, different algorithms exploit the signatures of the b-hadron decay [60].

- Impact parameter based algorithms: the IP3D [60] combines the impact parameter significances of all the tracks in the jet. IP3D uses a likelihood ratio technique in which input variables are compared to pre-defined smoothed and normalized distributions for both the b-jet and light jet hypotheses, obtained from MC simulation. The algorithm uses the 2 dimensional distribution of the transverse ($d_0/\sigma(d_0)$) and longitudinal ($z_0/\sigma(z_0)$) impact parameter significances, taking advantage of the correlations between the two.
- Secondary vertex finding algorithm: The secondary vertex search starts by building all two-track pairs that form a good vertex. Afterwards only tracks associated to the vertex and far enough from the primary vertex are used [60].
- Decay Chain Multi-Vertex Algorithm: JetFitter [61] reconstructs the decay chain of b hadrons which decay through an intermediate c hadron. It simultaneously

fits the cascade of b and c hadron decays assuming all tracks intersect in the same flight axis. This approach is able to distinguish the different decay topologies of b and c decays and discriminate against light quarks.

These approaches result in different efficiencies and rejections in different kinematic regimes. Therefore in ATLAS they are combined. This leads to significant improvements in tagging efficiency and reduction of fake rate. During Run-1, the used b-tagging approach is called MV1. It uses an artificial neural network to combine the IP3D, SV1 and JetFitter algorithms, giving a weight for a given jet as coming from a b, c or a light quark. If the weight of any give jet exceeds a given threshold (working point), the jet is said to be "b-tagged".

Multivariate algorithm: from MV1 to MV2 For Run-2 the MV2 algorithm has been introduced. The input variables obtained from the three basic algorithms described are combined using a boosted decision tree (BDT) algorithm to discriminate b-jets from light and c-jets. Fig. 5.2 shows a comparison for the MV1c (the "c" stands for added c-quark contribution in the training), with the Run-1 detector and reconstruction software compared to the default MV2c20, with the Run-2 detector and reconstruction software. In this comparison the light flavor rejection is improved by a factor of about 4 and the c-jet rejection by a factor of about 2 for a b-tagging efficiency of 70%. The change from artificial neural network to BDT not only improves the performance but also simplifies the algorithm significantly [62]. The MV2c20 algorithm is defined as the output of the BDT where the training is performed with b-jets as signal and a mixture of 80% light-flavor and 20% c-jets as background. Using 20% of c-jets (as opposed to none) as background keeps light-flavor rejection efficiency approximately constant, as shown in Fig. 5.3b, while increasing the c-jet rejection by a factor of of two as shown Fig. 5.3. From the 2015 data-taking period to 2016, the b-tagging were updated and improved, and a tagger MV2c10 is recommended.

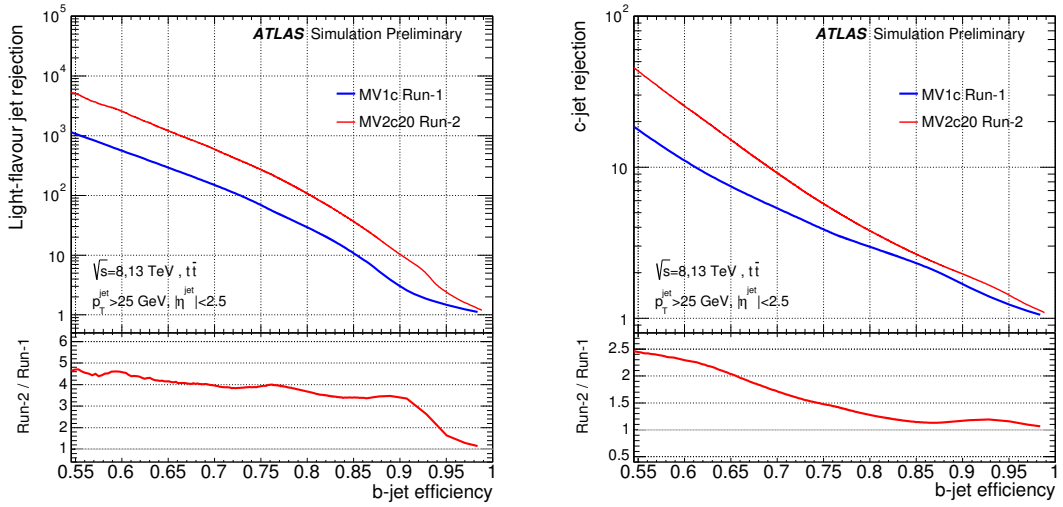

(a) (b)

Figure 5.2: (a) The light and (b) c-jet rejection versus b-jet efficiency for the MV1c b-tagging algorithm using the Run-1 detector and reconstruction software (blue) compared to the MV2c20 b-tagging algorithm using the Run-2 setup (red) [62].

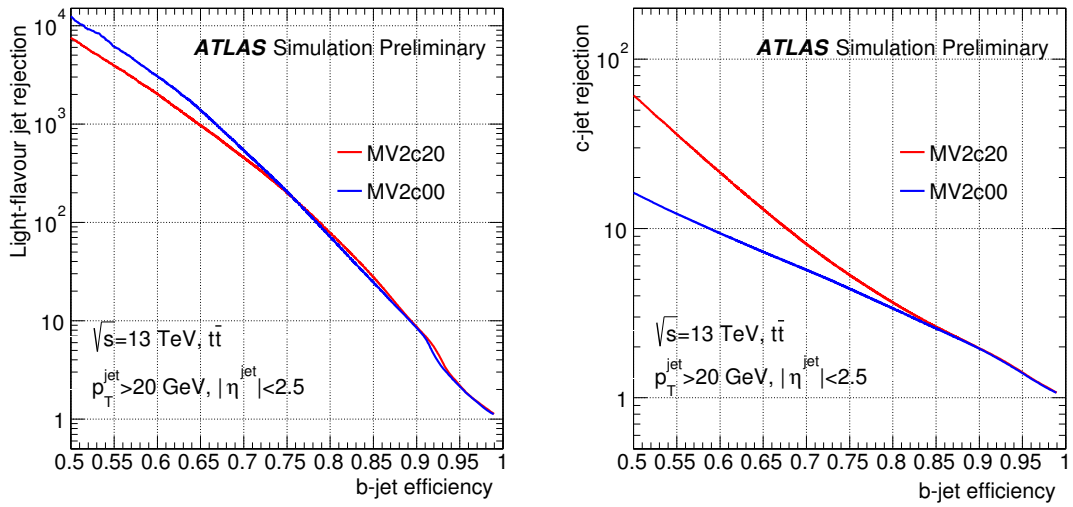

(a) (b)

Figure 5.3: The (a) light-jet rejection and (b) c-jet rejection as a function of the b-tagging efficiency for two b-tagging algorithms MV2c00 and MV2c20 (0% 20% c-quark content used in training respectively). The efficiencies and is b-tag rates are estimated using simulated $t\bar{t}$ events [62].

***b*-tagging with track jets** The standard b-tagging algorithm in ATLAS uses calorimeter jets to which groups of tracks have been associated. The b-tagging algorithms are applied to these tracks and the calorimeter jet is b-tagged. However, it is possible to directly run the jet clustering algorithms on tracks without using the associated calorimeter jet. These approach offers several advantages. Track jets are clustered with tracks chosen to come exclusively from the primary vertex, significantly reducing the performance dependence on pile-up. This is important when reconstructing low-p_{T} b-hadrons that can be present in highly boosted states if the b-hadron is produced in the opposite to the boost of the decaying particle. These relatively low p_{T} hadrons may be lost due to a higher p_{T}-threshold chosen for calorimeter to reduced pile-up [63]. For example usually the p_{T} threshold for calorimeter jets is $p_{\mathrm{T}} > 25$ GeV while for track jets it is possible to use jets with $p_{\mathrm{T}} > 10$ GeV. Finally, for highly boosted particles the merging of R=0.4 causes great inefficiencies when trying to reconstruct the mass of the parent particle. Reducing the radius helps to better identify the b-hadron decays and avoid merging. Fig. 5.4 shows the reconstruction efficiency of a graviton decaying to $b\bar{b}$ using track jets of different radii and calorimeter jets with $R = 0.3$.

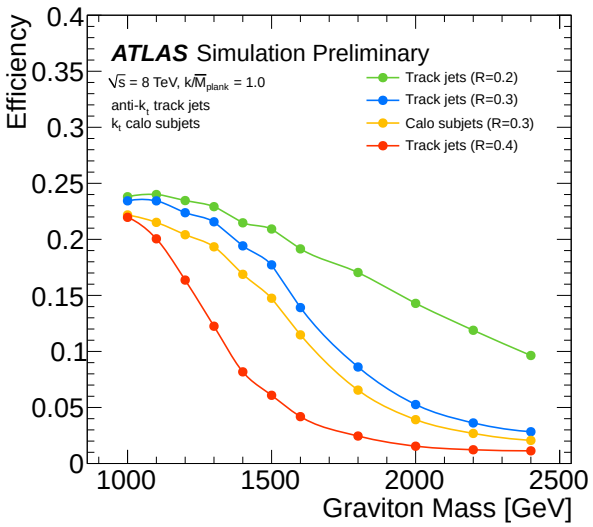

Figure 5.4: Graviton reconstruction efficiencies for using track jets with radii 0.2,0.3,0.4 and calorimeter jets with radius 0.3 [63].

For the HEPTopTagger performance studies(Section 7), calorimeter jets clustered the anti-k_t algorithm R=0.4 are used. The MV1 algorithm at a b-tagging efficiency of 70% is used to classified these jets as b-tagged. At this working point the light-jet (c-jet) rate is reduced by a factor of 137 (5). For the fully hadronic resonance search(Section 8), track jets with clustered with the anti-k_t algorithm R=0.2 are used. The MV2c10 algorithm with an efficiency of 70% is used is used to classify these jets as b-tagged. At this working point the light-jet (c-jet) rate is reduced by a factor of 120 (7) [64].

5.5.2 Calibration

In addition to b-jet identification, it is crucial to compare the b-tagging efficiency obtained from the simulation to the one obtained in data. Moreover, it is important to estimate the systematic uncertainties from the modeling of these efficiencies in different kinematic regimes. By comparing the efficiencies in data and simulation is it possible to obtain scale factors to adjust the efficiencies obtained in simulation to the efficiencies observed in data. Furthermore, this comparison is carried out as a function of jet p_{T}. The b-tagging scale factors are defined as:

$$\kappa_{\varepsilon_b}^{\mathrm{data/sim}}(p_{\mathrm{T}}) = \frac{\varepsilon_b^{\mathrm{data}}(p_{\mathrm{T}})}{\varepsilon_b^{\mathrm{sim}}(p_{\mathrm{T}})} \tag{5.2}$$

where $\varepsilon_b^{\mathrm{sim}}$ is the fraction of b-jets which are tagged in simulated events where the jet flavor is defined by matching jets to generator level partons. In physics analysis, the p_{T}-dependent scale factors are applied as weights to the jets in the simulation to correct the MC efficiency to the one observed in data.

5.6 Missing Energy

Even though neutrinos and other possibly existing weakly interacting particle escape the detector undetected, it is possible to infer their presence by measuring the transverse momentum imbalance occurring during the pp collision. This is achieved by measuring the vectorial sum of the transverse energy from every significant deposit energy in the

detector [65]:

$$E_T^{miss} = -\sum_i \vec{p}_{T_i} \tag{5.3}$$

$E_{\mathrm{T}}^{\mathrm{miss}}$ receives contributions from reconstructed electrons, photons, hadronically decaying taus, jets and muons. All of these objects are calibrated. Additionally, a soft term $E_{x(y)}^{miss,\mathrm{SoftTerm}}$ is added to account for low energy particles not reaching the high threshold required for object reconstruction e.g. only jets with a $p_{\mathrm{T}} > 20$ GeV are accounted for. The soft term is comprised of LCW topoclusters and tracks which have not been matched to any topocluser or reconstructed object. For Run2, the soft term has been modified to come entirely from tracks in order to avoid pile-up contributions that affect the topoclusters. Finally to avoid double counting, the expected energy loss of muons is subtracted from the soft term,

$$E_{x(y)}^{miss} = E_{x(y)}^{miss,e} + E_{x(y)}^{miss,\gamma} + E_{x(y)}^{miss,\tau} + E_{x(y)}^{miss,\mathrm{jets}} + E_{x(y)}^{miss,\mathrm{SoftTerm}} + E_{x(y)}^{miss,\mu}. \tag{5.4}$$

E_T^{miss} is a challenging observable to measure because its inputs are all the reconstructed objects in ATLAS. Therefore miscalibration in any of these objects will have an impact in E_T^{miss}. In addition, all the systematic uncertainties of the reconstructed objects enter the final systematic uncertainty of the E_T^{miss}.

6 The HEPTopTagger

In the following chapter the HEPTopTagger algorithm and the underlying techniques are introduced. The preferred algorithms to create jets in the LHC experiments, Sequential Recombination Algorithms are introduced in Section 6.1.1. The basic motivation for boosted physics and jet substructure is presented in Section 6.1.2. Techniques to remove underlying event and pile-up from the large-R jets commonly referred to as "grooming techniques" such as trimming or filtering are introduced in Sections 6.1.3 and 6.1.4 respectively. The HEPTopTagger algorithm, its features and its steps are presented in Section 6.2. Finally other top tagging techniques relevant for the top tagging comparisons are briefly introduced in Section 6.3.

6.1 Jets and Jet Substructure

6.1.1 Sequential Recombination Algorithms

By analyzing the tracks and energy deposits of hadrons in a jet, it is possible to infer the characteristics of the original quark or gluon. Since partons have divergent probabilities in perturbation QCD, a jet is not universally defined. The definition of a jet depends of the prescription on how to group particles and how to assign momentum to the resulting jet, i.e. a jet algorithm. There are several ways to construct a jet algorithm. However, a jet algorithm should always be infrared (IR) and collinear safe. This means that jets found in an event, should remain unchanged by a collinear splitting or the addition of a soft emission.

IR safety requires jets to not change if there is an additional soft emission from the parton. Since soft emissions are ubiquitous in hadronic showers this is an crucial requirement otherwise the definition of a jet would be constantly changing and it would not be possible to compare results with theory. In Fig. 6.1, an IR safe algorithm would always resolve the two hard jets created by the W-boson decay products, even if there are soft gluon emissions as seen in (a) and b). An IR unsafe algorithm would merge the two jets into one (c).

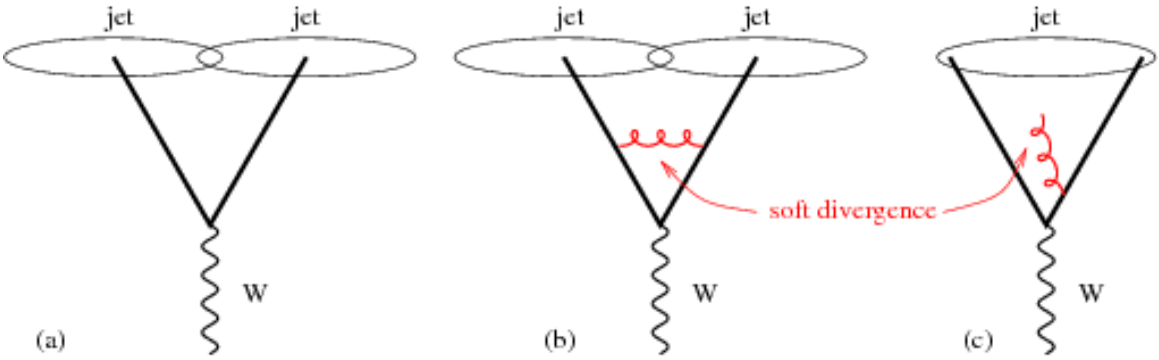

Figure 6.1: The decay of a W-boson into two hard quarks, which are independently resolvable for the given jet algorithm parameters (a). After the emission of a soft gluon, an IR safe jet algorithm still observes two separate jets (b), while IR unsafe algorithms merge the two jets into one (c) [66].

Collinear safety requires stability against single parton splitting, such as a quark radiating a gluon or a gluon splitting into two quarks. Just as IR safety, collinear safety is an indispensable requirement since hard-scatter partons go through many splittings during the hadronic shower. Fig. 6.2 shows how parton splitting changes the number of jets in collinear unsafe algorithms. Here the replacement of a quark with a virtual gluon correction by a distinct quark and a distinct gluon would cause the original jet to be split into two. IR or collinear unsafe jet algorithms can cause the reconstructed jet multiplicity to vary, which changes the observed physics. These changes must be avoided. Many collinear-IR safe algorithms are available through the FastJet package [67] including sequential recombination algorithms. Sequential recombination algorithms meet the IR and collinear safety requirements. They have become the standard jet finder and jet reconstruction algorithms at the LHC experiments. These are the only kind of algorithms used in this thesis.

Sequential Recombination Algorithms merge pairs of objects i and j by adding their four-momenta. They first creates a list of all inout objects (either hadrons, topo-clusters or tracks) in an event. Then, two distances are obtained for each of these objects: one between the object and its closest neighbor, as defined in Eq. (6.1) and the distance between the object and the beam as defined in Eq. (6.2)

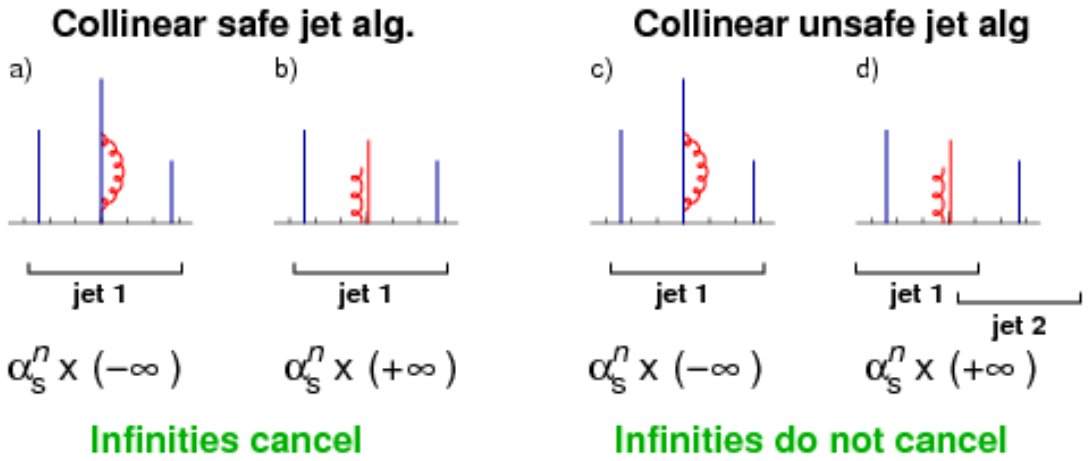

Figure 6.2: Difference between collinear safe and unsafe algorithms. Parton p_{T} is represented by the height of the line, while the horizontal axis represents the parton rapidity. All algorithms are stable against the gluon correction to the quark propagator (a and c), which is by construction given that no particle is emitted. However, the gluon correction should be canceled in perturbation theory by gluon radiation, where the gluon and parton share the p_{T}. This feature is provided by collinear safe algorithms (b), but not collinear unsafe algorithms (d), where the perturbative approach breaks down. The presence of an extra parton in the collinear unsafe algorithm leads to the reconstruction of two separate jets rather than one, changing the observed hard jet multiplicity [66].

$$d_{ij} = \min(p_{Ti}^{2n}, p_{Tj}^{2n}) \frac{\Delta R_{ij}^2}{R^2}, \tag{6.1}$$

$$d_{iB} = p_{Ti}^{2n}. \tag{6.2}$$

In Eqs. (6.1) and (6.2), p_{Ti} is the transverse momentum of the object. In Eq. (6.1), n is an integer, $\Delta R_{ij} = \sqrt{(y_i - y_j)^2 + (\phi_i - \phi_j)^2}$ is a measure of the opening angle between objects i and j. These two distance are then compared:

- If $d_{iB} < d_{ij}$ then the object is "closer" to the beam than to other objects in the event, so it is defined as a jet and removed from the list.
- If $d_{iB} > d_{ij}$ then the two objects i and j are combined into one (by adding their four momenta), forming a new object. This procedure continues until there are no more objects left on the list.

The difference between jet algorithms comes from the value of n in the exponent of p_{Ti} in Eq. (6.1):

- $n = 1$: the k_t algorithm [68]. Objects with smaller p_{T} tend to be clustered first.
- $n = 0$: the Cambridge/Aachen algorithm [69, 70]. Objects are combined based only on their angular separation from one another and the beam.
- $n = -1$: the anti-k_t algorithm [71]. Objects with higher p_{T} tend to be clustered first.

The jet distance parameter R controls the size of the jets in $y - \phi$ space, and can be referred to as the jet "radius". However, what this parameter does exactly is to ensure that particles separated by $\Delta R < R$ at a given clustering stage are not combined and that an object can only be promoted to a jet if there are no other objects within $\Delta R < R$ [72]. Typical jet distance parameter in the ATLAS experimente are $R = 0.4$ or $R = 0.6$ for small jets, and R = 1.0, 1.2 and 1.5 for large jets.

6.1.2 Boosted Physics and Jet Substructure

At the LHC, the heaviest known particles in Standard Model ($Z^{\pm}$, Z^0, Higgs boson, top quark) can be produced with a transverse momentum greatly exceeding their rest mass i.e. they are boosted. Additionally new possible particles (predicted by BSM theories in the same mass range or even heavier) would decay to top quarks and the top quarks in turn would be boosted. When boosted particles decay, they exhibit a highly collimated topology in the detector (see Fig. 6.3). A complete overview of boosted objects at the LHC is given in the report from BOOST 2011 [72]. For a boosted particle, the higher its p_{T}, the closer its decay products are as given by the following rule of thumb:

$$\Delta R \sim \frac{2m}{p_T} \tag{6.3}$$

This fact indicates that standard reconstruction techniques are not adequate to reveal the precedence of a boosted heavy particle. Many efforts have been performed to identify

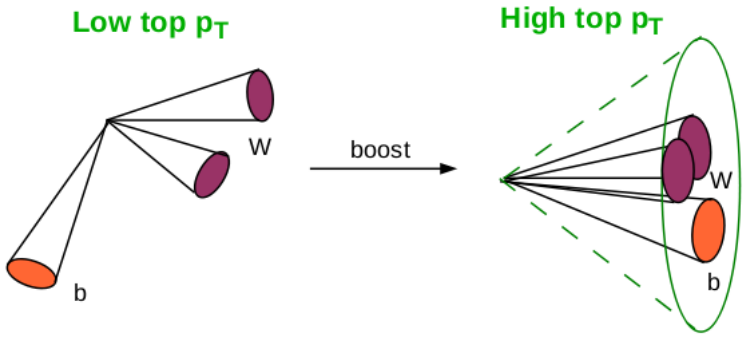

Figure 6.3: Comparison between top quark decays, with low and high p_T [73].

and reconstruct boosted W bosons, Higgs, etc [74]. This study focuses on the boosted top quarks. In the case of the boosted top quark, standard top quark identification is not effective: b-tagging is difficult as a consequence of crowded and unresolved tracks, W-boson decay products are not isolated from each other, and the measured top quark mass may differ from m_{top} due to an increase in QCD radiation. New tools have been developed to identify and reconstruct boosted top quarks. A strong motivation to study highly boosted top quarks is that heavy s-channel resonances can decay to $t\bar{t}$ pairs. The higher the New Physics mass scale is pushed by LHC searches, the more boosted these top quarks become if these new states exist. Large-R jets are needed to catch all decay products of the boosted top quark. However the larger the jet becomes, the more sensitive it becomes to UE and pile-up. To avoid unwanted changes in reconstructed variables, removing UE and pile-up is crucial. In the following relevant jet grooming techniques are introduced. The HEPTopTagger uses a combination of grooming techniques which are introduced in Section 6.2.

6.1.3 Trimming

The trimming algorithm [75] takes advantage of the fact that contamination from pile-up, multiple parton interaction and ISR in the reconstructed large-R jet are much softer than the outgoing partons associated with the hard-scatter and their FSR [76]. The constituents of a large-R jet with size R and with transverse momentum p_T are reclustered

into smaller subjets using the k_t algorithm. Subjets with $p_T/p_T^{\text{subjet}} < f_{\text{cut}}$ are removed. The remaining constituents form the trimmed jet. The trimming procedure is shown in Fig. 6.4.

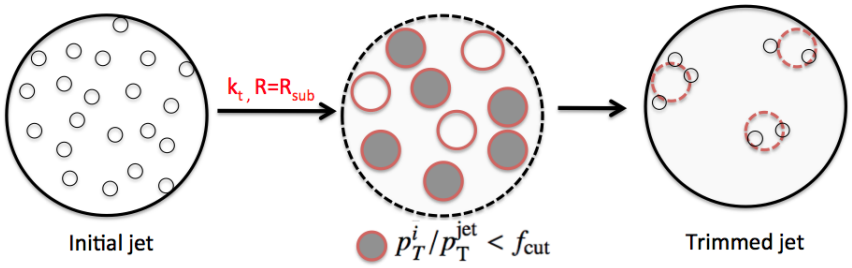

Figure 6.4: Diagram depicting the trimming procedure [77].

6.1.4 Filtering

The filtering algorithm [74] works similarly to trimming algorithm. The constituents of a large-R jet with size R and with transverse momentum p_{T} are reclustered into smaller subjets usually of size $R = 0.3$ using the C/A algorithm. Finally only a number N_{keep} of the hardest subjets is kept. The resulting subjet four-vectors are added and form the filtered jet.

6.2 The HEPTopTagger Algorithm

The HEPTopTagger (Heidelberg-Eugene-Paris Top Tagger) [78] is an algorithm designed to tag and fully reconstruct hadronically decaying top quarks. The main features of the HEPTopTagger are the following:

- Due to its distance parameter of R=1.5, the algorithm is able to tag top quarks with p_{T} in the range of $200 - 350$ GeV[4]. From Eq. (6.3), the lower the p_{T} of the top quark, the less collimated its decay products are. The partonic ΔR_{bjj} as a function of the top quark p_{T} for a Standard Model $t\bar{t}$ sample is shown in Fig. 6.5.

[4]Another approach which is able to tag top quarks with in this p_{T}-range is the newly introduced HEPTopTagger2 [79] which adapts the size of the jet distance parameter according to the reconstructed mass of the top quark.

The figure indicates the jet size necessary needed to catch all decay products of a top quark with a given p_{T}. A jet distance parameter $R = 1.5$ is well suited to catch all decay products of top quarks with $p_{\mathrm{T}} > 200$ GeV.

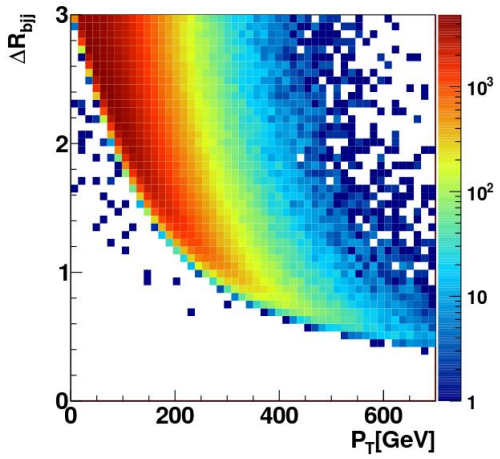

Figure 6.5: Partonic ΔR_{bjj} as a function of the top quark p_{T} for a Standard Model $t\bar{t}$ sample [78].

- It uses the C/A algorithm[5] with a mass drop criterion. As detailed in Section 6.1.1, the C/A algorithm cluster particles closest in distance. Therefore, the jet has an "angular-aware" substructure. This improves the mass resolution of the reconstructed object [74]. In addition, QCD-initiated jets processed by this method produce a relatively featureless mass spectrum. However, in the absence of any momentum scale, the last clustering step often involves soft radiation on the edges and therefore it is unrelated to the heavy object. C/A based substructure algorithms must therefore work backwards iteratively through the jet clustering and stop when the subjets meets some specific hardness requirement. A mass drop criterion is applied in the case of the HEPTopTagger, until all objects have a mass lower than a certain parameter. The mass-drop procedure is sketched in Fig. 6.6b. This ensures that wide angle underlying events (UE) and pile-up (PU) are removed

[5]The anti-k_t jet algorithm clusters high-p_{T} objects first, even if they are geometrically separated by a large distance. This algorithm is therefore not suited for the HEPTopTagger approach where the substructure of the fat jet is analyzed by undoing the last clustering steps.

from the event.

- The mass-drop procedure removes a substantial amount of wide-angle UE/PU. However, as moderately boosted regimes are explored and jet radii become larger (of $O(1)$), UE and PU contamination remains a major problem as they scale to jet mass as R^4 [80]. To further remove unwanted radiation and refine the subjets, a filtering procedure is applied to the jet. The filtering procedure consists of reclustering the substructure constituents with the C/A algorithm, using $R = \min(0.3, \Delta R_{subjets}/2)$. This enables the capture of possible gluon radiation in the heavy particle decay, while still eliminating much of the UE/PU.

6.2.1 HEPTopTagger Steps

In the following the steps of the HEPTopTagger algorithm are explained in detail.

1. **Find C/A R=1.5** Define a large-R jet J using the C/A algorithm with $R = 1.5$.

2. **Mass-Drop:** Undo the last clustering step of C/A in the jet J and obtain two subjets j_1 and j_2 with $\mathrm{m}_{j_1} > \mathrm{m}_{j_2}$. If subjets j_1 has 80% of the mass of the original C/A R=1.5 jet(m_J) or more, discard jet j_2. Otherwise keep both. Proceed iteratively with all subjets until all have a mass $\mathrm{m}_{cut} < 50$ GeV.

3. **Filtering:** Take all three-pairings of the previously obtained subjets and filter them (using the C/A algorithm) The filtering step consists on running the C/A algorithm using a distance parameter than can be different depending on the event topology ("dynamic radius"), $R_{\mathrm{filter}} = \min(0.3, \Delta R_{subjets}/2)$ where $\Delta R_{subjets}$ is the distance of the subjets obtained after the mass-drop criterion procedure. Next use the 5 hardest filtered constituents and calculate their jet mass. For less than 5 filtered constituents use all of them. Finally, select the set of three subjet pairings with a jet mass closest to the top quark mass (m_{top}). A dedicated calibration using radii 0.2 - 0.6 in steps 0.05 is applied for jets clustered these filtered subjets. If the dynamic distance parameters takes a value in between, it is rounded to the closest

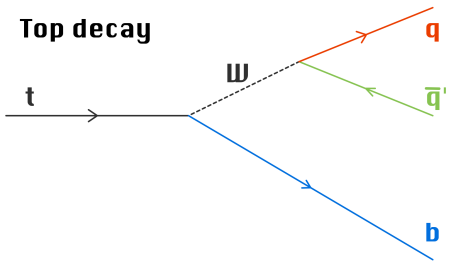

(a) Start with the following topology [81].

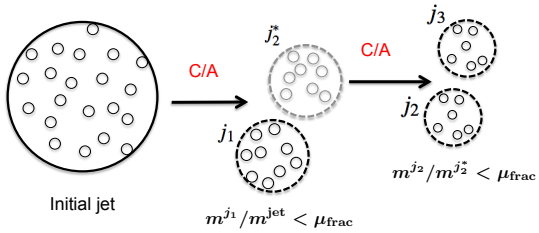

(b) Find a C/A R=1.5 jet. The mass-drop criterion is applied iteratively, following the highest subjet mass line through the clustering history until all objects have a mass < 50 GeV [77].

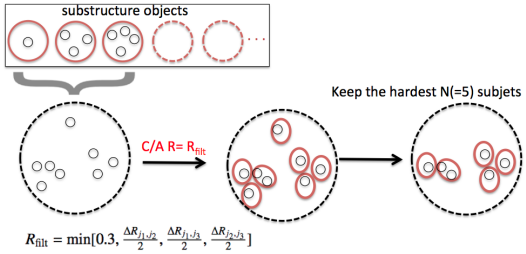

(c) For every triplet-wise combination of the substructure objects found in (b), apply filtering using a dynamic radius. After filtering select the $N_{subjet} = 5$ leading p_{T} subjets [77].

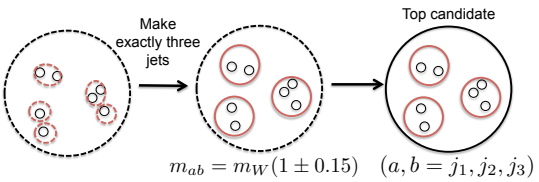

(d) Recluster the constituents of the N_{subjets} subjets into exactly three subjets to make the top quark candidate for this triplet-wise combination of substructure objects [77].

Figure 6.6: Sketches depicting the HEPTopTagger algorithm steps.

calibrated value. This calibration is necessary to obtain high tagging efficiency and background rejection.

4. **Top Quark Mass and W Boson Mass Requirements:** The knowledge of the top quark and W boson masses provides two constraints, $m_{123} = m_t$ and $m_{jk} = m_W$ for the (j, k) exclusive subjets in the identification of the top quark. An additional mass relation that can be exploited. The three subjets j_k ignoring smearing and assuming $p_i^2 \sim 0$ give:

$$m_t^2 \equiv m_{123}^2 = (p_1+p_2+p_3)^2 = (p_1+p_2)^2+(p_1+p_3)^2+(p_2+p_3)^2 = m_{12}^2+m_{13}^2+m_{23}^2 \tag{6.4}$$

which is the surface of a sphere with radius m_t in (m_{12}, m_{13}, m_{23}) space. For a fixed m_{123}, one can choose exactly two variables to describe the kinematics of the

event: m_{23}/m_{123} and $\arctan(m_{13}/m_{23})$ which means that m_{12}/m_{123} can be derived as,

$$1 = \left(\frac{m_{12}}{m_{123}}\right)^2 \left(1 + \left(\frac{m_{13}}{m_{123}}\right)^2\right) + \left(\frac{m_{23}}{m_{123}}\right)^2. \tag{6.5}$$

Assuming $m_{123} = m_t$, the condition $m_{12} = m_W \pm 15\%$ reads as Eq. (6.6). The selection criteria shown in equations Eq. (6.7) and Eq. (6.8) are built similarly. In the m_{23}/m_{123} - $\arctan(m_{13}/m_{23})$ space, top quark candidates lie in well defined regions that can be separated by the selection criteria presented in equations Eq. (6.6), Eq. (6.7) and Eq. (6.8) as seen in Fig. 6.7. A more detailed motivation is given in [78]. The selection criteria are the following:

$$0.2 < \arctan\left(\frac{m_{13}}{m_{12}}\right) < 1.3 \quad \text{and} \quad R_{\text{min}} < \frac{m_{23}}{m_{123}} < R_{\text{max}}, \tag{6.6}$$

$$R^2_{\text{min}}\left(1 + \left(\frac{m_{13}}{m_{12}}\right)^2\right) < 1 - \left(\frac{m_{23}}{m_{123}}\right)^2 < R^2_{\text{max}}\left(1 + \left(\frac{m_{13}}{m_{12}}\right)^2\right) \text{ and } \frac{m_{23}}{m_{123}} > 0.35, \tag{6.7}$$

$$R^2_{\text{min}}\left(1 + \left(\frac{m_{12}}{m_{13}}\right)^2\right) < 1 - \left(\frac{m_{23}}{m_{123}}\right)^2 < R^2_{\text{max}}\left(1 + \left(\frac{m_{13}}{m_{12}}\right)^2\right) \text{ and } \frac{m_{23}}{m_{123}} > 0.35. \tag{6.8}$$

The HEPTopTagger algorithm now proceeds to construct exactly three jets subjets j_1, j_2, j_3 as shown in Fig. 6.6d. from the five filtered constituents, ordered by (p_{T}). If the subjets masses (m_{12},m_{13},m_{23}) satisfy **one** of the selection criteria just mentioned, the four vectors of the 3 subjets are added and the sum is taken a as a top quark candidate.

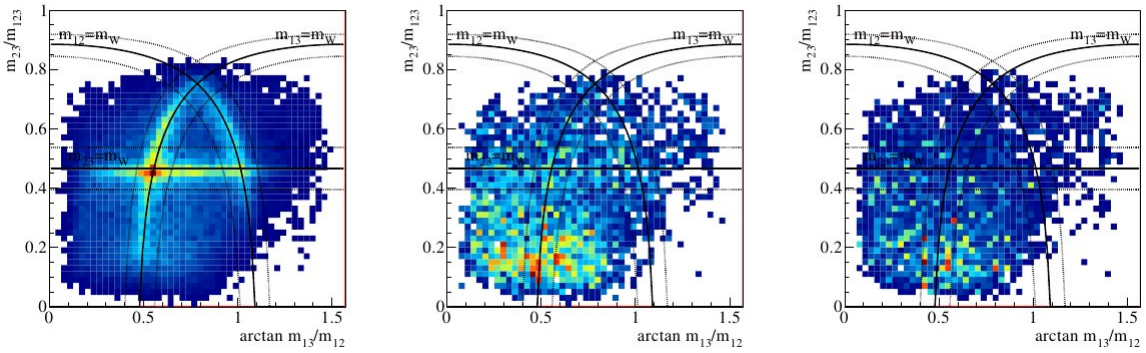

Figure 6.7: The distribution of events in the arctan m_{13}/m_{12} vs m_{23}/m_{123}. Samples shown are $t\bar{t}$ (left), W +jets (center) and pure QCD jets (right). More densely populated regions of the phase space appear in red [78].

5. Finally, require the combined p_{T} of the 3 subjets to exceed 200 GeV.

6.2.2 Improved $m_{t\bar{t}}$ Reconstruction

The HEPTopTagger is able to reconstruct $m_{t\bar{t}}$ by adding the four-vector of the any tagged top quarks. The HEPTopTagger is designed to capture any possible final state radiation (FSR) radiation coming from the top quark, hence FSR does not pose a problem for reconstructing a possible Z' boson, as long as the Z' boson decays to on-shell tops. If the Z' boson decays to off-shell tops, these in turn decay to on-shell tops giving off FSR. These additional FSR will mis-aling the Z' boson reconstruction since the HEPTopTagger reconstructs top quarks at the moment of decay. Since the hard radiated gluon does not enter the top reconstruction to top tag will pass, but the $m_{Z'}$ will be underestimated [79]. The truth $m_{t\bar{t}}$ along with the $m_{t\bar{t}}$ returned by the HEPTopTagger with and without any FSR are shown in Fig. 6.8a. Clearly with FSR, the $m_{t\bar{t}}$ exhibits a large tail toward lower values.

Instead of using the four-momentum of the tagged tops to reconstruct the Z' boson, the four-momenta of the two C/A R=1.5 jets is used. Using this scheme, it is possible to catch any FSR which was previously discarded by the HEPTopTagger. However, to used the large-R jets to reconstruct the Z' boson, it is necessary to groom the jets to

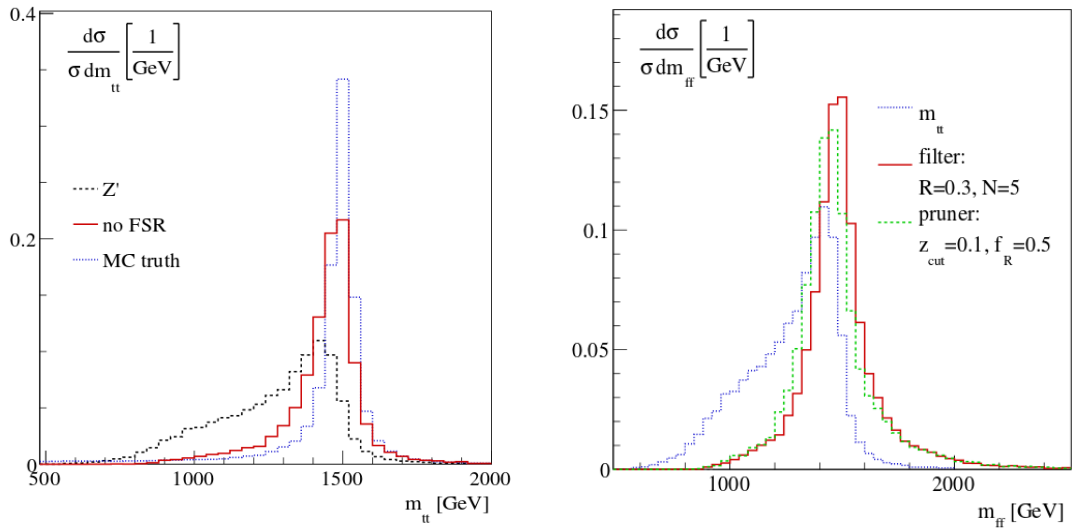

(a) (b)

Figure 6.8: (a) Effect of final-state radiation on the invariant mass of the tagged and reconstructed $t\bar{t}$ system $m_{t\bar{t}}$ for the Z' signal (b) and different approaches to reconstruct the Z' boson resonance mass peak [79].

remove large amounts UE and pile-up collected. The standard $m_{t\bar{t}}$ reconstruction, along with the $m_{t\bar{t}}$ reconstruction using the filtered and pruned C/A R=1.5 jets are shown in Fig. 6.8b. Both grooming approaches, filtering and pruning, work similarly and return a symmetric Z' boson mass around 1.5 TeV. For the $t\bar{t}$ fully hadronic resonance search the filtering approach has been applied with the parameters $R = 0.3$ and $N = 5$. The improved mass resolution eventually helps in the fully hadronic $t\bar{t}$ resonance search by making a possible signal more visible and thus improving the sensitivity and CL limits.

6.3 Other Top-tagging Approaches

Other top tagging approaches commonly used in ATLAS are introduced in order to provide some context for MC-only comparisons presented in Section 7.4. In these comparisons the performance of the HEPTopTagger studied in the thesis is compared in several p_{T} bins to the following top tagging approaches.

6.3.1 Substructure-variable taggers

The choice of trimmed anti-k_t $R = 1.0$ jets for substructure-based analyses was studied in [77], including comparisons of different grooming techniques and parameters. In the following, a brief summary of the top-tagging techniques compared to the HEPTopTagger in Section 7.4 is given.

- *trimmed mass* - The mass, m, of a trimmed anti-k_t $R = 1.0$ jet is less sensitive to contributions from underlying event and pile-up activity than untrimmed jet mass. On average, large-R jets containing from top quarks have a larger mass than light quark/gluon jets.

- *k_t splitting scales* The k_t splitting scales [82], measure the scale of the last recombination steps in the k_t algorithm, which clusters high-momentum and large-angle jets last. Therefore, the k_t splitting scales the scale of the merging of the decay products of massive particles. They are determined by reclustering the constituents of the trimmed large-R jet with the k_t algorithm and are defined as

$$\sqrt{d_{ij}} = \min(p_{\mathrm{T}i}, p_{\mathrm{T}j}) \times \Delta R_{ij} \quad , \tag{6.9}$$

  where ΔR_{ij} is the angular distance between two subjets i and j in the η–ϕ space, and $p_{\mathrm{T}i}$ and $p_{\mathrm{T}j}$ are the corresponding subjet p_{T}. The $\sqrt{d_{12}}$ observable is obtained from the subjets merged in the last k_t clustering step. The $\sqrt{d_{23}}$ is obtained from the second-to-last merging. The expected value $\sqrt{d_{12}}$ for a hadronic top quark decays fully contained in a large-R jet is approximately $m_t/2$, where m_t is the top quark mass. The second splitting scale $\sqrt{d_{23}}$ has an expected value of approximately $m_W/2$.

- *N-subjetiness* The N-subjettiness variables τ_N [83, 84] describe how well jets are described as containing N or fewer subjets. The N subjets are obtained by an exclusive k_t clustering of the constituents of the trimmed large-R jet. The τ_N is given by the p_{T}-weighted sum of the distances of the constituents from the subjet

axes:

$$\tau_N = \frac{1}{d_0} \sum_k p_{\mathrm{T}k} \times \Delta R_k^{\mathrm{min}} \qquad \text{with} \qquad d_0 \equiv \sum_k p_{\mathrm{T}k} \times R \quad , \tag{6.10}$$

where $p_{\mathrm{T}k}$ is the p_{T} of constituent k, $\Delta R_k^{\mathrm{min}}$ is the distance between constituent k and the axis of the closest subjet, and R is the jet distance parameter of the large-R jet. The ratio τ_3/τ_2 or τ_{32} provides discrimination between large-R jets formed from hadronically decaying top quarks with high p_{T} which posses a 3-prong subjet structure (small values of τ_{32}) and non-top quark jets with two or fewer subjets (large values of τ_{32}). Similarly, the ratio $\tau_2/\tau_1 \equiv \tau_{21}$ is used to separate large-R jets with a 2-prong structure (hadronic decays of Z or W bosons) from jets with only one hard subjet, such as those produced from light quarks or gluons.

7 HEPTopTagger Performance at ATLAS

The decay products of top quarks with high p_{T} ($\gtrsim$ 200 GeV) will be collimated. Classical reconstruction approaches do not work because small-R jets overlap each other. By collecting all decay products in a large-R jet ($R \gtrsim 0.8$), boosted techniques can determine if the jet originates from a heavy particle or multijet production or any other source of background. General boosted tagging techniques were explained in detail in Section 6.1.2. The HEPToptagger combines several boosted techniques to identify hadronically decaying top quarks with $p_{\mathrm{T}} \gtrsim 200$ GeV. It is explained in detail in Section 6.2. Unless stated otherwise the term "large-R-jet" is used as a interchangeably with "C/A R=1.5 jet".

The top-tagging efficiency of the HEPTopTagger (and in general of any top tagger) is usually measured in the $t\bar{t}$ lepton plus jets channel, where one top quark decays to $bq\bar{q}$ and the other one to $b\ell\nu_{\ell}$. This channel provides a very pure sample of top quarks where detailed studies of any top-tagging approaches can be conducted. In contrast, in order to measure the mis-identification efficiency (or mistag rate), multijet samples free of top quarks are employed. Section 7.1 describes the event-wide selection while Section 7.2 describes the lepton plus jets selection and top-tagging efficiency results with the associated systematic uncertainties. The top-tagging mistag rate selection and the results with their associated systematic uncertainties are presented in Section 7.3. A summary and conclusion are given in Section 7.5. The following material closely follows [85].

7.1 Event Selection

The following event selection was applied to both the top-tagging efficiency and mistag rate measurements described in Section 7.2 and Section 7.3 respectively. Data used for the top-tagging studies were recorded in 2012 at $\sqrt{s} = 8$ TeV with the ATLAS detector and correspond to an integrated luminosity of 20.3 fb^{-1} [86]. Data are used only if all subsystems of the detector as well as the trigger system were fully functional.

Baseline quality criteria reject contamination from detector noise, non-collision beam backgrounds, and other spurious effects. Events are required to have at least one reconstructed primary vertex with at least five associated ID tracks with a $p_{\mathrm{T}} > 400$ MeV and are consistent with the LHC beam spot [87]. Finally, events containing anti-k_t $R = 0.4$ jets arising from non-collision background (e.g cosmic rays, beam gas) are rejected [88].

7.2 HEPTopTagger Top Tagging Efficiency

The lepton plus jets selection is applied in the muon and electron channel. For the muon channel, events are required to pass at least one of two muon triggers: isolated muons with $p_{\mathrm{T}} > 24$ GeV or muons with $p_{\mathrm{T}} > 36$ GeV without isolation. Exactly one fully reconstructed muon is required. Muons are rejected if they are close to an anti-k_t $R = 0.4$ jet that has $p_{\mathrm{T}} > 25$ GeV. The rejection occurs if $\Delta R(\mu, \mathrm{jet}) < (0.04 + 10\ \mathrm{GeV}/p_{\mathrm{T}}^{\mu})$. The p_{T}-dependence of the isolation requirement causes the "isolation cone" to shrink guaranteeing an efficient isolation with higher top quark boosts. Events in the muon channel are discarded if they contain an electron candidate.

For the electron channel, events are required to pass at least one of two triggers: isolated electrons with $p_{\mathrm{T}} > 24$ GeV or electrons with $p_{\mathrm{T}} > 60$ GeV without the isolation requirement. Exactly one electron $E_{\mathrm{T}} > 25$ GeV is required. At higher top quark boosts, the top quark decay products will be more collimated. Therefore the electron may contribute significantly to the energy of an adjacent jet. To avoid double counting of energy, an electron-in-jet overlap removal is carried out and described in the following. The electron momentum is subtracted from the jet momentum before kinematic requirements are applied to the jet, so that jets close to an electron often fall below the jet p_{T} threshold. If the electron-subtracted jet still passes the selection criteria for anti-k_t $R = 0.4$ jets and the electron is still close, the electron is considered not isolated. In this case, the electron is removed from the event and the original non-subtracted jet is kept. Events in the electron channel are discarded if a muon candidate is identified.

The following selection criteria are required to ensure the events contain a W boson. The events are required to have $E_{\mathrm{T}}^{\mathrm{miss}} > 20$ GeV. The scalar sum of $E_{\mathrm{T}}^{\mathrm{miss}}$ and the

transverse mass of the leptonically decaying W-boson candidate must satisfy $E_T^{miss} + m_{\mathrm{T}}^W > 60$ GeV, where $m_{\mathrm{T}}^W = \sqrt{2p_{\mathrm{T}}^{\ell} E_{\mathrm{T}}^{\mathrm{miss}}(1-\cos\Delta\phi)}$ is calculated from the transverse momentum of the lepton, p_{T}^{ℓ}, and $E_{\mathrm{T}}^{\mathrm{miss}}$ in the event. The variable $\Delta\phi$ is the azimuthal angle between the lepton momentum and the $E_{\mathrm{T}}^{\mathrm{miss}}$ direction.

For the $t\bar{t}$ lepton plus jets selection, the largest background contribution comes from W+jets production. Removing the W+jets production contribution is desired since large systematic uncertainties, such as the W+jets normalization uncertainty, would affect the final measurement. Therefore, at least two b-tagged anti-k_t $R = 0.4$ jets with $p_{\mathrm{T}} > 25$ GeV and $|\eta| < 2.5$ are required. In $t\bar{t}$ events with high-p_{T} top quarks, the b-quark coming from the leptonic decay of a top quark is often close to the lepton. Therefore, at least one b-tagged jet is required to be within $\Delta R = 1.5$ of the lepton. A second b-tagged jet away from the lepton is required with $\Delta R(\ell, b\text{-tagged jet}) > 1.5$. This b-tagged jet is expected to originate from the b-quark from the hadronic top-quark decay.

Events are required to contain at least one large-R jet that fulfills the requirement $\Delta R(\ell, \text{large-}R\text{ jet}) > 1.5$. This criterion increases the probability that the large-R jet originates from a hadronically decaying top quark. If several large-R jets in an event satisfy the criteria mentioned, only the highest-p_{T} jet is considered. In simulated events, if a hadronically decaying top quark is present, large-R jets are classified as *matched* or *not matched* to the top quark. *Matched* jets have a separation $\Delta R < 1.0$ with respect to the hadronically decaying top quark after FSR. Correspondingly, non-matched jets are those with a $\Delta R > 1.0$. The top-tagging efficiency is defined in each jet p_{T} and η bin i as:

$$f_{\mathrm{data,i}} = \left(\frac{N_{\mathrm{data},i}^{(\mathrm{tag}),} - N_{t\bar{t}\text{ non-matched},i}^{(\mathrm{tag})} - N_{\text{non-}t\bar{t},i}^{(\mathrm{tag})}}{N_{\mathrm{data},i} - N_{t\bar{t}\text{ non-matched},i} - N_{\text{non-}t\bar{t},i}} \right) \quad (7.1) \qquad f_{\mathrm{MC,i}} = \left(\frac{N_{MC,i}^{(\mathrm{tag})}}{N_{MC,i}} \right) \quad (7.2)$$

where

- $N_{\mathrm{data},i}^{(\mathrm{tag})}$ is the number of measured (tagged) large-R jets in bin i,
- $N_{t\bar{t}\text{ non-matched},i}^{(\mathrm{tag})}$ is the number of (tagged) jets not matched to a hadronically de-

caying top quark according to the MC simulation in bin i,

- $N_{\text{non-}t\bar{t}}^{(\text{tag}),\text{i}}$ is the number of (tagged) large-R jets predicted by simulation from other background contributions, such as W+jets, Z+jets and single-top production in bin i,

- $N_{\text{MC},i}^{(\text{tag})}$ is the number of (tagged) large-R jets in matched $t\bar{t}$ events which are tagged by the HEPTopTagger in bin i.

This stage of the analysis is referred to as "pre-tag". The pre-tag distributions m_T^W, $E_{\text{T}}^{\text{miss}}$, large-$R$ jet mass and p_{T} of the p_{T}-leading C/A $R = 1.5$ jet with $p_{\text{T}} > 200$ GeV are shown Figs. 7.1a to 7.1d. After the application of the lepton plus jets requirements the simulation predicts a top quark purity of 97% (this includes contributions from the matched and non-matched $t\bar{t}$ as well as the single-top quark contribution). The $t\bar{t}$ contribution is divided into a matched (59%) and a not-matched (29%) part. The largest non-$t\bar{t}$ background contribution comes from W+jets production (3%), while other non-$t\bar{t}$ backgrounds (Z+jets, diboson production) are negligible. Single-top production contributes 9% of the total event yield. The green shaded band indicates the systematic uncertainty. To better visualize the contributions of the different kinds of systematics variations in the ratio, they have been redrawn separately: red for the experimental systematics and blue for the modeling systematics. All distributions are well described by the simulation.

The uncertainties which most affect the pre-tag distributions come from the b-tagging scale factors, the prediction of the $t\bar{t}$ cross section, the $t\bar{t}$ modeling uncertainties from the choice of generator, parton shower, and PDF sets. In particular, there is an increase of systematic uncertainty for higher values of large-R jet mass Fig. 7.1c and p_{T} Fig. 7.1d. The uncertainty from the choice of generator increases for high-masses that are particularly sensitive to additional radiation close to the hadronically decaying top quark. The modeling uncertainty for the large-R jet p_{T} distribution increases with p_{T} due to increasing uncertainties from the large-R JES, the b-tagging efficiency, and the $t\bar{t}$ modeling uncertainties.

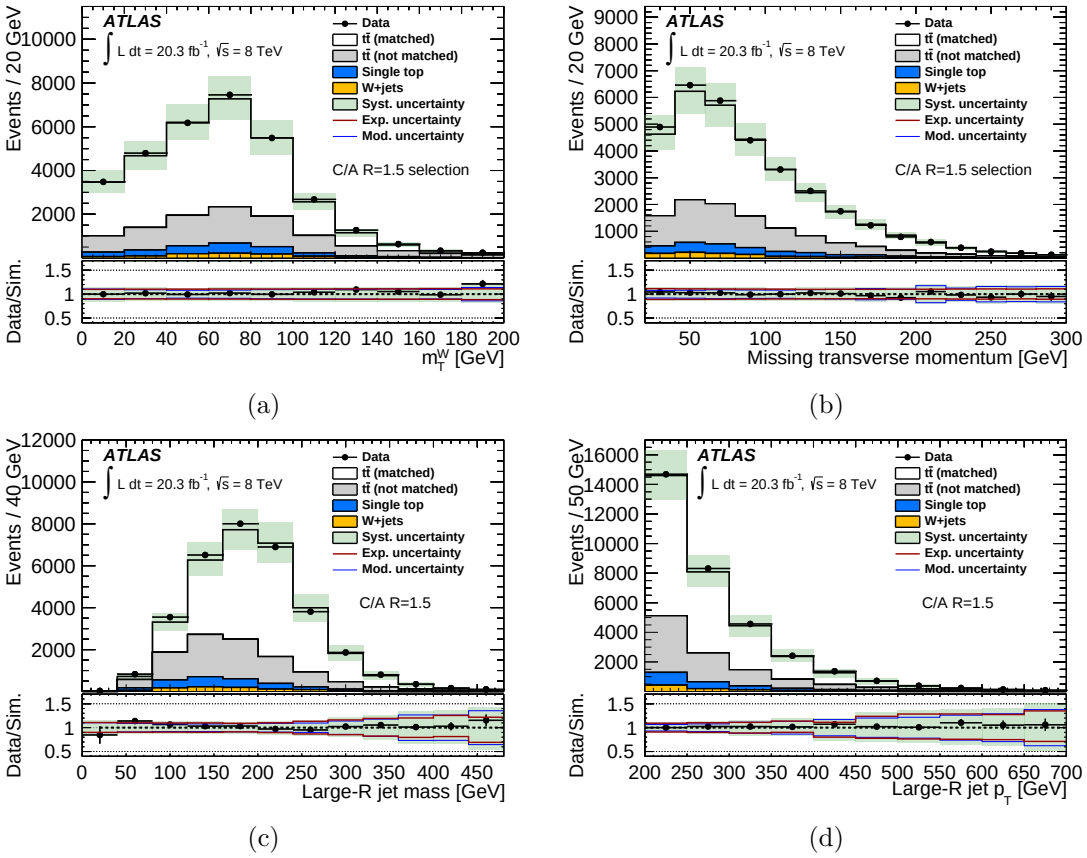

Figure 7.1: Distributions of the pre-tag selection variables. The (a) W-transverse mass, (b) the missing transverse momentum, (c) the leading large-R jet mass and (d) the large-R jet p_{T} are shown. The green shaded band indicates the systematic uncertainty. The impact of experimental and $t\bar{t}$ modeling uncertainties is shown separately in the ratio (red and blue lines respectively) [85].

The HEPToptagger algorithm is then applied to the large-R jets obtained after the lepton plus jets selection. The post-tag distributions for the top quark candidate m_{23}/m_{123}, $\arctan\left(\frac{m_{13}}{m_{12}}\right)$, p_{T} and mass are shown in Figs. 7.2a to 7.2d respectively. The top-tagging efficiency as defined in Eq. (7.1) and Eq. (7.2) is shown on Figs. 7.3a and 7.3b as a function of large-R jet p_{T} for two $|\eta|$ bins, $|\eta| < 0.7$ and $0.7 > |\eta| > 2.0$. The systematic uncertainty band shows the systematic uncertainty only in the MC while the systematic uncertainty band on the ratio shows the correlated data-MC uncertainty (the MC uncertainty enters the data through the non-matched $t\bar{t}$ subtraction). The HEP-

Toptagger efficiency plateaus at around $\sim 50\%$. The MC modeling of the data is very good in all p_{T} bins.

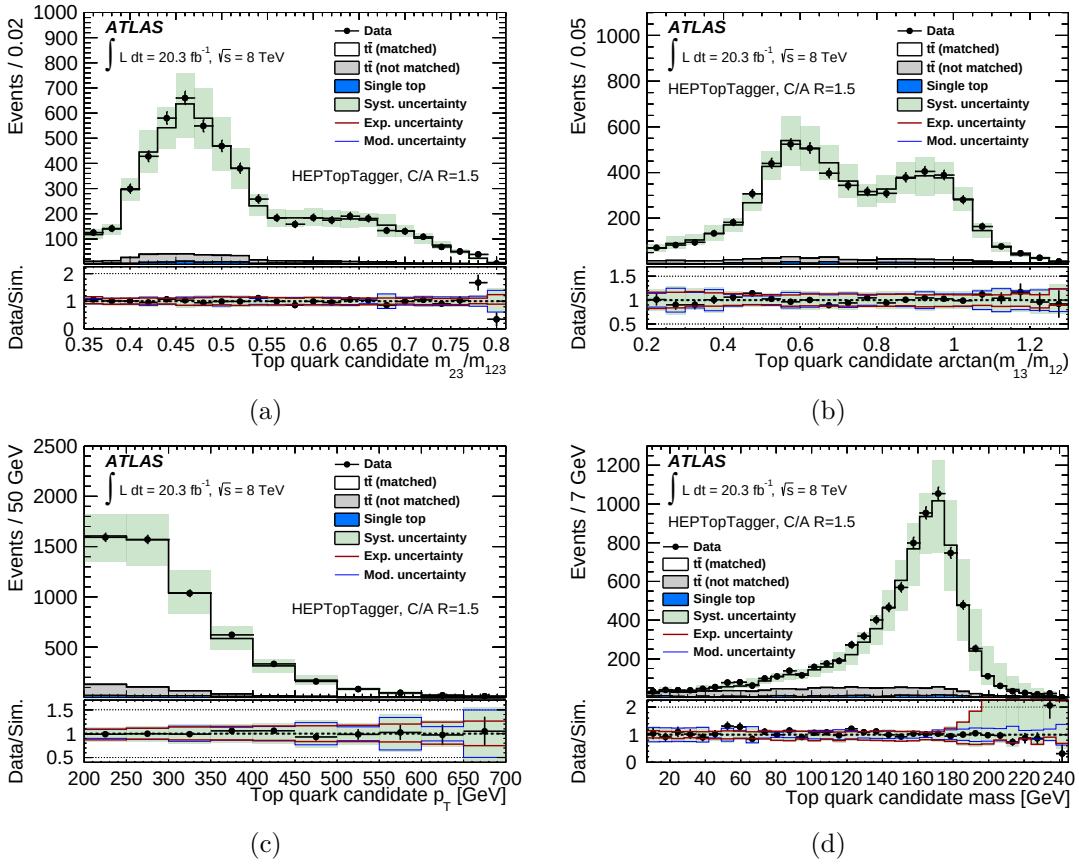

Figure 7.2: Distributions of HEPTopTagger substructure variables, (b)m_{23}/m_{123} , (b) arctan $\left(\frac{m_{13}}{m_{12}}\right)$, (c) mass and (d) p_{T} and of the top quark candidate for the tagged highest-p_{T} C/A R=1.5 jet in the event which are tagged by the HEPTopTagger. The green shaded band indicates the systematic uncertainty. The impact of experimental and $t\bar{t}$ modeling uncertainties are shown separately in the ratio (red and blue lines respectively) [85].

7.3 HEPTopTagger Mistag Rate

In addition to the top-tagging efficiency measurement, the mistag rate has been measured using the full 2012 dataset. This measurement is useful to understand if the available MC samples simulate the HEPToptagger mistag rate correctly. To perform this mea-

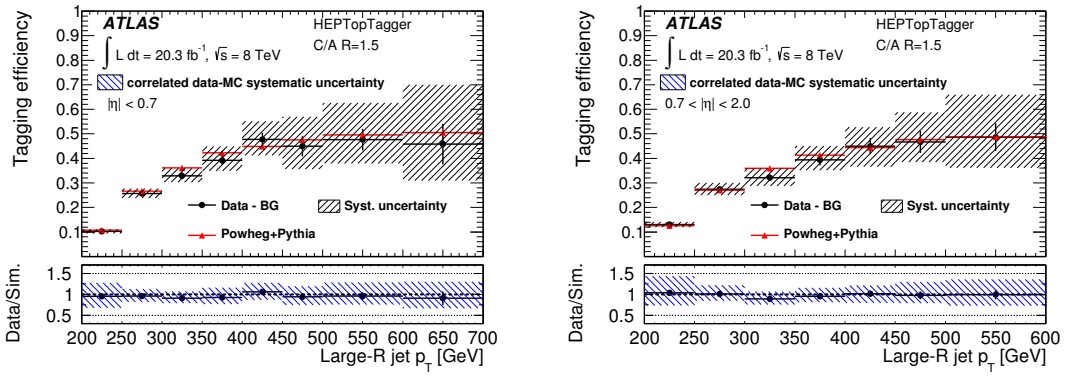

(a) (b)

Figure 7.3: The efficiency f_{data} and f_{MC} as defined in Eq. (7.1) and Eq. (7.2) respectively, for tagging C/A R=1.5 jets as a function of the large-R jet p_{T} in two η-ranges: (a) $|\eta| < 0.7$ and (b) $0.7 < |\eta| < 2.0$. The ratio $f_{\text{data}}/f_{\text{MC}}$ is shown at the bottom of each figure and the error bar gives the statistical uncertainty and the band the systematic uncertainty. The systematic uncertainty on the ratio is calculated taking into account the systematic uncertainties on the data and the MC and their correlation [85].

surement, it is necessary to obtain a sample free from top quarks. In the following a "mistag rate" selection, which attemps to select a sample of multijet events in data, free from top quarks is presented.

An electron trigger has been used to obtain an sample of multijet events. The use of jet triggers was and found not adequate for the purpose of these studies due to a high-p_{T} threshold and a the prescence of a trigger bias. Therefor events are selected by requiring the trigger for electrons with $p_{\text{T}} > 60$ GeV and vetoing the trigger for isolated electrons with $p_{\text{T}} > 24$ GeV. A first approach was to use the same electron trigger configuration as the top-tagging efficiency measurement i.e. trigger on electrons with $p_{\text{T}} > 60$ GeV or isolated electrons with $p_{\text{T}} > 24$ GeV. The C/A R=1.5 jet p_{T} after applying the HEPToptagger for this trigger configuration is shown in Fig. 7.4a. The remaining $t\bar{t}$ yield after this selection (also referred to as $t\bar{t}$ contamination) over the integrated large-R jet p_{T} is 12.4%. Changing the trigger configuration to require a trigger on electrons with $p_{\text{T}} > 60$ GeV and vetoing the trigger on isolated electrons with $p_{\text{T}} > 24$ GeV reduces the $t\bar{t}$ contamination to 3% shown in Fig. 7.4b. This reduction is expected since real electrons are more likely to be isolated. Events with an offline reconstructed

electron satisfying loose identification criteria [89], which are not isolated are discarded to reduce contributions from electroweak processes. To avoid the likely bias coming from the single core energy deposit likely to have fired the electron trigger, the leading large-R jet is required to have $\Delta R > 1.5$ from the electron-trigger object. If several large-R jets satisfy these criteria, only the jet with the highest-p_{T} is considered. The fraction of $t\bar{t}$ events before requiring a top candidate is negligible. The $t\bar{t}$ contribution in different large-R jet p_{T} bins is shown Table 7.1. After requiring a top candidate, the remaining $t\bar{t}$ contribution is subtracted. The selection criteria just described is called "mistag rate selection" onwards.

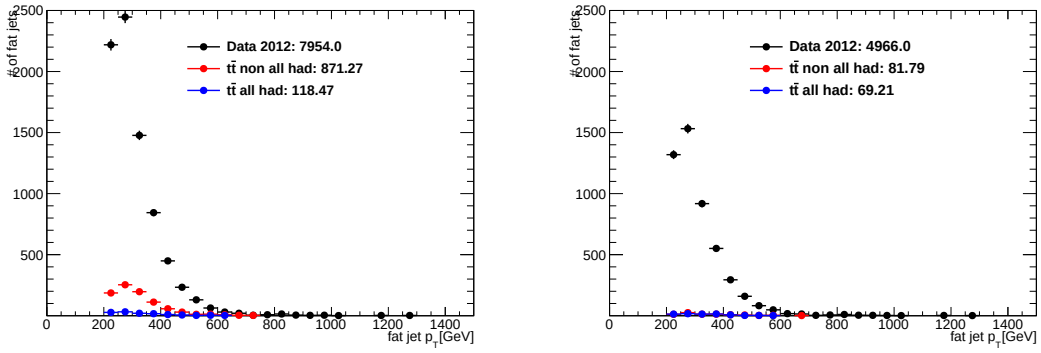

(a) (b)

Figure 7.4: (a) Large-R jet p_{T} selected by the HEPTopTagger with a top candidate mass between 140-200 GeV for the full 2012 dataset with the trigger configuration: electrons with $p_{\mathrm{T}} > 60$ GeV or isolated electrons with $p_{\mathrm{T}} > 24$ GeV. (b) large-R jet p_{T} selected by the HEPTopTagger with a top candidate mass between 140-200 GeV with the trigger configuration: electrons with $p_{\mathrm{T}} > 60$ GeV or isolated electrons with $p_{\mathrm{T}} > 24$ GeV isolated electrons with $p_{\mathrm{T}} > 24$ GeV.

The mistag rate is defined in each jet p_{T} bin i as:

$$f^{\mathrm{mistag}}_{\mathrm{data},i} = \left(\frac{N^{(\mathrm{tag})}_{\mathrm{data},i}}{N_{\mathrm{data},i}} \right) \qquad (7.3) \qquad f^{\mathrm{mistag}}_{\mathrm{MC},i} = \left(\frac{N^{(\mathrm{tag})}_{MC,i}}{N_{MC,i}} \right) \qquad (7.4)$$

where,

- $N^{(\mathrm{tag})}_{\mathrm{data}}$ is the number of measured (tagged) large-R jets in bin i,

Bin [GeV]	yield $t\bar{t}$/ yield data [%]
200 - 250	2.2
250 - 300	3.0
300 - 350	2.9
350 - 400	4.1
400 - 450	5.3
450 - 500	5.2
500 - 600	2.2
600 - 700	11.1

Table 7.1: $t\bar{t}$ contribution in data after the mistag rate selection.

- $N^{(\text{tag})}_{\text{non-}t\bar{t}}$ is the number of (tagged) large-R in bin i.

The pre-tag large-R jet p_{T} distribution, the post-tag large-R jet p_{T} distribution and the top candidate mass are shown in Figs. 7.5a to 7.5c respectively. The corresponding obtained mistag rate as defined in Eq. (7.3) and Eq. (7.4) for the full 2012 dataset and the di-jet samples from PYTHIA and HERWIG is shown in Fig. 7.5d. The mistag rate selection is applied to both data and MC and the MC is normalized to the data. The pre-tag large-R jet p_{T} distribution shows an agreement close to 1 for both PYTHIA and HERWIG. For post-tag distributions, particularly the the top candidate mass and the mistag rate, very large statistical uncertainties are observed for the MC. While the ratio is consistent with 1, the statistical uncertainty is too large to make a definite statement. Such a large statistical uncertainty is expected since there are very few instances where the electron trigger is fired for the di-jet MC samples.

Since the application of the trigger selection to the MC samples greatly reduces the number of available events, the removal of the trigger requirements for the simulation is studied in the following. The mistag rate selection is mainly designed to make sure the data is free from any top quark contribution, to reduce mistag-rate bias on the large-R jets and to achieve a lower large-R jet p_{T} threshold, it is not expected that the removal of the trigger selection biases the mistag rate for a dijet MC sample. After removing the mistag selection from the dijet MC, a slope appears in the large-R jet p_{T} due to the fact that requiring an electron trigger in the data effectively selects higher $\hat{m}$ events, where $\hat{m}$ is defined as the mass of the four-vector addition of the two original partons. The

slope does not affect the measurement of the mistag rate since it is a ratio. However to obtain an adequate MC modeling, the MC large-R jet p_{T} spectrum is reweighted to the data.

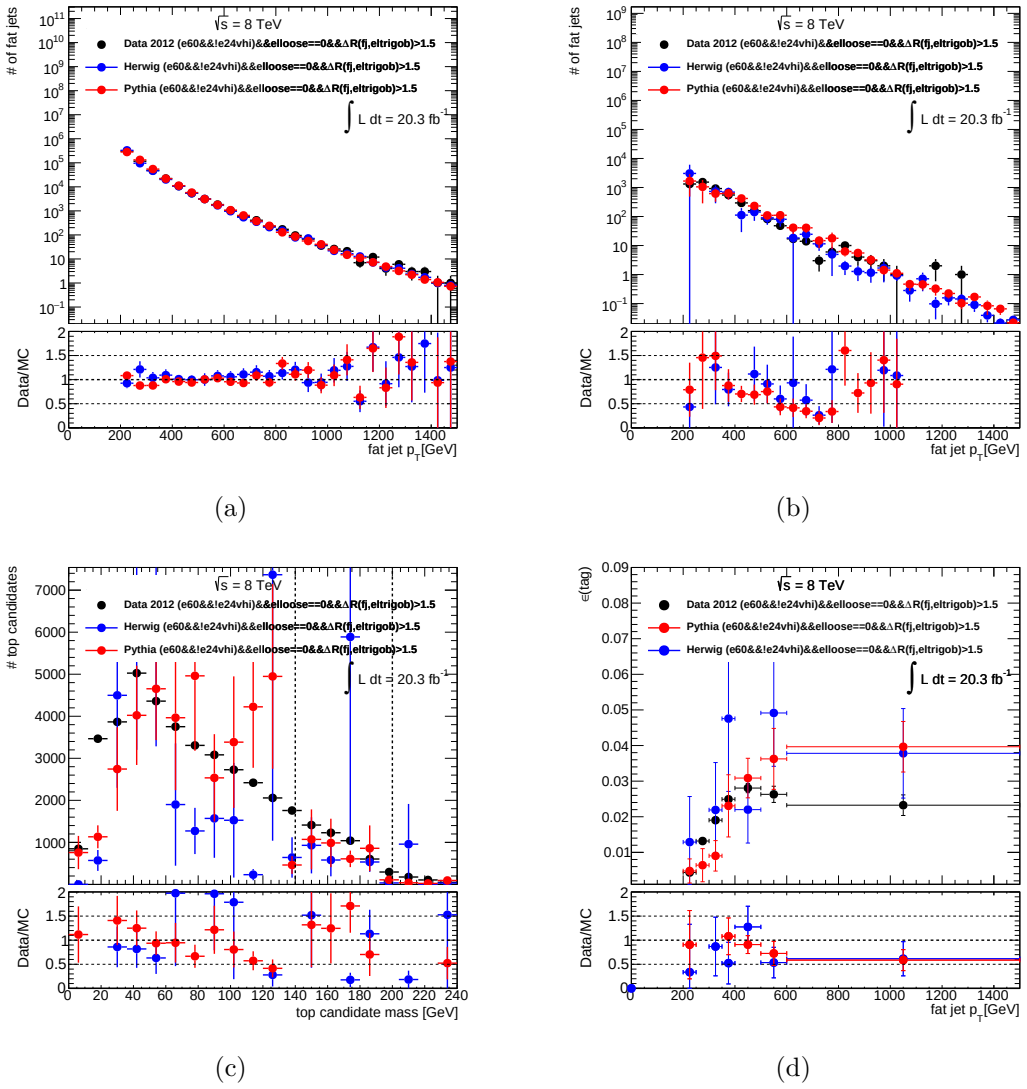

Figure 7.5: (a) Pre-tag C/A R=1.5 jet p_{T} distribution (b) post-tag C/A R=1.5 jet p_{T} distribution (c) top candidate mass and (d) mistag rate as a function of large-R jet p_{T} for the full 2012 dataset for the PYTHIA and HERWIG. Events in data and MC are required to have been triggered by the electron trigger, while vetoing a fully reconstructed loose electron and requiring $\Delta R(\text{large-}R\text{ jet}, \text{electron trigger object}) > 1.5$.

It is important to check that the application of the mistag rate selection criteria is

invariant against pile-up. Fig. 7.6a shows the average top candidate mass as a function of N_{PV} and Fig. 7.6b shows the average top candidate mass as a function of $\langle\mu\rangle$. Both plots are fitted with a line and the obtained parameters are printed. No significant deviation from a slope consistent with zero is observed for both data and the PYTHIA prediction.

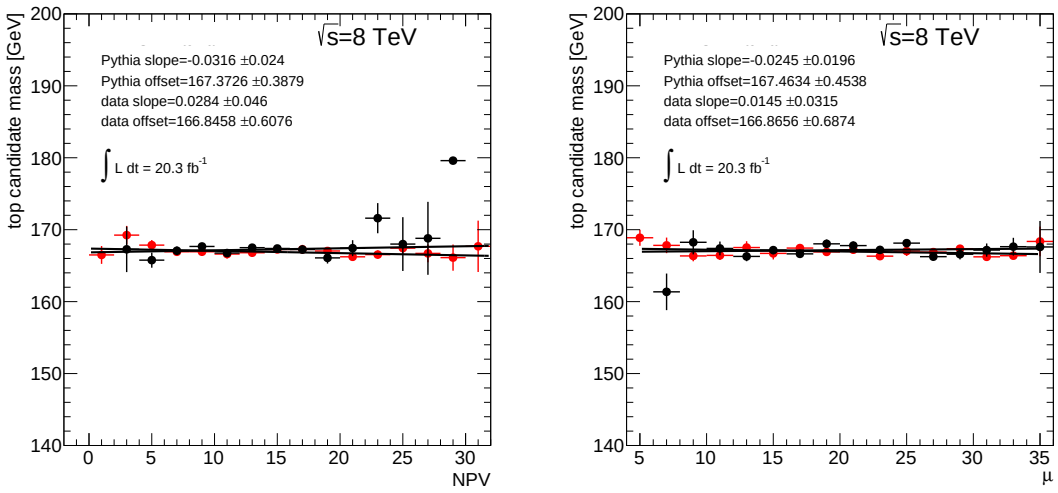

(a) (b)

Figure 7.6: (a) Average mass of the reconstructed HEPTopTagger top quark candidate as a function of N_{PV} (b) reconstructed primary vertices and () Average mass of the reconstructed HEPTopTagger top quark candidate as a function average number of interactions per bunch crossing, $\langle\mu\rangle$ in the PYTHIA di-jet sample and the 2012 dataset. The mass average is determined in the window $140 < m_{\mathrm{top}} < 200$ GeV. The slope is given in MeV (per unit of $\langle\mu\rangle$ or N_{PV}, respectively).

Only reconstruction systematic uncertainties are included for this measurement: the subjet JES, large-R JER, subjet JER and large-R JER. Table 7.2 shows the the relative uncertainty integrated over p_{T} and η. The biggest contribution comes from the subjet uncertainties. The control plots for the pre-tag, post-tag large-R jet p_{T} and the top candidate mass applying the mistag rate selection to data but not to the reweighted MC are shown in Figs. 7.7a to 7.7c. The red shaded band indicates the systematic uncertainty. The agreement in all distribution is very close to one within statistical uncertainties. Fig. 7.8 shows the corresponding mistag rate as a function of large-R jet

p_{T}, with the red shaded band indicating the systematic uncertainty. The mistag rate around 200 GeV is around 0.5% and rises to reach a plateau of 3.5% for a jet p_{T} of around 400 GeV. The MC prediction is good within statistical and systematic uncertainties.

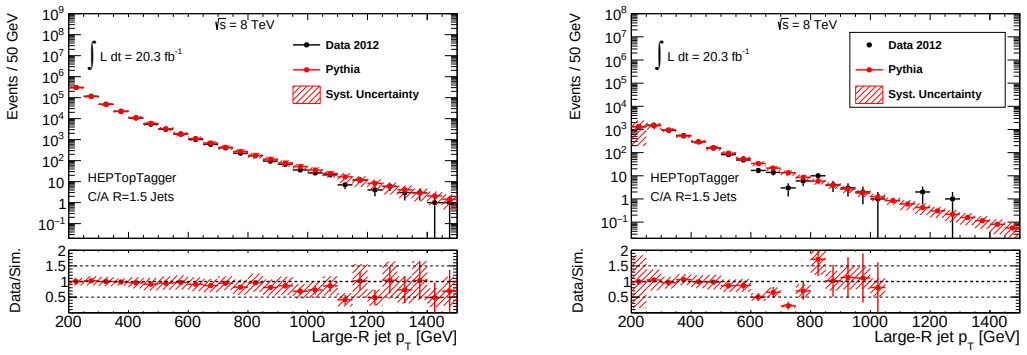

(a) (b)

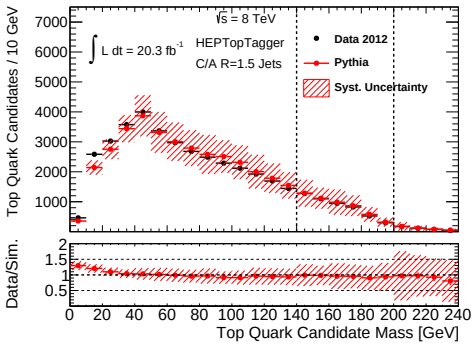

(c)

Figure 7.7: (a) Pre-tag C/A R=1.5 jet p_{T} distribution (b) post-tag C/A R=1.5 jet p_{T} distribution and (c) the top candidate mass (the dotted lines indicate the tagging mass range) for the full 2012 dataset, the PYTHIA prediction. The statistical uncertainties on the simulation are shown as a red shaded band. The ratio Data/Sim. is shown in each figure with the corresponding systematic uncertainty shown as a red shaded band. Events both in data and MC are required to fulfill the mistag rate selection.

7.4 MC-only Top Tagging Performance

A performance comparison of different top-tagging techniques is performed to understand the range of applicability, phase space, and best uses of commonly-used top-

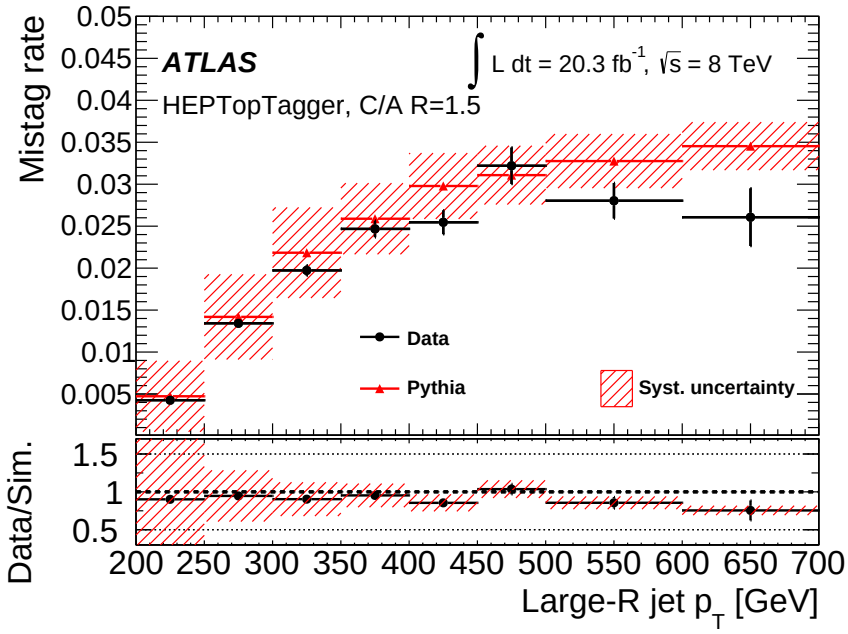

Figure 7.8: The HEPTopTagger mistag rate, as defined in Eqs. (7.3) and (7.4) for C/A R = 1.5 jets with $|\eta| < 2.0$ selected with the mistag rate selection as a function of the jet p_{T}. For the data the vertical error bars indicates the statistical uncertainty. For the PYTHIA prediction the vertical error bars indicates the statistical uncertainty while the shaded band show the systematic uncertainty. The ratio of measured to predicted mistag rate is shown at the bottom the figure and the error bar gives the statistical uncertainty of the measurement [85].

tagging techniques. In the following, the HEPTopTagger has been compared with other top-tagging approaches used in ATLAS. For the following comparisons are MC only. This allows to extend the kinematic reach for which 8 TeV data was collected. The performance is studied in terms of the efficiency for tagging signal large-R jets and the background rejection, which is defined as the reciprocal of the mistag rate. For signal and background, $Z' \to t\bar{t}$ events and multijet events are used. In the fully hadronic $t\bar{t}$ channel, multijet events are the largest background. Other backgrounds such as W+jets production do not play an important role due to their smaller cross section. In the lepton plus jets channel, W+jets production is the largest background when the W boson decays leptonically and there are additional jets in the event. It has been shown, that the mistag rate from multijet and W+jets production is the same [77]. Therefore, the

systematic	PYTHIA[%]
large-R energy scale	8.06
large-R energy resolution	10.459
subjet energy scale	29.667
subjet energy resolution	29.319

Table 7.2: Impact of systematic uncertainties on the p_{T} and η-integrated fraction of tagged fat jets in simulation. The numbers give the relative shift of the tagging fraction and correspond to the maximum shift when applying "up" and "down" variations with respect to the nominal prediction.

	200-250 GeV	250-300 GeV	300-350 GeV	350-400 GeV	400-450 GeV	450-500 GeV	500-600 GeV	600-700 GeV
MC efficiency	0.0047	0.0142	0.0218	0.0259	0.0298	0.0311	0.0328	0.0345
Data efficiency	0.0042	0.0136	0.0192	0.0243	0.0259	0.0298	0.0253	0.0211
Ratio Data/MC	0.9009	0.9584	0.8808	0.9392	0.868	0.958	0.773	0.6104
Syst. Error (MC)	0.0042	0.0051	0.0054	0.0042	0.0039	0.0035	0.0032	0.0029
Syst. Error (MC)/ MC Eff.	0.9012	0.3586	0.2476	0.1638	0.1317	0.1128	0.0985	0.0828
Absolute error in ratio	0.8118	0.3437	0.2181	0.1539	0.1143	0.1081	0.0761	0.0506
Relative error in ratio	0.9012	0.3586	0.2476	0.1638	0.1317	0.1128	0.0985	0.0828

Table 7.3: Data and MC mistag rate efficiencies with their corresponding systematic uncertainty in different large-R jet p_{T} bins.

conclusions reached in this section are applicable to the $t\bar{t}$ lepton plus jets channel where W+jets production is the main non-$t\bar{t}$ background.

One of the first obstacles one encounters when trying to compare different top-tagging approaches is the fact that different approaches use different large-R jet collections as input, namely anti-k_t R=1.0 and C/A R=1.5. Therefore, a side-by-side comparison is not ideal since different phase-spaces would be used. To relate the different jet types used at reconstruction level the particle-level or "truth" jets are used. Reconstructed large-R jets are geometrically matched to a particle-level jet within $\Delta R = 0.75$ for the trimmed anti-k_t $R = 1.0$ jets, and within $\Delta R = 1.0$ for the C/A $R = 1.5$ jets. The fraction of reconstructed large-R jets with no truth matching jet is negligible. In addition, truth jets in the signal are matched to a hadronically decaying top quark within $\Delta R = 0.75$. The top-quark direction at the top-quark decay vertex is chosen consistent with the matching procedure used for the top tagging efficiency measurement. The signal truth jet p_{T} spectrum is reweighted to the p_{T} spectrum of the background to remove any dependence on a specific signal model.

Different top-tagging approaches can be classified in two categories: "low efficiency-high rejection", with a top-tagging efficiency of $\sim$ 30-50% and a rejection of $\sim$10-1000 and "high efficiency-low rejection", with a top-tagging efficiency of $\sim$ 50-100% and a rejection of $\sim$1-10. The HEPToptagger is a "low efficiency-high rejection" top-tagger. "Low efficiency-high rejection" top-taggers include the HEPTopTagger, Shower Deconstruction and the W'-tagger (see Section 6.3), while "high efficiency-low rejection" include the substructure variables such as the mass, the splitting scales, N-subjetiness or a combinations of these (indicated as taggers I-V in figures Figs. 7.9a, 7.9b, 7.10a and 7.10b) (see Section 6.3). As "low efficiency-high rejection", the HEPTopTagger is better suited for application in events with large multijet background as opposed to clean environments such as the $t\bar{t}$ lepton plus jets decay channel, where requiring a lepton already eliminates a large a amount of multijet background. In this context it is better to choose a high efficiency top-tagger. The comparisons of the different top taggers is performed in the following $p_{\mathrm{T}}^{\mathrm{true}}$ bins: $350 < p_{\mathrm{T}}^{\mathrm{true}} < 400$ GeV, $550 < p_{\mathrm{T}}^{\mathrm{true}} < 600$ GeV, $700 < p_{\mathrm{T}}^{\mathrm{true}} < 1000$ GeV and $1000 < p_{\mathrm{T}}^{\mathrm{true}} < 1500$ GeV, shown in Figs. 7.9a, 7.9b, 7.10a and 7.10b, respectively. For the range $350 < p_{\mathrm{T}}^{\mathrm{true}} < 400$ GeV the HEPToptagger performance is represented by the black dot. The HEPTopTagger remains competitive in all $p_{\mathrm{T}}^{\mathrm{true}}$ bins when comparing to other "low efficiency-high rejection" top taggers. From the top-taggers explored for this publication the HEPToptagger is the only available approach capable of tagging down to a top quark p_{T} of 200 GeV due to its larger R=1.5 distance parameter.

7.5 Conclusion

The HEPToptagger performance was measured in exhaustive detail. For the top-tagging efficiency, the lepton plus jets channel has been used since it provides an environment with a high purity of $t\bar{t}$ events. The data/MC comparisons show a very good agreement for both the pre-tag, post-tag distributions and the top-tagging efficiency. All relevant systematic uncertainties have been included and a very good understanding has been achieved about the source of the experimental and modeling systematics.

For the mistag rate measurement the use of an electron trigger allows to measure the mistag rate down to a large-R p_{T} of 200 GeV. It is worth pointing out than this is the only measurement of this kind since the CMS experiment only measures down to 400 GeV with the sum of the tranverse energy of all objects in the event, $\mathrm{H_T} > 800$ GeV [90]. It is also observed that the MC simulation correctly models the data for the HEPTopTagger mistag rate. The strategy of using an electron trigger has been used by all other existing top-tagging approaches in ATLAS in order to get a multijet sample with no trigger bias.

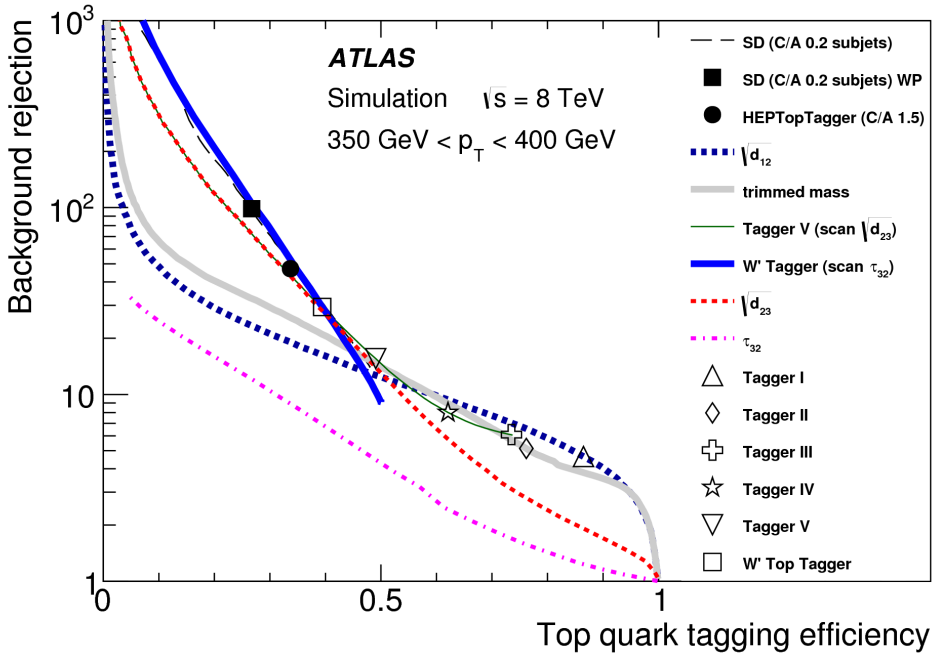

(a)

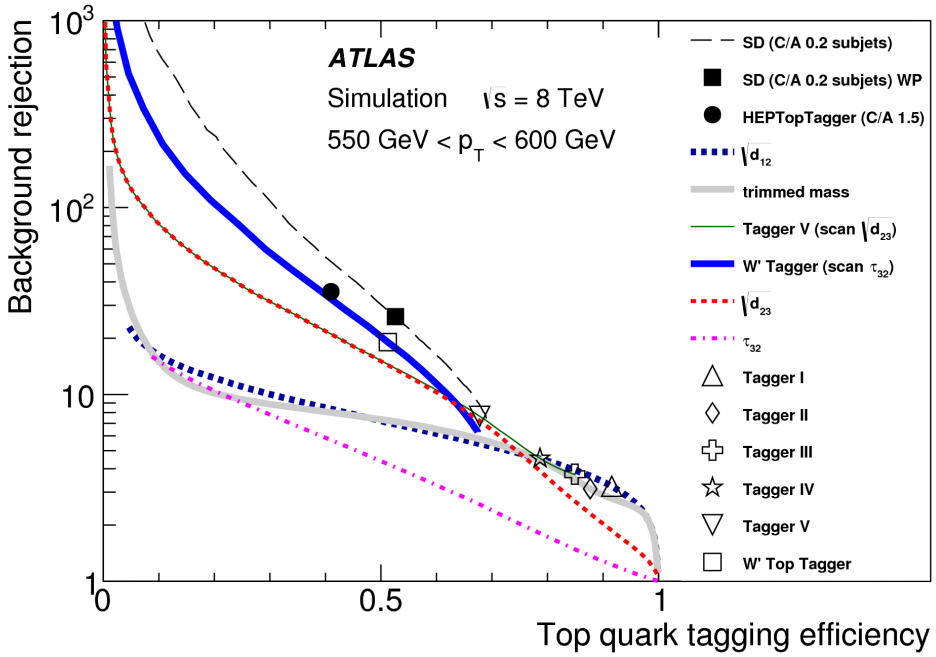

(b)

Figure 7.9: The background rejection as a function of the tagging efficiency of large-R jets obtained from MC simulations for p_{T} bins (a) 350 GeV $< p_{\mathrm{T}} <$ 400 GeV and (b) 550 GeV $< p_{\mathrm{T}} <$ 600 GeV. The HEPToptagger is shown as black full dot [85].

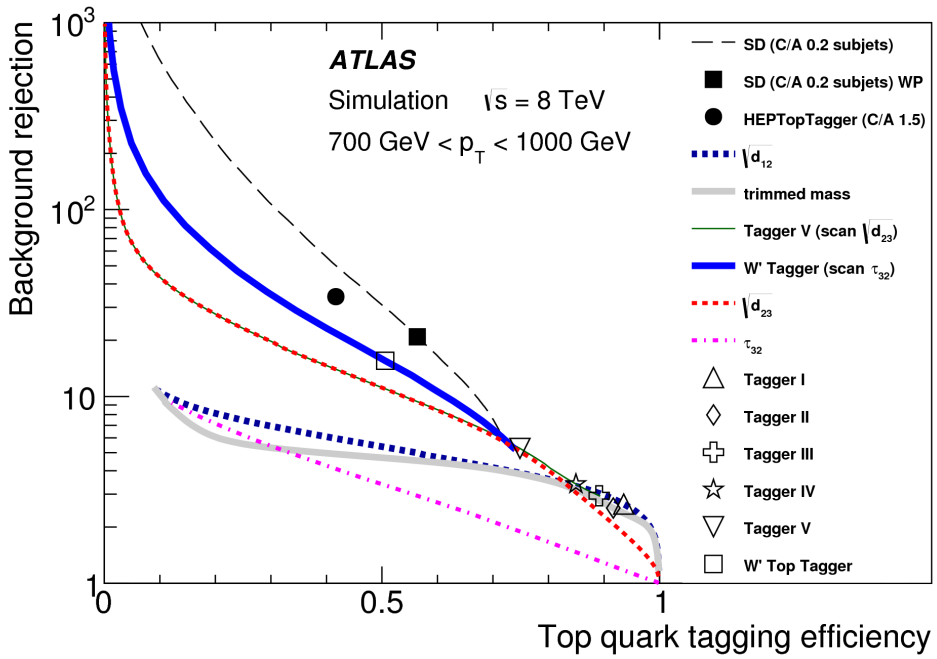

(a)

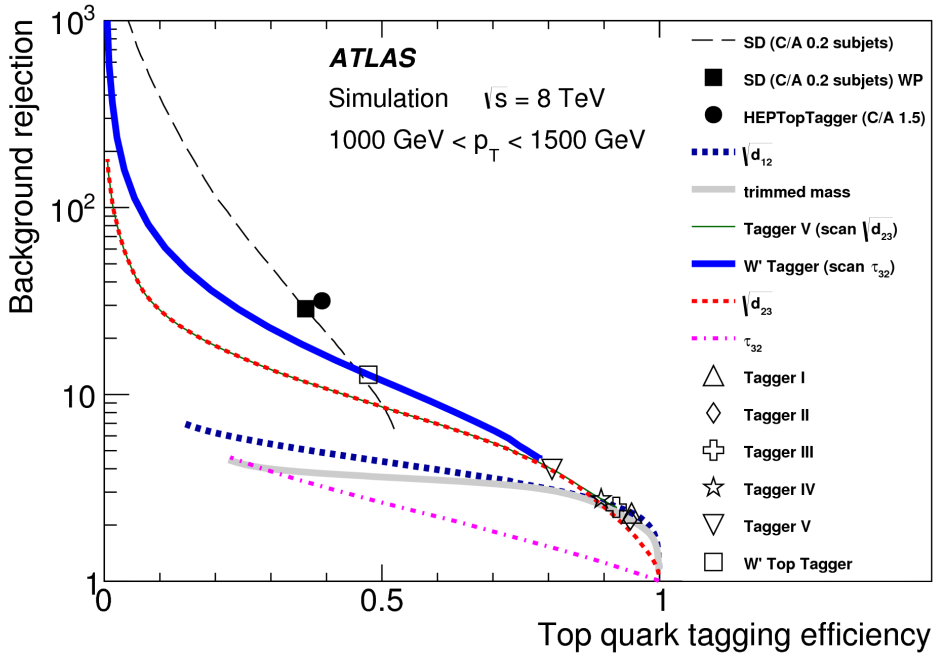

(b)

Figure 7.10: The background rejection as a function of the tagging efficiency of large-R jets obtained from MC simulations for p_{T} bins (a) 700 GeV $< p_{\mathrm{T}} <$ 1000 GeV and (b) 1000 GeV $< p_{\mathrm{T}} <$ 1500 GeV. The HEPToptagger is shown as black full dot [85].

8 Fully Hadronic $t\bar{t}$ Resonance Search

8.1 Introduction

A search for new heavy resonances in the $t\bar{t}$ invariant mass spectrum in the fully hadronic channel is presented. The top-color assisted technicolor Z' boson resonance, described in Section 2.7.1, decaying only into top quark pairs is considered for this study. The Z' boson resonance is examined with two decay widths: $\Gamma/m = 1.2\%$ and $\Gamma/m = 3.0\%$.

The most recent $t\bar{t}$ resonance search conducted by the ATLAS collaboration [91] was carried out in the lepton plus jets channel using only events where a large-R jet with $p_{\mathrm{T}} > 350$ GeV is found and Z' boson resonances in the mass ranges $0.7 > m_{Z'} > 2.0$ TeV have been excluded at a 95% confidence level (CL). For the fully hadronic channel, a search was conducted in the fully hadronic channel using the full 7 TeV dataset [92], excluding Z' boson resonances in the mass range $0.70 < m_{Z'} < 1.00$ and $1.28 < m_{Z'} < 1.32$ TeV. The CMS collaboration has presented results combining the dilepton, lepton plus jets and the fully hadronic channels for the 8 TeV data-taking period reaching an upper mass limit of 2.4 TeV for a Z' boson resonance of width $\Gamma/m = 1.2\%$ [93].

In this thesis, the HEPTopTagger algorithm (see Section 6) is used to search for $t\bar{t}$ resonances in the fully hadronic decay channel using the 13 TeV dataset. The HEP-TopTagger tests C/A R=1.5 jets for compatibility with the top quark decay hypothesis. This analysis focuses on the boosted regime where the top quarks are expected to have $p_{\mathrm{T}} > 200$ GeV. If a top quark is found, the C/A R=1.5 jet is said to be "tagged" and the top quark candidate four-momentum is returned. The $m_{t\bar{t}}$ variable is constructed using the top quark four-vectors. Additionally, as motivated in Section 6.2.2, it is beneficial to reconstruct the $m_{t\bar{t}}$ variable with the tagged filtered C/A R=1.5 jets. The filtering procedure consists on reclustering the constituents of the "parent" C/A R=1.5 using the C/A algorithm with $R_{filt} = 0.3$ and requiring exclusively $N_{filt} = 5$ subjets[6]. The $N_{filt} = 5$ subjets are calibrated using the scheme explained in Section 5.4 and added to

[6]The filtering settings were chosen as given in [79]. Other settings were investigated but did not provide any substantial advantage.

get the filtered C/A R=1.5 four-momentum. It is shown in Section 8.2.2 that by using the tagged filtered C/A R=1.5 jets instead of the top quark four-vector, improves the $m_{t\bar{t}}$ resolution significantly.

Improvements to the resonance search by using track jets for b-tagging and filtered C/A R=1.5 jets for $m_{t\bar{t}}$ reconstruction are discussed in Section 8.2.1 and Section 8.2.2, respectively. The event selection and reconstruction is presented in Section 8.3. After applying all the selection criteria ("full selection"), the most important backgrounds are comprised by fully hadronic $t\bar{t}$ and QCD multijet events. A very small amount of non-fully hadronic (semileptonic and full leptonic decay modes) $t\bar{t}$ is still present as well. The method to estimate the multijet background from data is explained in Section 8.4. Data/MC comparisons which show that the multijet background estimation method works well are shown in Section 8.5. The systematic uncertainties taken into account are discussed in Section 8.6. Finally, a discussion of the results obtained through statistical analysis is given in Section 8.7. In the following, C/A R=1.5 jets are referred to as large-R jets.

8.2 Improvements

8.2.1 b-tagging with Track Jets

In the previous $t\bar{t}$ hadronic resonance search, b-tagging with calorimeter jets was used. For the present analysis, b-tagging with track jets is used. The motivation for this change is detailed in section Section 5.5.1. The improvement between track and calorimeter b-tagging in the $t\bar{t}$ fully hadronic resonance search is thus investigated. The 70% efficiency working point is selected for both types of b-tagging. To understand the impact of the change of b-tagging approaches with respect to the truth $m_{t\bar{t}}$ spectrum without taking into account the top tagging efficiency, only the efficiency of finding exactly 2 b-jets in the event is shown in Fig. 8.1a between the track jets and the calorimeter jets. The efficiency of finding exactly 2 b-jets using track jets is approximately 40% higher throughout the $m_{t\bar{t}}$ spectrum. This is in accordance with the studies presented in Section 5.5.1 showing

that b-tagging with track jets outperforms b-tagging with calorimeter jets considerably at higher $m_{t\bar{t}}$. The efficiency of the full selection using b-tagging with track and calorimeter jets is shown in Fig. 8.1b. b-tagging using track jets has improves by a factor 1.3 to 2 (depending on truth $m_{t\bar{t}}$) the selection efficiency. One can also look at the integrated selection efficiency on signal and background for 2 b-jets and the full selection (2 b-tags,2 top quarks) as shown in Tables 8.1 and 8.2. For the signal the efficiency is increased by approximately a factor of 2 when going from calorimeter jets to track jets. For the background, the selection efficiency is also increased by approximately a factor of 2. This is results in an increase of $S\sqrt{B}$ by a factor of $\sqrt{2}$ or 1.41. The gains of using track jets come about for two reasons reasons. First, since tracker is more robust against pile-up, it is possible to have lower jet p_{T} thresholds. For calorimeter jets the p_{T} threshold is usually set at 25 GeV, whereas for track jets it is lowered to 10 GeV (hence the increase in background). Second, the smaller size of the track jet allows for better jet separation in boosted environments such as the one in this analysis. For the rest of the chapter b-tagging refers to b-tagging using track jets.

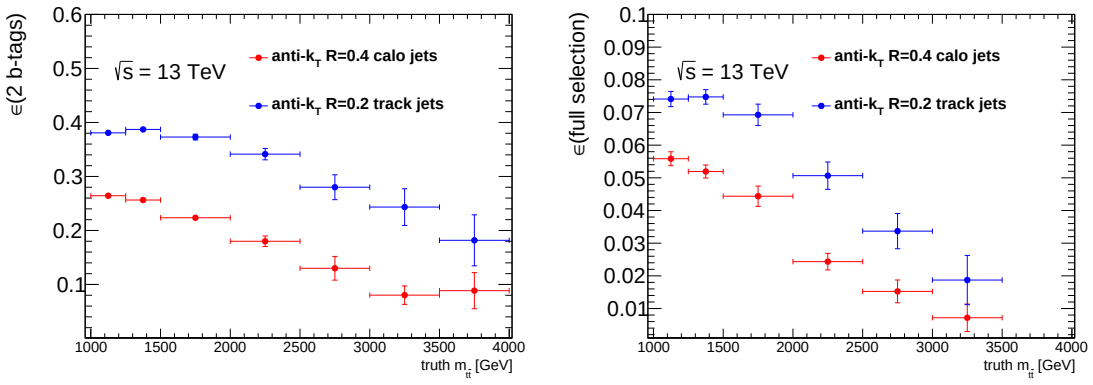

(a) (b)

Figure 8.1: (a) Efficiency of finding exactly 2 b-jets in a $t\bar{t}$ sample as a function of the truth $m_{t\bar{t}}$ for anti-k_t $R = 0.2$ track jets and anti-k_t $R = 0.4$ calorimeter jets. (b) Efficiency of full selection in a $t\bar{t}$ sample as a function of the truth $m_{t\bar{t}}$ using anti-k_t $R = 0.2$ track jets and anti-k_t $R = 0.4$ calorimeter jets.

Sample	2 b-tags	Full Selection
Z'(2 TeV) 13 TeV calo b-tag	25.53	2.71
Z'(2 TeV) 13 TeV track b-tag	44.00	5.14

Table 8.1: Selection efficiency [%] for track and calorimeter jets on a Z'(2 TeV) sample for 2 b-tags and the full selection (2 b-tags,2 top tags).

Sample	2 b-tags	Full Selection
QCD 13 TeV calo b-tag	1.67	0.0052
QCD 13 TeV track b-tag	3.39	0.012

Table 8.2: Selection efficiency [%] for track and calorimeter jets on a QCD sample for 2 b-tags and the full selection (2 b-tags,2 top tags)

8.2.2 $m_{t\bar{t}}$ Reconstruction with Filtered C/A R=1.5 jets

For a very heavy resonance which decays into off-shell top quarks, there is an increase in gluon radiation from off-shell top quarks which go back to on-shell top quarks. This missed final-state radiation causes a mis-reconstruction of the heavy resonance when using the HEPTopTagger. Therefore the approach mentioned in Section 6.2.2 where the $m_{t\bar{t}}$ variable is reconstructed from the tagged filtered C/A R=1.5 jets (as opposed to the top quark candidate) is investigated. The reconstructed $m_{t\bar{t}}$ spectra using Z' boson resonance masses of 1.5 and 3.0 TeV are shown in Figs. 8.2a and 8.2c. The resolution of the $m_{t\bar{t}}$ variable using filtered C/A R=1.5 jets and top quarks candidates is shown in Figs. 8.2b and 8.2d respectively. The improvement on the $m_{t\bar{t}}$ reconstruction using the filtered jets is readily seen by observing that for a Z'(1.5 TeV) resonance using the filtered large-R jet four-vectors returns a sharper peak around $m_{t\bar{t}} \sim 1.5$ TeV. The mis-reconstruction when using the four-vectors returned by the HEPTopTagger is significantly larger higher Z' boson mass of 3 TeV. Using the filtered C/A R=1.5 jet four-vectors, the resolution improves and remains similar to the Z'(1.5 TeV) resolution. For a $t\bar{t}$ resonance search, a worse $m_{t\bar{t}}$ reconstruction translates into decreased sensitivity. Using the approach of the filtered jets, it is possible to re-align the Z' boson mass and thereby improve the sensitivity.

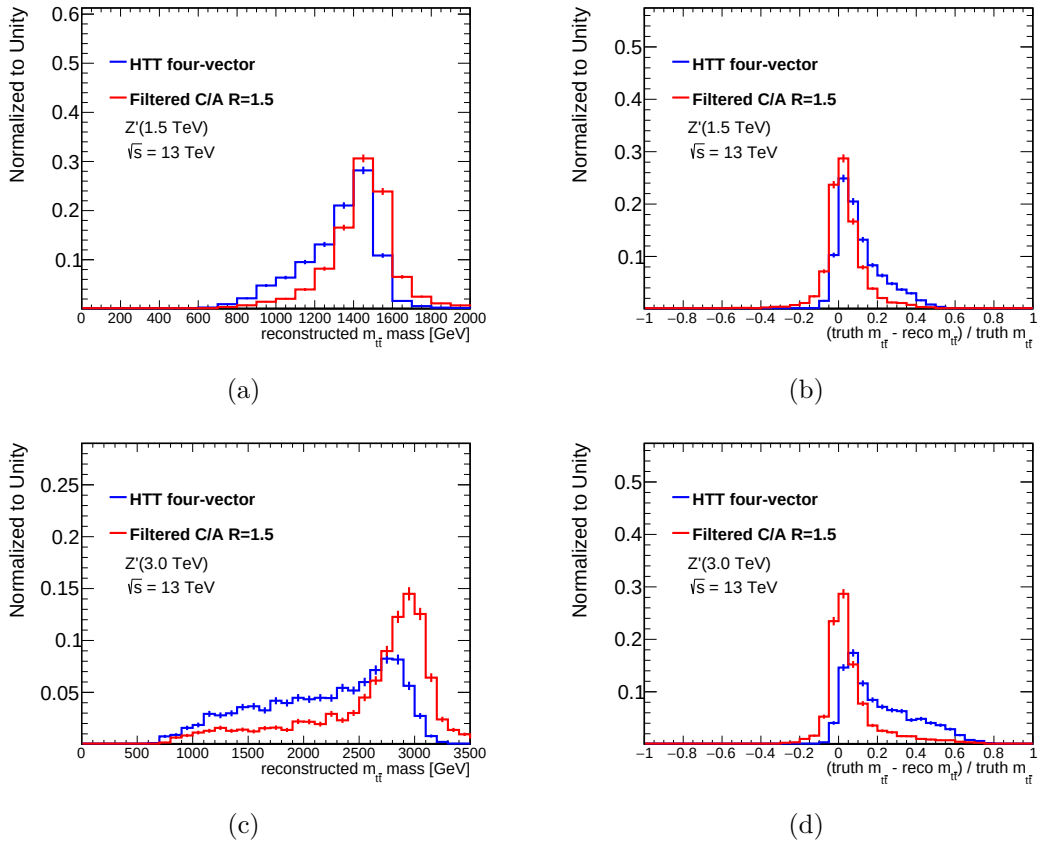

Figure 8.2: Comparison of the reconstructed $m_{t\bar{t}}$ spectra after the full selection for the HEPTopTagger using top quark candidate four-vectors and the filtered C/A R=1/5 jet four-vectors for a Z' boson resonance with masses of (a) 1.5 and (c) 3 TeV. Resolution of the $m_{t\bar{t}}$ for HEPTopTagger four-vector and tagged filtered C/A R=1/5 jets for Z' boson resonances with masses (b) 1.5 and (d) 3 TeV.

8.3 Event Selection

For this thesis, the full 2015 dataset and data corresponding to an integrated luminosity of 11.5 fb^{-1} from the 2016 dataset collected by the ATLAS detector are used. For the 2015 data-taking period, the lowest unprescaled anti-k_t R=1.0 jet trigger with a threshold of $p_{\mathrm{T}} > 360$ GeV is used. Due to increased luminosity in the 2016 data-taking period, the anti-k_t R=1.0 jet trigger threshold was raised to $p_{\mathrm{T}} > 420$ GeV. The choice of jet trigger restricts this search to the mass range $m_{t\bar{t}} > 1000$ GeV. The previous fully hadronic $t\bar{t}$ search with the HEPTopTagger has already excluded Z' boson resonances with masses less than 1 TeV [92].

The primary vertex must have at least five associated tracks with $p_{\mathrm{T}} > 0.4$ GeV. If more than one primary vertex is found, the vertex with the highest-p_{T} associated tracks is selected. This requirement suppresses background from sources other than the pp collision. If isolated leptons with the corresponding quality criteria and $p_{\mathrm{T}} > 25$ GeV are found, the event is rejected. This ensures orthogonality to the $t\bar{t}$ resonance search in the lepton plus jets channel.

At least two C/A R=1.5 jets are required. The C/A R=1.5 jets are calibrated using the scheme described in Section 5.4. For the 2015 dataset, the leading jet must have $p_{\mathrm{T}} > 400$ GeV. For the 2016 dataset, the leading jet must have $p_{\mathrm{T}} > 500$ GeV. The subleading jet must have $p_{\mathrm{T}} > 200$ GeV for both datasets. The lower p_{T} requirement on the subleading jet allows for an increased efficiency since it is not guaranteed that both top quarks will have the same momentum. The HEPTopTagger then takes the large-R jets as inputs. Exactly two top quarks candidates are required with masses between 140 and 210 GeV. The $m_{t\bar{t}}$ variable is obtained by adding the tagged filtered C/A R=1.5 jet four-vectors .

Exactly two jets originating from a b-quark are required. This greatly reduces the background coming from multijet production. Section 5.5.1 describes the increase in b-tagging efficiency for track jets over calorimeter jets. A study of this improvement in the context of this thesis is presented in Section 8.2.1. Track jets are clustered with the

anti-k_t algorithm with R=0.2 and are required to have $p_{\mathrm{T}} > 10$ GeV, $|\eta| < 2.5$ and more than one track. Calorimeter jets are clustered with the anti-k_t algorithm with R=0.4 and are required have $p_{\mathrm{T}} > 25$ GeV and $|\eta| < 2.5$. The MV2c10 b-tagging algorithm (defined in Section 5.5.1) with 70% efficiency is used for both jet collections. To ensure that the b-jets found originate from the hadronic top decay, a distance $\Delta R < 1.5$ between the b-jet and the large-R jets is required. Events containing anti-k_t R=0.4 jets arising due to instrumental detector failures, non-collision backgrounds such as cosmic rays, beam gas and beam halo are rejected [58]. The yields before any b- or top-tagging are shown for the full 2015 dataset and 11.5 fb^{-1} of the 2016 dataset are shown in Tables 8.3 and 8.4, respectively as a function combination of number of b-tags and top-tags.

	before top-tagging	1 top-tag	2 top-tags
before b-tagging	12.7 $\times 10^6$	4.2×10^5	5.8×10^3
1 b-tag	2.0 $\times 10^6$	1.2×10^5	2.5×10^3
b-tags	1.6×10^5	1.4×10^4	9.5×10^2

Table 8.3: Total number of events recorded in data for different number of b-tags and top-tags for the full 2015 dataset (3.2 fb^{-1}). The events are required to pass all other event selection criteria listed in the main text.

	before top-tagging	1 top-tag	2 top-tags
before b-tagging	2.2×10^6	8.8×10^5	1.4×10^6
b-tag	4.0×10^6	2.8×10^5	7.0×10^3
b-tag	3.5×10^5	3.3×10^4	2.3×10^3

Table 8.4: Total number of events recorded in data for different number of b-tags and top-tags for 11.5 fb^{-1} of the 2016 dataset. The events are required to pass all other event selection criteria listed in the main text.

After the full selection, it is important to check if the relevant variables in the analysis are independent on pile-up. Pile-up dependence may induce artificial features not related to any underlying physics to emerge. The average reconstructed top quark candidate mass as a function of the average number of interaction per bunch-crossing, $\langle\mu\rangle$, and the number of reconstructed primary vertices, N_{PV}, for the MC fully hadronic $t\bar{t}$ and the data collected during 2016 after the full selection are shown in Fig. 8.3a and Fig. 8.3b

respectively. For $\langle\mu\rangle$, the offset of the MC $t\bar{t}$ and data are consistent with each other, while the slope is consistent with zero for both data and MC $t\bar{t}$. For N_{PV}, the offset of the MC $t\bar{t}$ and data 2016 are also consistent with each other, while the slope is consistent with zero for data but not for $t\bar{t}$ MC. It is expected that the systematic uncertainty on the $t\bar{t}$ covers this small inconsistency. Shown in Fig. 8.4a and Fig. 8.4b are the average reconstructed $m_{t\bar{t}}$ mass using the filtered large-R jets as a function of $\langle\mu\rangle$ and N_{PV} for $t\bar{t}$ and the data collected during 2016 respectively. The offset of the $t\bar{t}$ MC and data 2016 are consistent with each other, while the slope is consistent with zero for both data and $t\bar{t}$ both as a function of $\langle\mu\rangle$ and N_{PV}. Pile-up independence for the $m_{t\bar{t}}$ variable is crucial since this is the variable used in the limit-setting procedure.

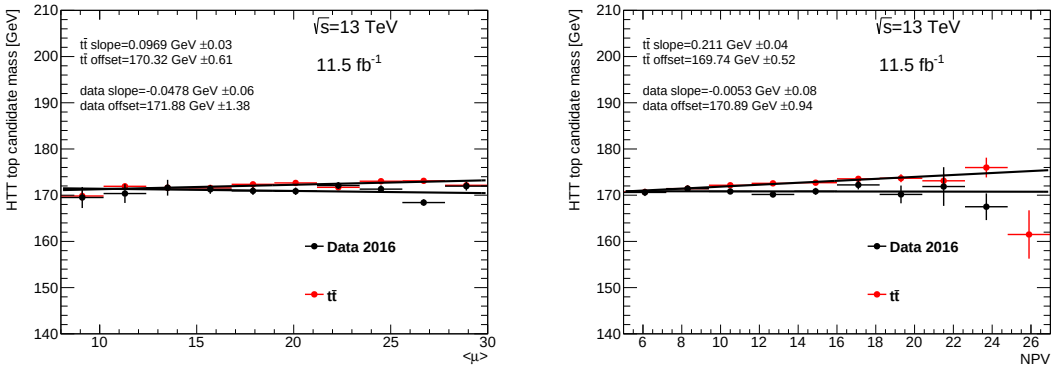

(a) (b)

Figure 8.3: The mean HEPTopTagger top-quark candidate mass as a function of (a) average number of interactions per bunch-crossing $\langle\mu\rangle$ and (b) the number of primary vertices N_{PV}. The quantities are shown for data and events from MC $t\bar{t}$ after the full selection. Only statistical uncertainties are shown.

8.4 Multijet Estimate

The multijet event yield present in the signal region is determined via a data-driven method. Six regions are defined depending on the number of b-tags and top-tags. Table 8.5 also shows the $t\bar{t}$ content or purity in each of the regions.

The signal region has a $t\bar{t}$ purity of 88%, whereas the multijet background dominates in the other regions. The most significant contribution of the signal is expected in the

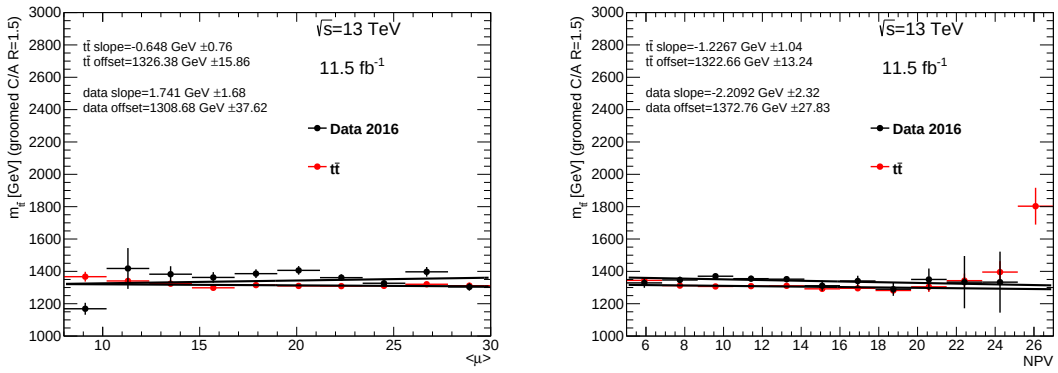

(a) (b)

Figure 8.4: The mean filtered C/A R=1.5 jet mass as a function of (a) average number of interactions per bunch-crossing $\langle\mu\rangle$ and (b) the number of primary vertices N_{PV}. The quantities are shown for data and events from MC $t\bar{t}$ after the full selection. Only statistical uncertainties are shown.

	1 top-tag	== 2 top-tags
no b-tag	A(0.4%)	B(2.8%)
1 b-tag	C(4.5%)	D(29.5%)
== 2 b-tag	E(29.0%)	F(88.2%)

Table 8.5: The six regions used for estimating the $t\bar{t}$ and multijet backgrounds. For each region the estimated purity of $t\bar{t}$ events is listed in parentheses. The purity is calculated as the expected number of events from SM $t\bar{t}$ production divided by the number of observed events in that region.

signal region F. The estimation of the QCD multijet background is carried out using the "ABCD" method. The use of this method relies on the independent distributions from signal and background. If a probability density function $\rho(x, y)$ is expressed using two functions $f(x)$ and $g(x)$: Improvements to the search by using track-based b-tagging and filtered C/A R=1.5 jets for $m_{t\bar{t}}$ reconstruction are discussed in Section 8.2.1 and Section 8.2.2, respectively.

$$\rho(x, y) = f(x)g(x) \tag{8.1}$$

then the distribution of events if x and y is said to be independent. The event yield in each region is determined by (as shown in Fig. 8.5):

$$n_I = \int_{x_1}^{x_2} \int_{y_1}^{y_2} dx\, dy\, \rho(x,y) \qquad n_{II} = \int_{x_3}^{x_4} \int_{y_1}^{y_2} dx\, dy\, \rho(x,y)$$

$$n_{III} = \int_{x_1}^{x_2} \int_{y_3}^{y_4} dx\, dy\, \rho(x,y) \qquad n_{IV} = \int_{x_3}^{x_4} \int_{y_3}^{y_4} dx\, dy\, \rho(x,y)$$

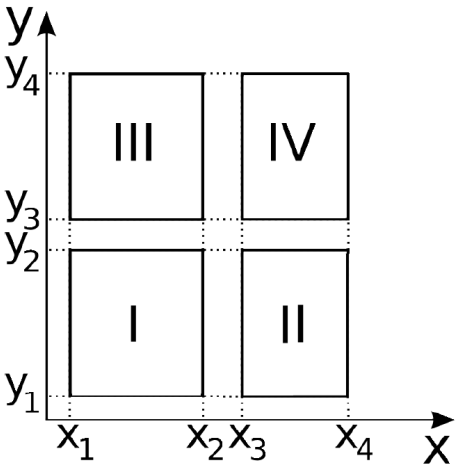

Figure 8.5: Illustration of the regions used in the ABCD method for the general case. The regions are named using roman numerals to avoid confusion with the regions used for the actual analysis which are denoted by the letters A to F. From [94].

it can be then shown that:

$$\frac{n_I}{n_{II}} = \frac{n_{III}}{n_{IV}}. \tag{8.2}$$

Eq. (8.2) allows to calculate the resulting event yield by rearranging:

$$n_{IV} = n_{III} \frac{n_{II}}{n_I}. \tag{8.3}$$

The multijet background is determined using the assumption that top-tagging and b-tagging are uncorrelated. The assumption is supported by the fact that the information from b-tagging comes from the tracking detectors, whereas the HEPTopTagger uses calorimeter information. Further support to this assumption is the fact that the control plots shown in Figs. 8.6 to 8.9 show a good description of the data by the MC and the multijet events. The "ABCD" procedure starts with the subtraction of the MC $t\bar{t}$ in

each of the regions A,B,C,D and E. No signal is subtracted from any of these regions since it is assumed to very small in comparison to the $t\bar{t}$ contribution. Afterwards, the shape in region B ($\frac{dn_B}{dm_{t\bar{t}}}$) is normalized by taking the number of events in the in region A and E:

$$\frac{dn'_F}{dm_{t\bar{t}}} = \frac{n_E}{n_A}\frac{dn_B}{dm_{t\bar{t}}} \tag{8.4}$$

The ABCD method is performed for a second time taking the shape in region D ($\frac{dn_D}{dm_{t\bar{t}}}$) and normalizing it by taking the number of events in the in region C and E as shown:

$$\frac{dn''_F}{dm_{t\bar{t}}} = \frac{n_E}{n_C}\frac{dn_D}{dm_{t\bar{t}}} \tag{8.5}$$

From these estimates a mean is calculated:

$$\frac{dn_F}{dm_{t\bar{t}}} = \frac{1}{2}\left(\frac{dn'_F}{dm_{t\bar{t}}} + \frac{dn''_F}{dm_{t\bar{t}}}\right). \tag{8.6}$$

It is also possible to use the shapes $\frac{dn'_F}{dm_{t\bar{t}}}$ and $\frac{dn''_F}{dm_{t\bar{t}}}$ to obtain a multijet shape systematic uncertainty as detailed in Section 8.6.4. The estimated number of multijet events in region F is 140.31 ± 20.35.

8.5 Control Distributions

The final yields in the signal region from the fully hadronic $t\bar{t}$ decays, the $t\bar{t}$ non-fully hadronic decays and the multijet contributions with all systematic and statistical uncertainties are shown in Table 8.6. The $t\bar{t}$ background in the signal region is 808.8 ± 358.8 events and the multijet background is 140.31 ± 15.6 events. There is a small contribution from non-fully hadronic $t\bar{t}$ decays of 32.74 ± 7.2. The number of events observed for data is 954.0 ± 30.9. The event yields are summarized in Table 8.6. The MC prediction estimates a yield consistent with data. Control distributions in the signal regions after the multijet background estimation are shown in the following. The large-R jet p_{T}, mass, η and ϕ distributions are shown in Fig. 8.6. The large-R p_{T} distribution starts at 400 GeV as specified by the 2015 selection. The filtered large-R jet p_{T}, mass, η

Type	Yield
$t\bar{t}$	808.8 ± 358.8
$t\bar{t}$ non-all	32.74 ± 7.2
multijet	140.31 ± 15.6
Total	981.85 ± 360.0
Data	954.0 ± 30.9

Table 8.6: Data and expected background event yields in the signal region for the full 2015 dataset. The total systematic and statistical uncertainty added in quadrature are also shown.

and ϕ distributions are shown in Fig. 8.7. The HEPTopTagger-related variables are also presented; (Fig. 8.8) the leading top quark candidate mass, (Fig. 8.9a) sub-leading top quark candidate mass, (Fig. 8.9b) the leading top quark candidate p_{T}, (Fig. 8.9c) the leading top quark candidate η and (Fig. 8.9d) the leading top quark candidate ϕ. The substructure variables, (Fig. 8.9e) leading top quark candidate m_{23}/m_{123} and (Fig. 8.9f) the leading top quark candidate arctan $\left(\frac{m_{13}}{m_{12}}\right)$, as described in Section 6 are also shown. All control distribution show good agreement between data and MC.

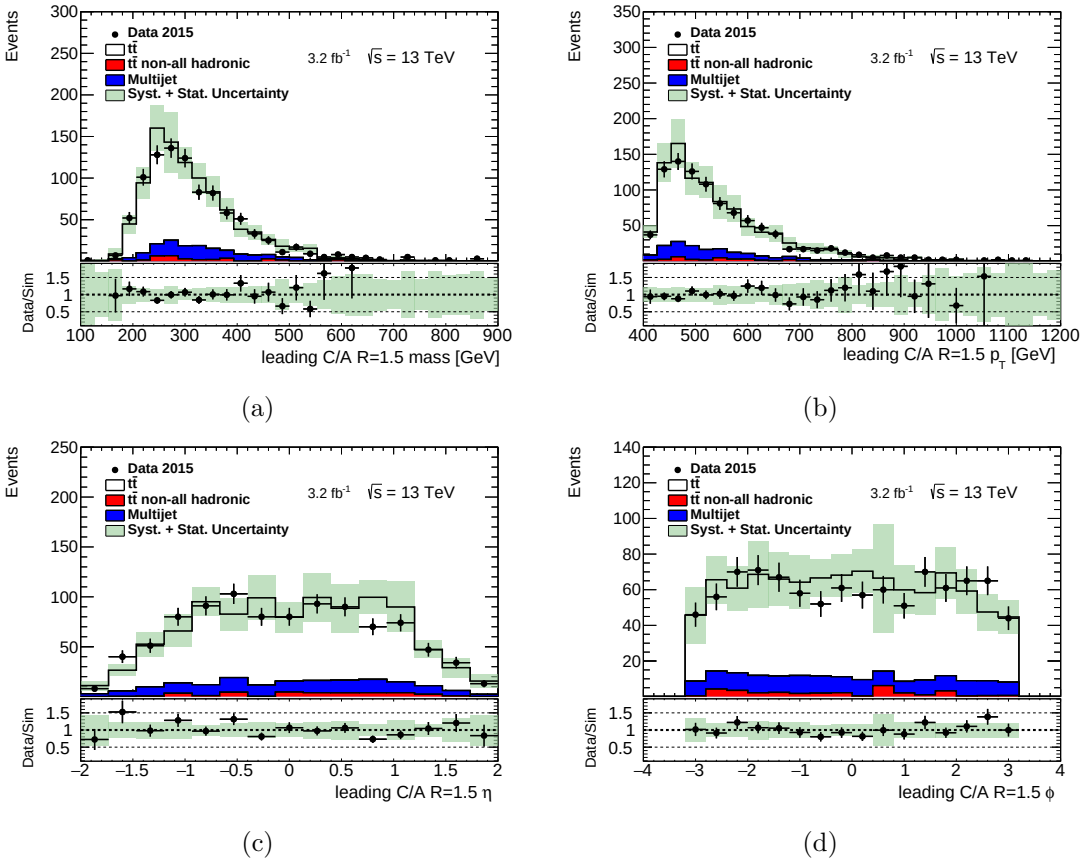

Figure 8.6: Distributions of the (a) mass, (b) p_{T}, (c) η and (d) ϕ of the p_{T}-leading C/A R=1.5 jet in the signal region. Shown stacked are the SM $t\bar{t}$ production and the multijet background contribution as estimated from data and data. The vertical bars represent the statistical uncertainty of the data events. The green bands represent the statistical and systematic uncertainty added in quadrature.

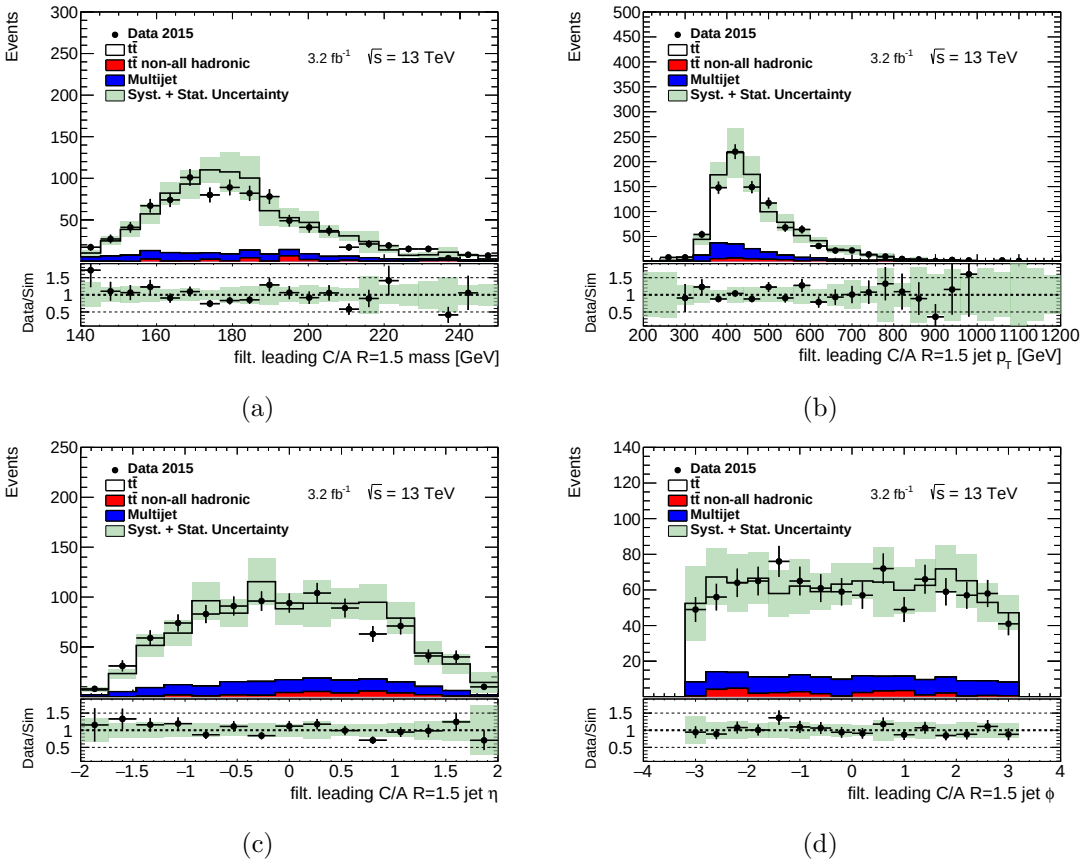

Figure 8.7: Distributions of the (a) mass, (b) p_{T}, (c) η and (d) ϕ of the p_{T}-leading **filtered** C/A R=1.5 jet in the signal region.

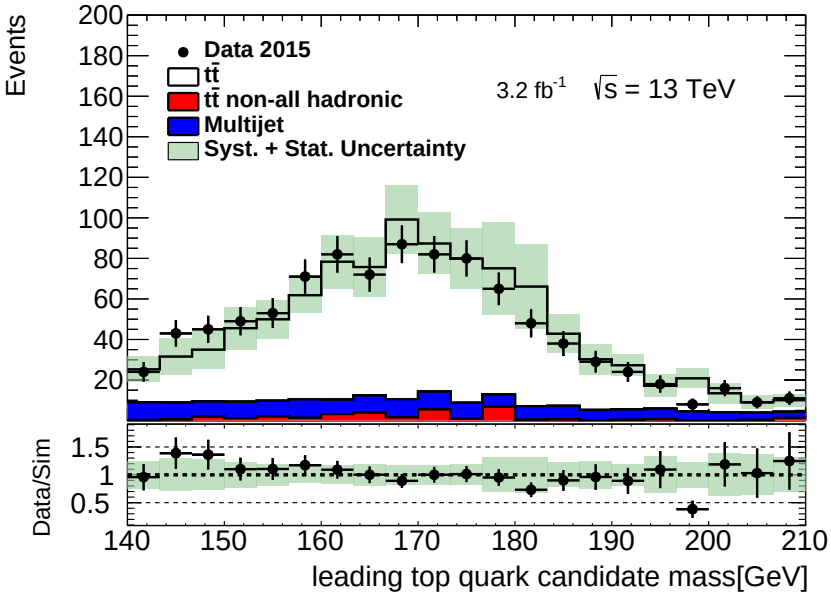

Figure 8.8: Distribution of the leading-p_{T} top quark candidate mass in the signal region.

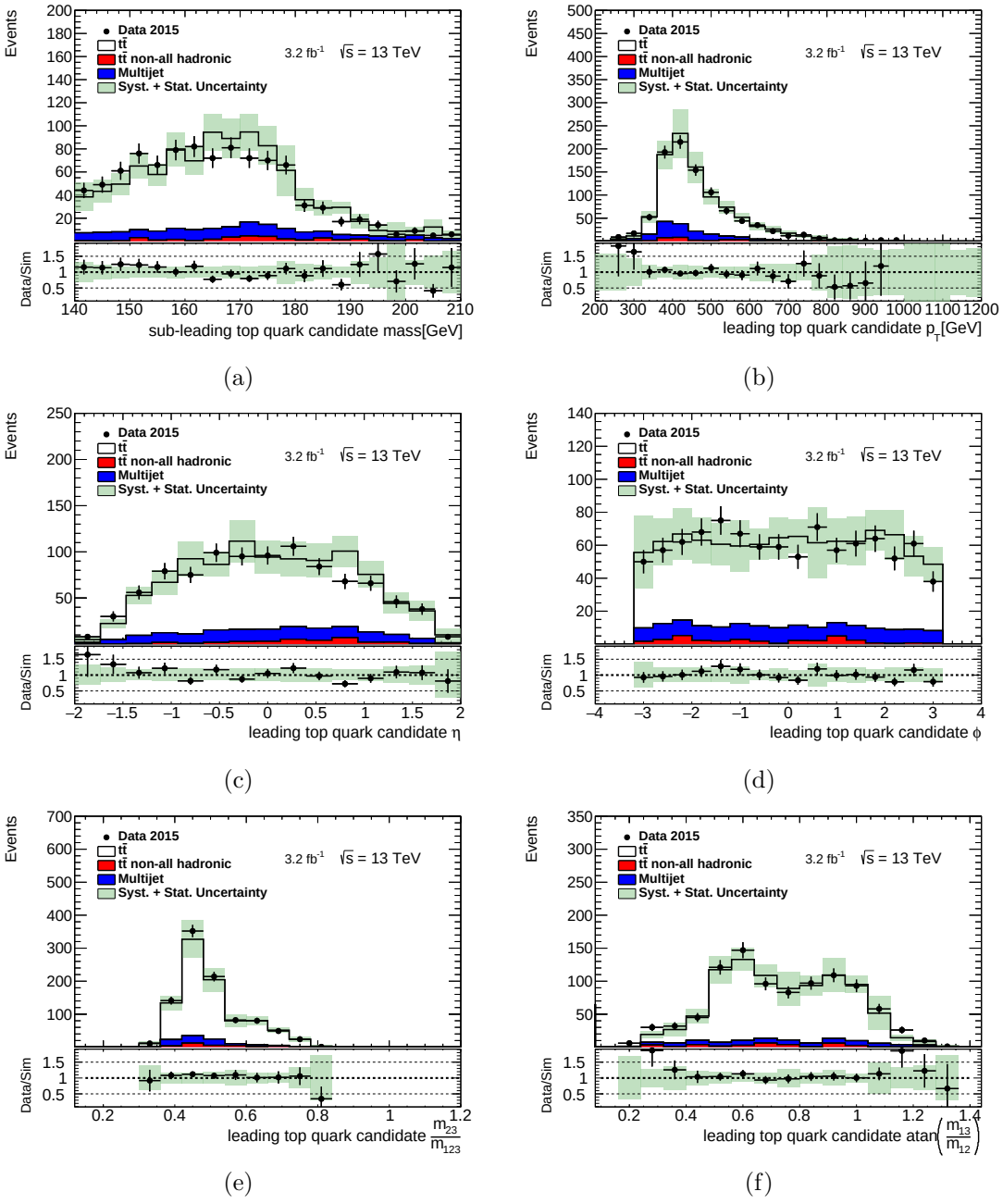

Figure 8.9: Distributions of (a) the of sub-leading-p_{T} top quark candidate mass and (b) the p_{T}, (c) η, (d) ϕ, (e) $\frac{m_{23}}{m_{123}}$ and (f) arctan $\left(\frac{m_{13}}{m_{12}}\right)$ of the leading-p_{T} top quark candidate.

8.6 Systematic Uncertainties

The $m_{t\bar{t}}$ spectrum modeled by the MC $t\bar{t}$ and the multijet samples is impacted by several sources of systematic uncertainties. All presented systematic uncertainties are including in the limit-setting procedure and the exclusion limits of the search. The following systematic uncertainties are included:

- b-tagging efficiency,
- c- light-quark mistag rate,
- b-tagging high-p_{T} extrapolation,
- luminosity,
- $t\bar{t}$ cross section,
- $t\bar{t}$ renormalization and factorization scales,
- $t\bar{t}$ initial and final state radiation,
- $t\bar{t}$ parton shower modeling,
- $t\bar{t}$ PDF uncertainties,
- $t\bar{t}$ electroweak correction and
- multijet shape.

The $m_{t\bar{t}}$ spectra obtained with the different systematic uncertainties according to the procedure explained in Appendix A to avoid changes due to statistical fluctuations. All systematic uncertainties enter the multijet background through the $t\bar{t}$ subtraction, however the shape uncertainty is the largest affecting this background.

8.6.1 *b*-tagging

The b-jet reconstruction and efficiency are explained in Section 5.5.1. To obtain the b-tagging scale factors a $t\bar{t}$ lepton plus jet selection with a high $t\bar{t}$ purity is used. To

obtain the c-jet and light quark scale factors a QCD multijet sample is used [95]. Since the more relevant sources of systematic uncertainties in the present analysis come from the b-tagging efficiency uncertainties, only these are discussed in detail in the following.

The most precise method to obtain the scale factors or calibration (and the one used in this analysis) is the combinatorial likelihood, also called the $t\bar{t}$ PDF likelihood method [96]. Compared to previous methods, such as the fitting of b-jet multiplicity [97], a large gain in precision is obtained by considering the correlations between the jets in the events. This results in reduced uncertainties when requiring b-jets in the analysis. The $t\bar{t}$ PDF likelihood method consists of the construction of a per-jet likelihood function with the flavor fractions, the probability density functions for the weight for a jet flavor for a given p_{T} and a two-dimensional PDF with p_{T} and flavor combinations. The b-jet tagging efficiency as a function of jet p_{T} in data and simulation (a) and the obtained scale factors with their corresponding uncertainty are shown in Fig. 8.10 for the MV2C20 algorithm using anti-k_t R=0.4 calorimeter jets. The principle of the calibration remains the same for the MV2c10 algorithm and the anti-k_t R=0.2 track jets used in the present search. Since the b-tagging calibrations for b and c-jets only extend up to 300 GeV in jet p_{T} with the light-jets extending to 750 GeV, a simulation-only analysis is performed to estimate a high-p_{T} extrapolation uncertainty on the b-tagging efficiency from the last calibrated p_{T} bin up to 1200 GeV. To reduce the number of systematic variations (to the number of bins used for the calibration, for example), an eigenvector variation method is carried out. It starts from the construction of the covariance matrix corresponding to each source of uncertainty. These covariance matrices are then summed to obtain the total covariance matrix. These positive-definite and symmetric matrix is solved as an eigenvalue problem. The eigenvectors that solve this problem are understood as "directions" in which to carry out independent variations. The sizes of the variations are given by the square root of the corresponding eigenvalues. There are 64 (4 and 12) eigenvectors for the b-flavor (c- and light-flavor) quarks and 2 eigenvectors specifically for the extrapolation of the scale factor in high p_{T} regimes, which are correlated across the flavors. After the eigenvector reduction, only the first 5 eigenvalues (4 and 12) for

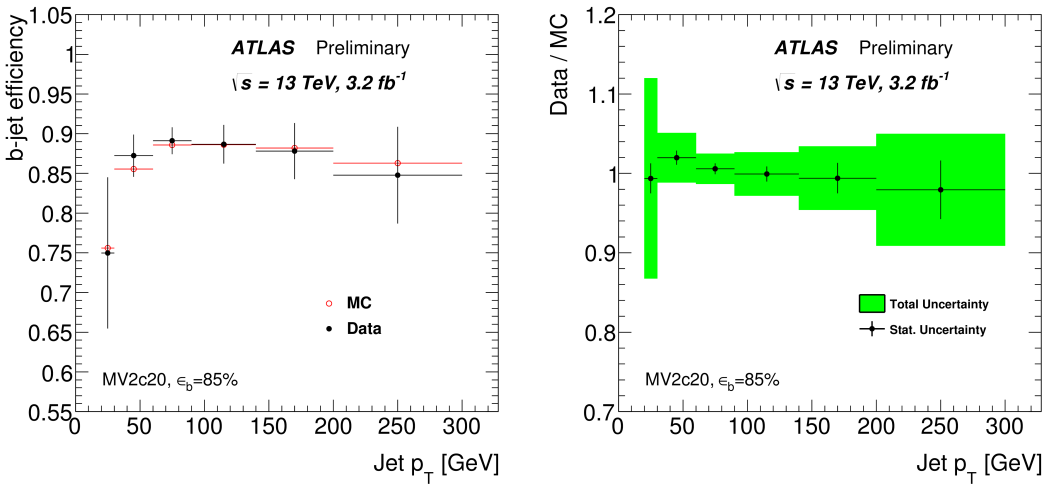

Figure 8.10: (a) b-tagging efficiency as a function of anti-k_t R=0.4 jet p_{T} for data and $t\bar{t}$ MC. (b) Data $t\bar{t}$ MC ratio as a function of anti-k_t R=0.4 jet [98].

the b-flavor (c- and light-flavor) are used as a systematic uncertainty in the analysis. The impact of the systematic uncertainties from the b-tagging scale factors are obtained by substituting the nominal scale factors, by scale factors increased and decreased by one standard deviation. This is carried out for the tagging efficiency in true b-jets and the mis-tag rate in true c-jets and true light-quark and gluon jets. The scale factors are only derived for jets with p_{T} up to 300 GeV. Hence an additional extrapolation uncertainty is needed for jets with $p_{\mathrm{T}} > 300$ GeV.

Each of the track jets used in the event has a weight. Multiplying all weights of all track jets which satisfy the kinematic criteria outlined in Section 8.3, an event weight is obtained. The impact of the b-, c-, light-quark and extrapolation scale factors on the $m_{t\bar{t}}$ distribution is shown in Figs. 8.11a to 8.11d and 8.12b respectively. The largest contribution comes from the eigenvector components 0 and 1 of the b-tagging efficiency with an impact on the total added background of 7.9% and 3.2% respectively.

8.6.2 Luminosity

The methods to measure the luminosity is ATLAS were explained in detail in Section 4.6. The relevant contributions to the uncertainty of this measurement come from effects that

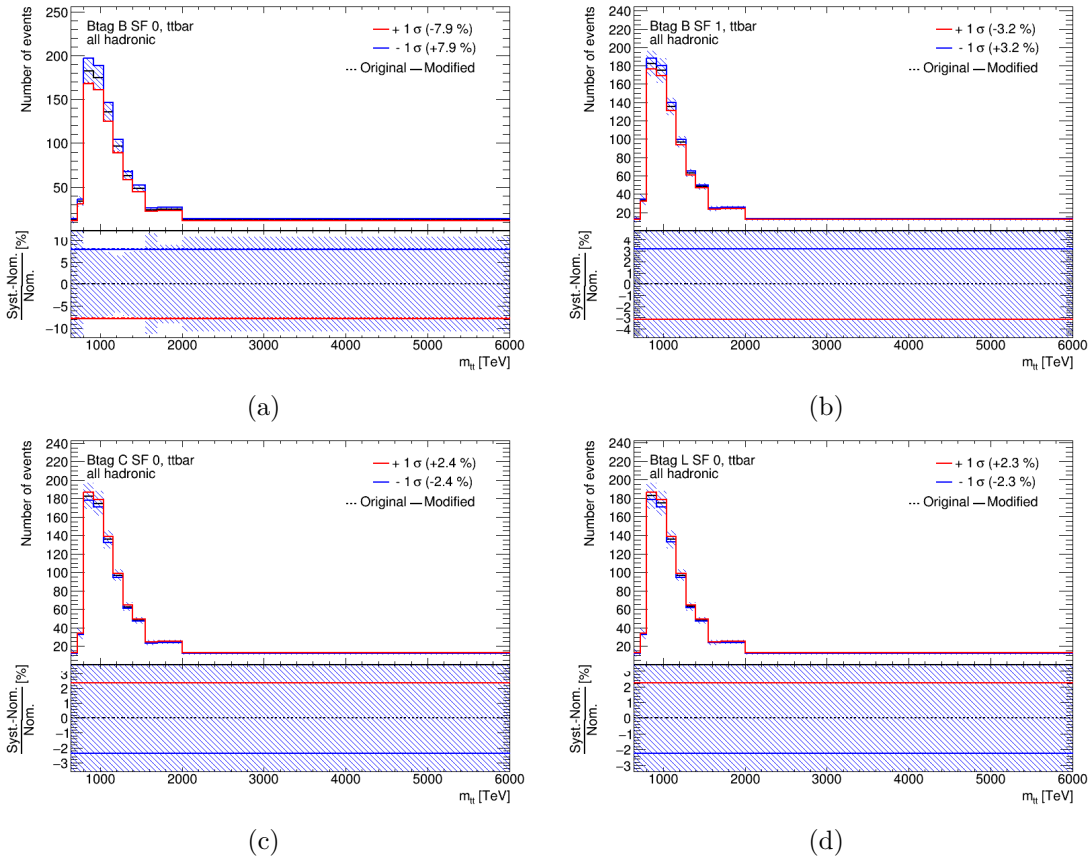

Figure 8.11: Impact on the $m_{t\bar{t}}$ distribution for the $t\bar{t}$ sample for the (a) b-quark tagging (eigenvector 0) (b) b-quark tagging (eigenvector 1) (c) c-quark mistag rate (eigenvector 0) and light-quark mistag rate (eigenvector 0) uncertainties. In the top section of each figure, the $m_{t\bar{t}}$ distributions corresponding to an integrated luminosity of 3.2 fb^{-1} are shown with the corresponding systematic variation changed by $\pm 1\sigma$. The bottom part of the figures show the relative change for the corresponding uncertainty. Note that the y-axis range may be different. The histograms are smoothed according to the procedure outlined in Appendix A. The shaded band represents the statistical uncertainty.

influence the results of the van-der-Meer scans such as correlations between beam positions, variation in the cross section, changes in emittance during the scan, dependence in μ and beam-beam effects. A total uncertainty of $\pm 2.1\%$ is calculated for an integrated luminosity of 3.2 fb^{-1} [99]. This systematic uncertainty affects all processes in which the event yield from simulation is used. The effect on the total added background event yield is 1.8%.

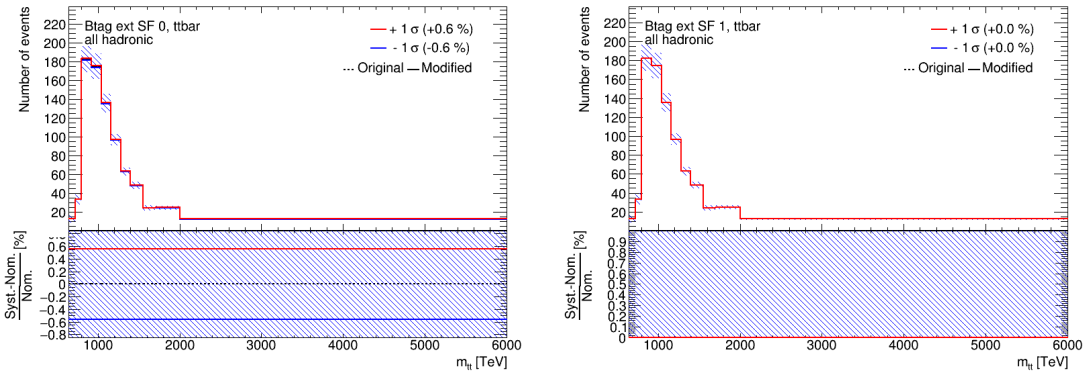

(a) (b)

Figure 8.12: Impact on the $m_{t\bar{t}}$ distribution for the $t\bar{t}$ sample for the (a) b-tagging extrapolation for high-p_{T} jets and (b) b-tagging extrapolation for high-p_{T} for high-p_{T} including charm quarks uncertainties.

8.6.3 Jet Energy Scale and Resolution

A sample containing QCD dijet events where light quarks and gluons give rise to jets can be used to determine the difference in the subjet jet energy scale (sJES) between data and simulation. A JES uncertainty would be determined by comparing the double ratio of data and simulation and energy of jets constructed from topoclusters and tracks using the same jet-clustering algorithm. The subjet jet energy resolution (sJER) is determined using the p_{T} asymmetry in dijet events. Because the resolution in simulated events is usually better than what is observed in data the simulated resolution is accordingly worsened. At the time of writing no sJES/sJER were available in the ATLAS collaboration for the 13 TeV dataset. Work is ongoing to obtain these uncertainties. For the 8 TeV dataset, the sJES uncertainty was estimated to be 1.1%, while the sJER uncertainty was estimated to be 0.7% [85]. It is expected that for the 13 TeV dataset, these uncertainties will be comparable. Therefore, the conclusions reached in the thesis will not be greatly changed.

8.6.4 Multijet Estimate Uncertainty

A multijet uncertainty is obtained by taking the different multijet templates obtained from regions B and D after the $t\bar{t}$ subtraction (as shown in Fig. 8.13) and from a bin-by-bin difference. This uncertainty on the multijet shape is around 12%. The histograms have been smoothed according to the procedure explained in Appendix A to avoid changes due to statistical fluctuations. The impact on the total added background is 1.2%.

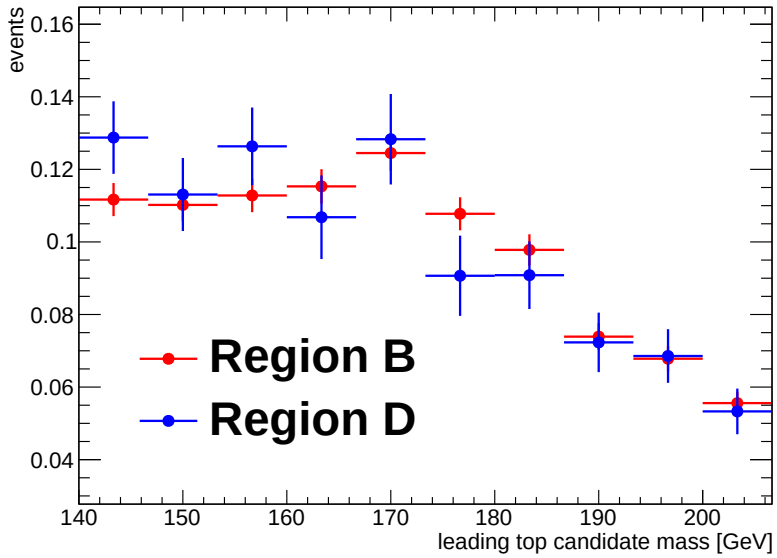

Figure 8.13: Multijet templates from regions B and D. An multijet uncertainty is obtained by getting the bin-by-bin difference.

8.6.5 $t\bar{t}$ Cross Section Uncertainty

The $t\bar{t}$ cross section is obtained at NNLO in QCD with a total uncertainty of +5/-6%. The uncertainty includes systematic uncertainties from the PDF choice and α_s and the uncertainty on the top quark mass.The effect on the total added background event yield is 5.2%. The effect of the choice of hard scatter model is shown in Fig. 8.14a.

8.6.6 Hard Scatter Generation

A systematic uncertainty for the hard scatter matrix element is obtained by comparing the $m_{t\bar{t}}$ shapes obtained with MC generators POWHEG and MC@NLO. For this comparison both samples use HERWIG to model the parton shower. Since the shower model is the same, any resulting differences in the $m_{t\bar{t}}$ shape should come from the choice of hard scatter model. The differences between these two model are symmetrized. The relative difference is estimated for bin i in the $m_{t\bar{t}}$ distribution as:

$$\Delta_i = \frac{(A_i - B_i)}{(1/2)(A_i + B_i)} \tag{8.7}$$

In this formula the placement of the different samples does not change the final result. The resulting shape uncertainty is obtained by multiplying the nominal bin i value by this relative difference:

$$n_{\text{nominal},i} \cdot (1 \pm \Delta_i) \tag{8.8}$$

where $n_{\text{nominal},i}$ is the value of bin i the nominal POWHEG+PYTHIA sample. The effect of the choice of hard scatter model is shown in Fig. 8.14d. The effect on the total added background event yield is 19.9%.

8.6.7 Parton Shower Model

The evaluation of the uncertainty coming from different parton shower models is evaluated by using POWHEG simulated the hard scatter and comparing different models to simulate the parton shower: PYTHIA and HERWIG. Eqs. (8.7) and (8.8) are applied to obtain the systematic uncertainty. The effect of the choice of parton shower model is shown in Fig. 8.14c. The effect on the total added background event yield is 17.3%.

8.6.8 Initial and Final State Radiation

Shape comparison between two different POWHEG+PYTHIA samples, which have modified shower radiation, factorization and renormalization scale and NLO radiation

are compared. Eqs. (8.7) and (8.8) are applied to obtain the systematic uncertainty. The effect of the choice of additional radiation parameters is shown in Fig. 8.14b. The effect on the total added background event yield is 21.6%.

8.6.9 Parton Distribution Function

The PDF and α_s uncertainties are estimated using the PDF4LHC15 prescription [100, 101]. PDF4LHC15 prescription combines the MSTW2008 68% CL NNLO, CT10NNLO and NNPDF2.3 5f FFN [102] PDF sets added in quadrature. This approach of estimating the impact of the PDF uncertainty has the advantages that is much more convenient for the final user and it is statistically better defined than the CT14, MMHT14 and NNPDF3.0 envelope. It is also less conservative than the envelope of these 3 PDF sets. PDF uncertainties are obtained through reweighting. This avoids the re-generation of samples with different PDF conditions. The effect on the total added background event yield is 1.7%. The histograms have been smoothed according to the procedure explained in Appendix A to avoid changes due to statistical fluctuations.

8.6.10 Higher Order Electroweak Correction

Large (negative) corrections at high momentum transfers and large partonic energies $\hat{s} = m_{t\bar{t}}$ affect kinematic distributions such as the p_{T} of the top quark and $\hat{s} = m_{t\bar{t}}$. Therefore scale factors have been derived to account for this effect [103]. The effect on the total added background event yield is 0.5%. The histograms have been smoothed according to the procedure explained in Appendix A to avoid changes due to statistical fluctuations.

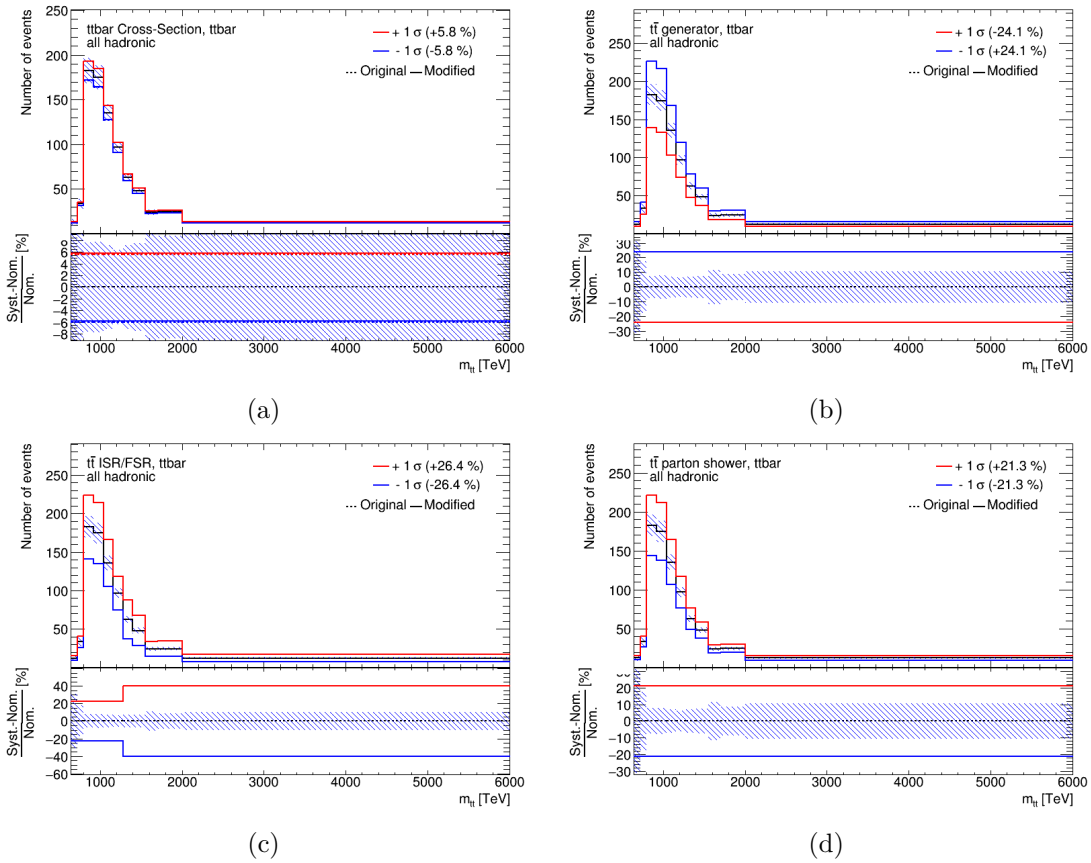

Figure 8.14: Impact on the $m_{t\bar{t}}$ distribution for the $t\bar{t}$ sample for the (a) $t\bar{t}$ cross section, (b) additional $t\bar{t}$ radiation, (c) parton shower modeling and (d) and generator modeling uncertainties.

Systematics	Percentage Variation
b-tagging eff.	6.8
c mistag eff.	2.6
l mistag eff.	1.8
b-tagging extrap.	0.5
luminosity	1.8
$t\bar{t}$ cross section	5.2
$t\bar{t}$ generator	19.9
$t\bar{t}$ p. shower	17.3
$t\bar{t}$ ISR/FSR	21.6
$t\bar{t}$ PDF	1.7
$t\bar{t}$ electroweak	0.5
multijet shape	1.1
Total	36.6

Table 8.7: Estimated relative change in event yield due to systematic uncertainties for the SM background.

8.7 Resuls

The $m_{t\bar{t}}$ distributions for data, background ($t\bar{t}$ and multijet) and the signal are shown in Fig. 8.15 along with Z' boson signal for two masses of 2 and 3 TeV. The Z' boson cross sections have been multiplied times 10 for better visibility. No significant excess is observed over the SM $t\bar{t}$ and multijet backgrounds.

In the absence of signal, a frequentist approach using the CLs method is used to set 95% Confidence Level (CL) cross section limits on the hypothesis that the data is consistent with the Standard Model background and signal. The likelihood in the signal region is defined as:

$$L(\mu,\Theta) = \prod_{i=0}^{\text{channels,bins}} \frac{e^{-\mu\, a_{Z',i}\, \sigma_{Z'}+b_i}(\mu\, a_{Z',i}\, \sigma_{Z'}+b_i)^{D_i}}{\Gamma(D_i+1)} C(\Theta) \tag{8.9}$$

where D is the expected data yield, b is the expected background yield, $\sigma_{Z'}$ is the cross-section of the Z' signal, $a_{Z'}$ is the acceptance of the signal and μ is the signal strength, which is the parameter of interest. The function C indicates a set of of constraints applied on the nuisance parameters Θ , such as the systematic uncertainties in the background and signal, and the luminosity measurement uncertainty. The hypothesis testing is based on the profile likelihood ratio test statistic *Llambda* as follows:

$$\Lambda(\mu) = \frac{L(\mu,\hat{\hat{\Theta}}(\mu))}{L(\hat{\mu},\hat{\Theta}(\mu))} \tag{8.10}$$

where the single circumflex indicates the unconditional maximum likelihood estimate of a parameter and the double circumflex indicates the maximum likelihood estimate assuming a specific value of μ. According to Wilk's Theorem, the distribution of the test statistic -2ln($\Lambda(\mu)$) follows a χ^2-distribution in the large-sample limit. The quantiles of the $\chi^2_{1-\alpha}$ of the χ^2-distribution is used to evaluate $1-\alpha$ confidence intervals [104]. With this procedure, 95% CL on the upper limit of the signal production cross-section times branching ratio. To include systematic uncertainties, the profile likelihood ratio is used and the evaluation of a μ, requires a minimization in all other parameters Θ. This

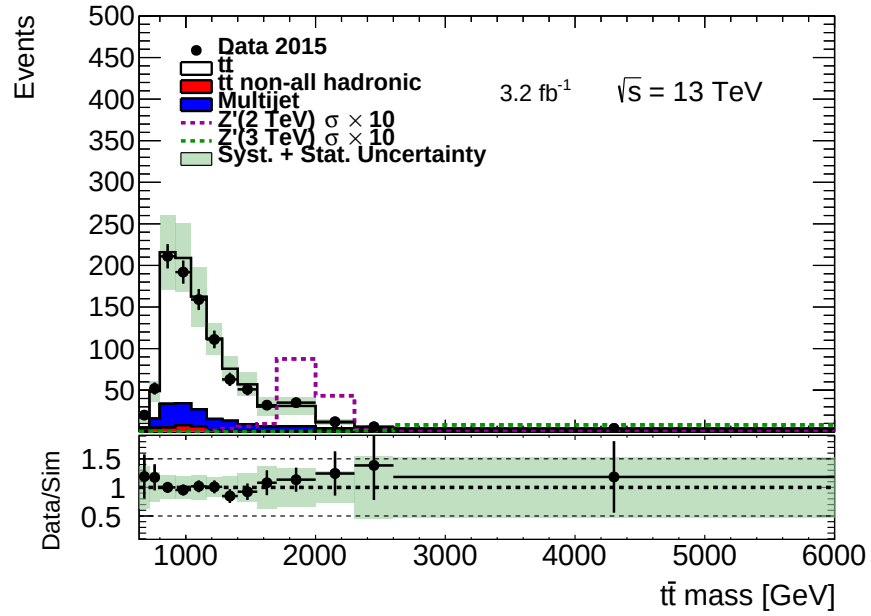

(a)

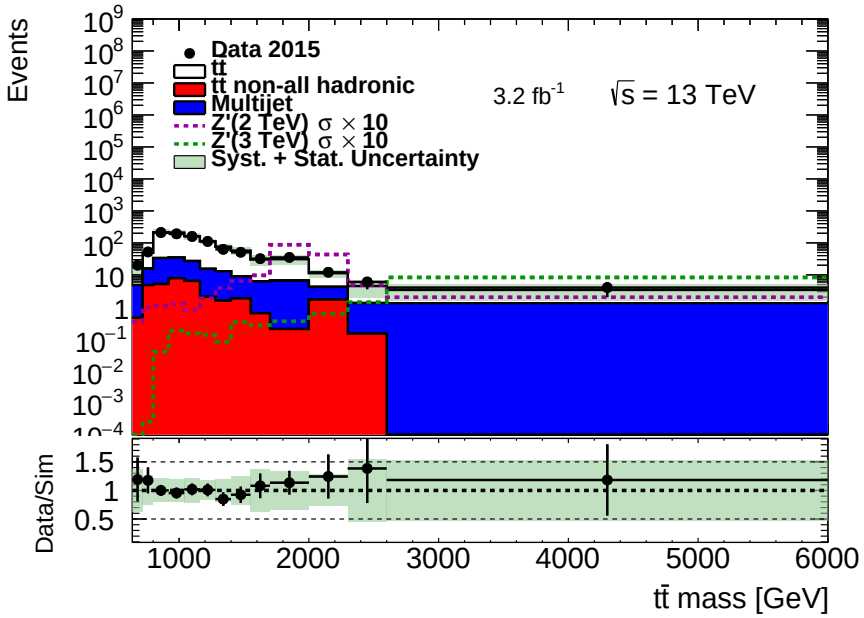

(b)

Figure 8.15: Distributions of $m_{t\bar{t}}$ in the signal region for (a) a linear scale and (b) a logarithmic scale. The distributions are obtained after the 2015 selection and normalized to 3.2 fb^{-1}. The SM fully hadronic $t\bar{t}$, the multijet background contribution as estimated from data and the SM non-fully hadronic $t\bar{t}$ are shown stacked. Two hypothetical Z' boson resonances with masses of 2 and 3 TeV with their cross sections multiplied by a factor of 10 are also shown. The green bands represent the statistical and systematic uncertainty added in quadrature.

procedure is carried out for Z' boson masses in the range from 0.75 to 4 TeV using their corresponding theoretical cross sections.

The measured cross section limits are compared to theoretical cross section calculations to obtain corresponding mass limits. The expected and observed limits on the Z' $\rightarrow t\bar{t}$ production times branching fraction as a function of Z' boson mass are shown in Fig. 8.16. The cross-section of a Z' boson with two different widths (1.2% and 3%) are shown. These cross sections have been multiplied by the NLO factor of 1.3. Systematic uncertainties are included as nuisance parameter which are marginalized to calculate confidence intervals. The analysis excludes Z' boson (width $\Gamma/m = 1.2\%$) masses from 0.77 GeV to 1.65 GeV. The expected exclusion limits are from 0.75 GeV to 1.83 GeV. These yields are summarized in Table 8.8. The observed and expected exclusion limits on $\sigma \times BR$ limits for the Z' boson are shown in Table 8.9 for a Z' boson mass with width $\Gamma/m = 1.2\%$.

Model	obs. limit [TeV]	exp. limit [TeV]
Z'	$0.75 < m_{Z'} < 1.65$	$0.75 < m_{Z'} < 1.83$

Table 8.8: Observed and expected exclusion regions on the Z' boson mass with width $\Gamma/m = 1.2\%$.

The impact of the systematic uncertainties on the exclusion limits is evaluated by removing a particular uncertainty as a nuisance parameter and re-running the limit-setting procedure as shown in Table 8.10. The numbers shows the relative improvement [%] with respect to the default limit (which includes all systematic uncertainties) on the cross section limit for all Z' boson masses. This procedure is done for the $t\bar{t}$ modeling and b-tag E0 systematic. The last column in Table 8.10 shows the improvement obtained including only systematic uncertainties. The greatest impact comes from the $t\bar{t}$ ISR/FSR systematic uncertainty, whose removal constitutes the largest improvement of all presented uncertainties.

The MC simulation prediction is fitted to the observed data and the nuisance parameters are profiled. The pre-fit and post-fit (before and after profiling) distributions in Fig. 8.17 show the reduction of the systematic uncertainties after they are profiled and

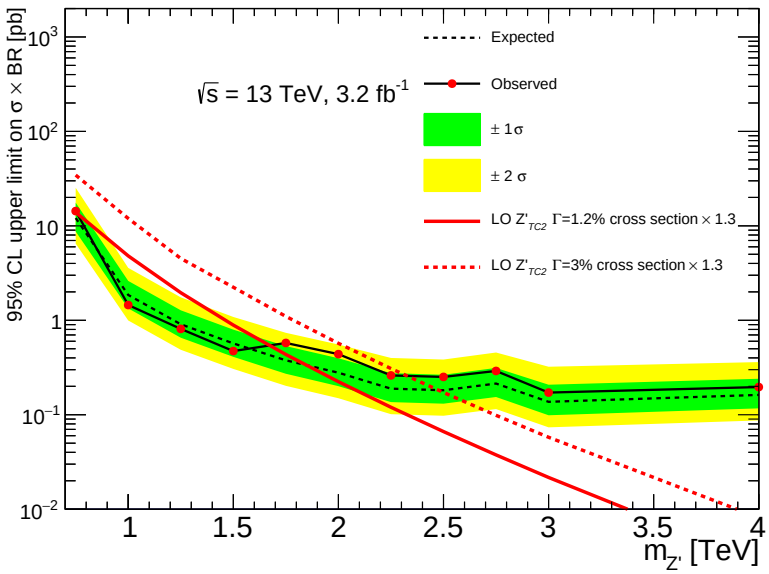

Figure 8.16: The observed and expected upper limits at 95% CL on the production cross section times branching fraction $\sigma \times BR$ for Z'_{TC2} signal full 2015 dataset. The theoretical predictions for the production cross section times branching ratio at the corresponding masses for two different Z' widths are also shown.

Z' [GeV]	obs. $\sigma \times BR$	exp. $\sigma \times BR$
750	14.338	12.102
1000	1.452	1.856
1250	0.811	0.908
1500	0.472	0.57
1750	0.576	0.377
2000	0.438	0.279
2250	0.261	0.189
2500	0.252	0.182
2750	0.291	0.214
3000	0.172	0.137
4000	0.002	0.002

Table 8.9: Observed and expected 95% confidence limits on $\sigma \times BR$ for all investigated Z' boson masses.

allowed to float. The pulls of the post-fit nuisance parameters (NP) from a background-only fit are shown in Fig. 8.18. A pull centered at zero indicates that there was no adjustment for the background prediction. Consequently a large pull indicates a large adjustment. No large pulls from zero are observed for any of the systematic uncertainties with the $t\bar{t}$ ISR/FSR being the largest. Additionally, the error bars represent the size of the NP's after profiling (starting at 1 before profiling). A error bar smaller than 1 means that the corresponding NP is being constrained. The $t\bar{t}$ modeling NPs show the largest constrainment.

Z' [GeV]	no PS[%]	no gen.[%]	no ISR/FSR[%]	no b-tag E0[%]	only stat.[%]
750	0.28	0.42	0.46	0.06	9.4
1000	1.38	2.21	4.97	0.13	26.22
1250	0.26	0.36	0.56	0.0	22.0
1500	1.47	2.05	23.87	0.17	31.78
1750	0.69	0.95	11.93	0.06	16.41
2000	0.38	0.54	6.7	0.03	9.66
2250	0.13	0.18	2.22	0.02	3.55
2500	0.14	0.17	1.61	0.01	2.64
2750	0.08	0.15	1.37	0.01	2.3
3000	0.12	0.13	1.21	0.01	2.07
4000	0.11	0.18	1.68	0.06	2.97

Table 8.10: Relative improvement (with respect to the default limit (which includes all systematic uncertainties)) [%] on the cross section limit for all Z' boson masses investigated for the removal of the parton shower, generator, ISR/FSR, b-tag and all systematic uncertainties (only statistical uncertainties). Only the main uncertainties are listed.

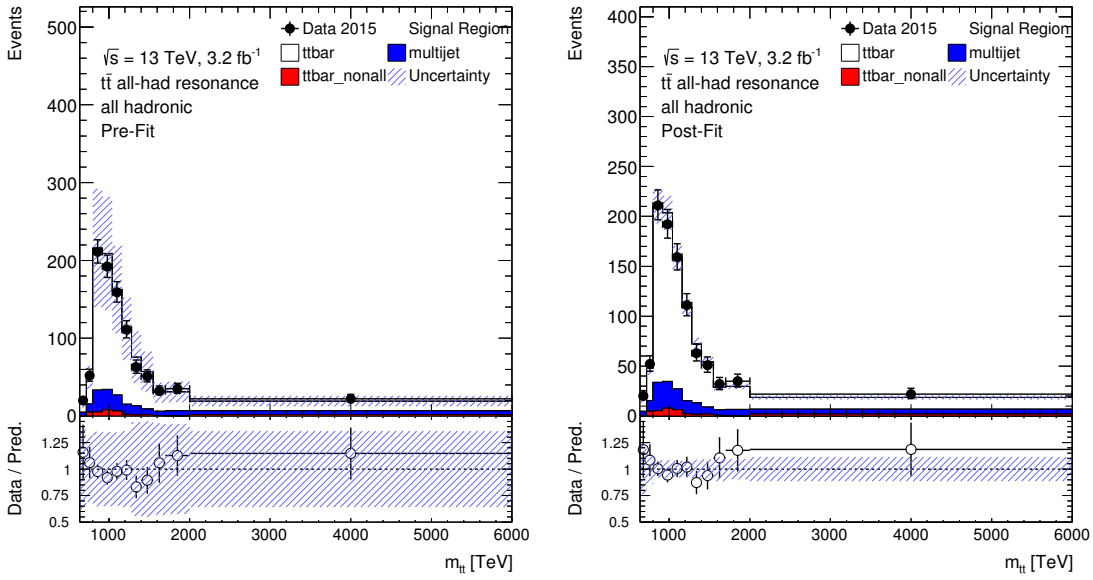

(a) (b)

Figure 8.17: $m_{t\bar{t}}$ spectrum for (a) pre-fit and (b) post-fit procedures.

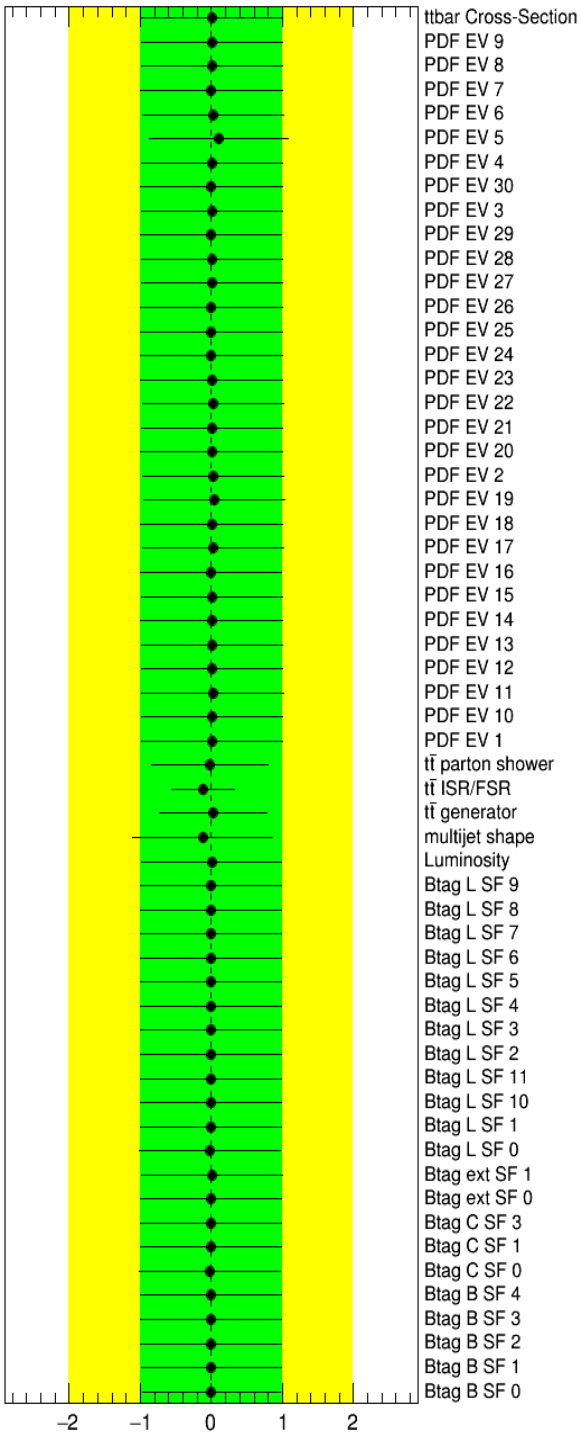

Figure 8.18: Pull of the post-fit nuisance parameters for a fit performed under the background hypothesis using the ATLAS data.

8.7.1 Expected Limits with 2016 data

Using 2016 data, expected upper limits at 95% CL are obtained for the Z' boson. The procedure follows is the same previously detailed. It was decided to keep the $m_{t\bar{t}}$ spectrum blinded in order to allow any future changes or optimizations in the analysis. Due to a higher luminosity, the large-R jet trigger p_{T} threshold was increased from 360 GeV to 420 GeV. Correspondingly, the threshold on the C/A R=1.5 leading jet is increased from 400 GeV to 500 GeV. The final yields in the signal region from the fully hadronic $t\bar{t}$, $t\bar{t}$ coming from non-fully hadronic decays and multijet contributions with all systematic and statistical uncertainties are shown in Table 8.11. The $t\bar{t}$ background in the signal region is 1844.47 $\pm$ 625.4 events and the multijet background is 452.23 $\pm$ 68.6 events. There is small contribution from the non-fully hadronic $t\bar{t}$ decays of 86.65 $\pm$ 13.9. The number of events observed for data is 2317.0 $\pm$ 48.1. The event yields are summarized in Table 8.6. The MC prediction estimates a yield consistent with data. The top quark candidate mass distribution obtained with 11.5 fb^{-1} is shown in Fig. 8.19. The other relevant HEPTopTagger variables are shown in Fig. 8.20. The MC modeling remains good when using the 2016 dataset and changing the trigger conditions. The corresponding $m_{t\bar{t}}$ distribution is shown in Figs. 8.21a and 8.21b. The measured cross section limits are compared to theoretical cross section calculations to obtain corresponding mass limits. The expected and observed limits on the $Z' \to t\bar{t}$ production times branching fraction as a function of Z' boson mass are shown Fig. 8.22. The expected exclusion limits are from 0.83 GeV to 2.37 GeV for a Z' boson of width $\Gamma/m = 1.2\%$. The observed and expected exclusion limits on $\sigma \times BR$ limits for the Z' boson as a function of mass are shown in Table 8.9 for all masses investigated. A comparison of the observed limits for 2015 and 2016 with the corresponding change is presented in Section 8.7.1. Note that for a Z' boson mass of 750 GeV the limit worsens. This is due to the raise trigger and leading large-R jet p_{T} thresholds. A combination of the 2015 and 2016 dataset will recover the better limits at low Z' boson mass.

Sample	Yield
$t\bar{t}$	1844.47 ± 625.4
$t\bar{t}$ non-all	86.65 ± 13.9
multijet	452.23 ± 68.6
Total	2383.35 ± 633.6
Data	2317.0 ± 48.1

Table 8.11: Data and expected background event yields in the signal region for 11.5 fb^{-1} of the 2016 dataset. The total systematic and statistical uncertainty added in quadrature are also shown.

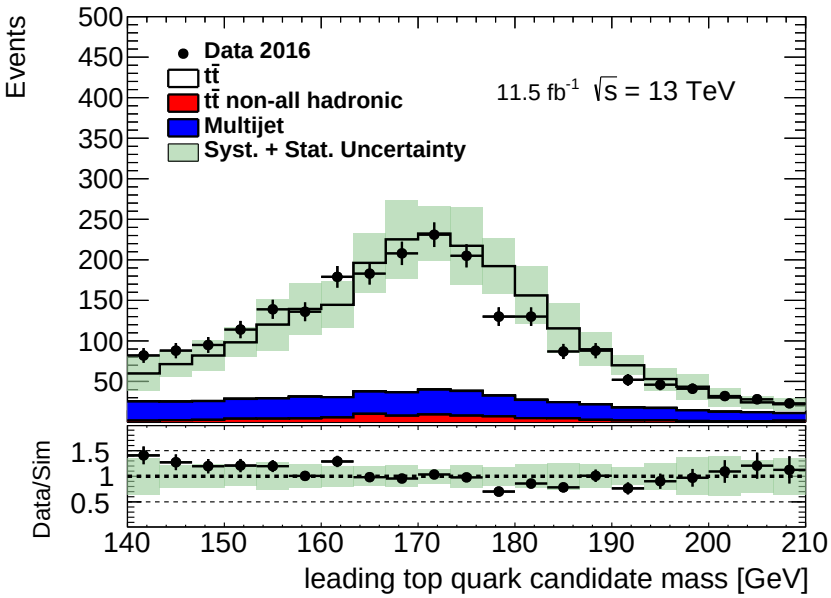

Figure 8.19: Distribution of the mass of the leading p_{T} top quark candidate in the signal region. The SM fully hadronic $t\bar{t}$, multijet background contribution as estimated from data and the SM non-fully hadronic $t\bar{t}$ are shown stacked. The vertical bars represent the statistical uncertainty of the data events. The green bands represent the statistical and systematic uncertainty added in quadrature. The vertical bars represent the statistical uncertainty of the data events.

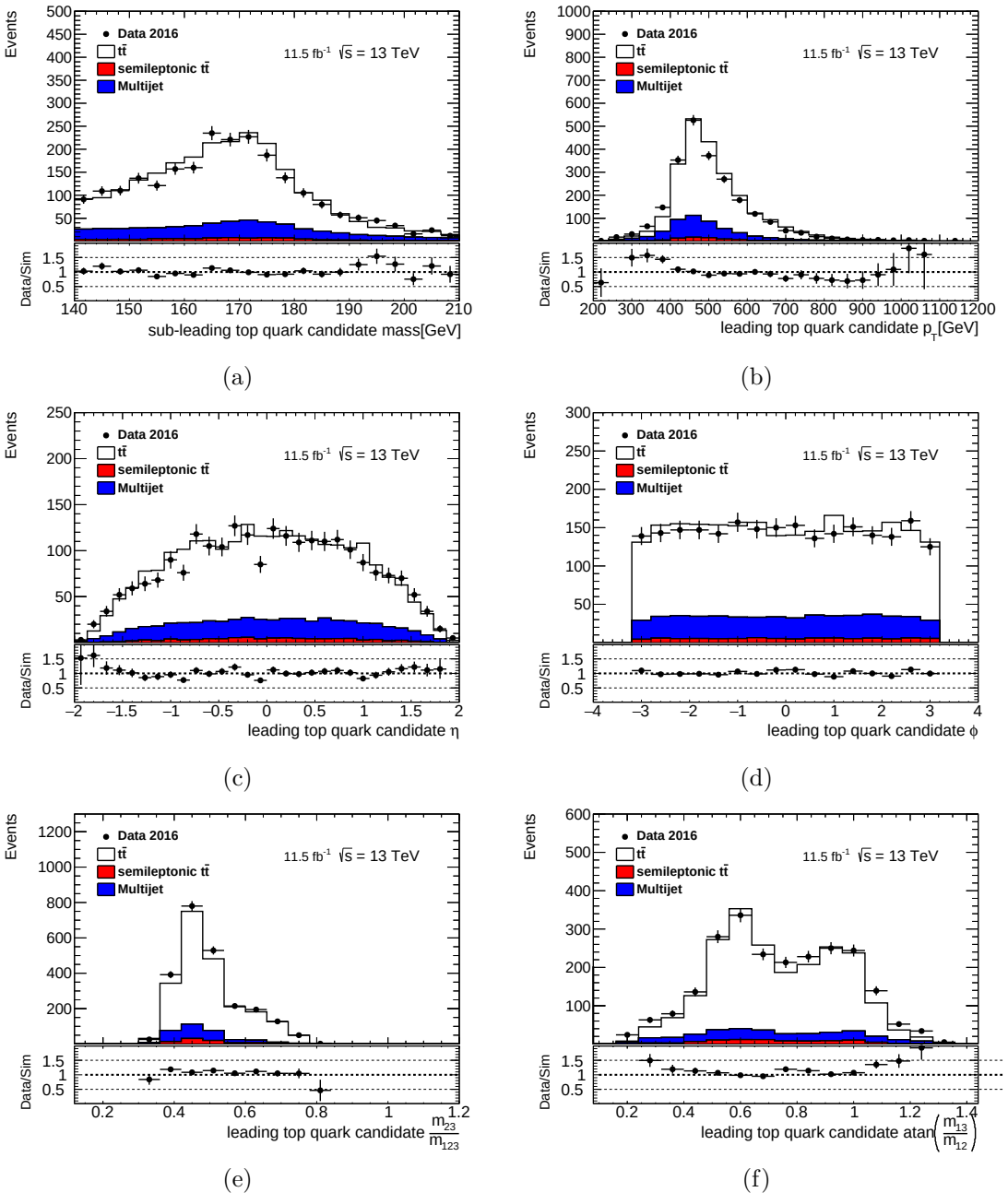

(a) (b) (c) (d) (e) (f)

Figure 8.20: Distributions of (a) the mass of the subleading-p_{T} top quark candidate and (b) the p_{T}, (c) η, (d) ϕ, (e) $\frac{m_{23}}{m_{123}}$, (f) arctan $\left(\frac{m_{13}}{m_{12}}\right)$ of the leading-p_{T} top quark candidate. Only statistical uncertainties of data are shown.

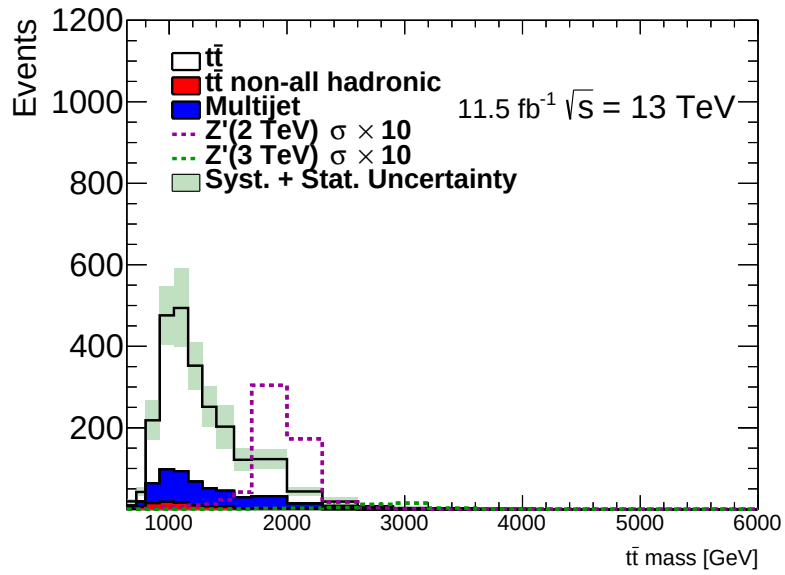

(a)

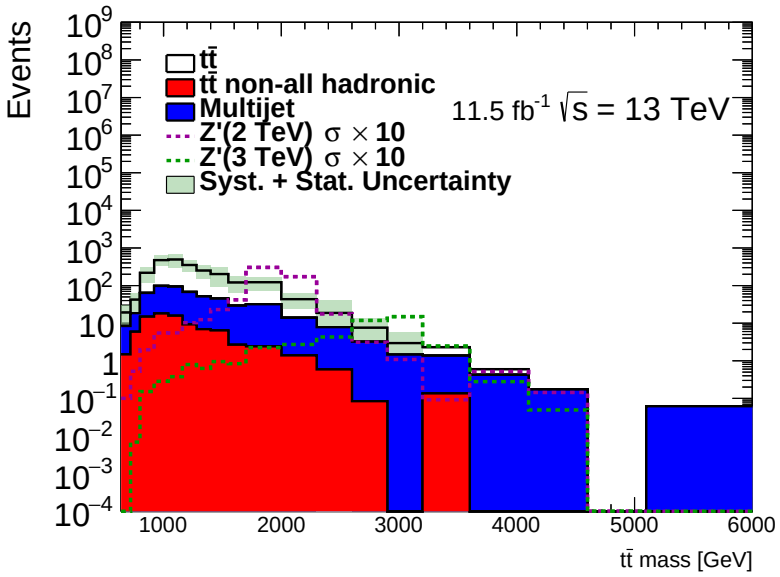

(b)

Figure 8.21: Distributions of $m_{t\bar{t}}$ in the signal region for (a) a linear scale and (b) a logarithmic scale. The distributions are obtained after the 2016 selection and normalized to 11.5 fb^{-1}. The SM fully hadronic $t\bar{t}$, the multijet background contribution as estimated from data and the SM non-fully hadronic $t\bar{t}$ are shown stacked. Two hypothetical Z' signals with masses of 2 and 3 TeV with their cross sections multiplied by a factor of 10 are shown. The green bands represent the statistical and systematic uncertainty added in quadrature.

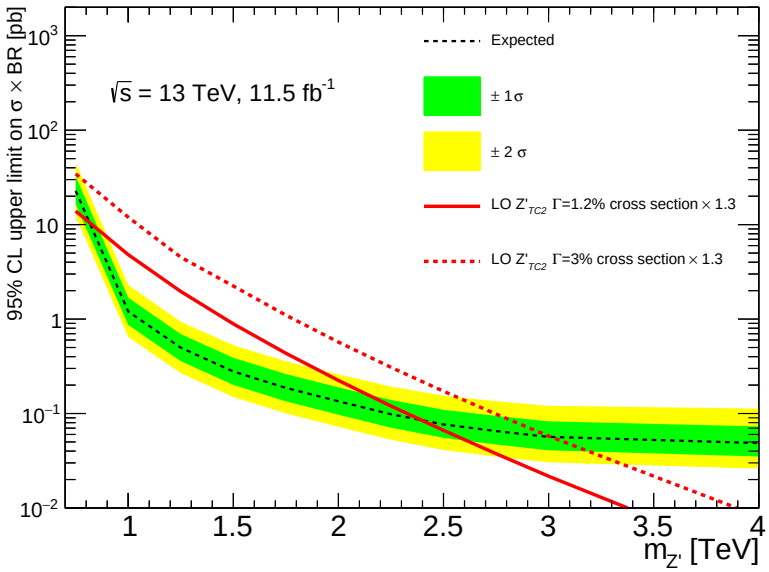

Figure 8.22: The expected upper limits at 95% CL on the production cross section times branching fraction $\sigma \times BR$ as a function of the $Z^{'}$ mass. The 2016 configuration is applied to all simulated samples and they have been normalized to 11.5 fb^{-1}. The theoretical predictions for the production cross section times branching ratio at the corresponding masses for two different Z' widths are also shown.

Z' [GeV]	2016 (11.5 fb^{-1})	2015 (3.2 fb^{-1})	Change [%]
750	22.82	12.102	-46
1000	1.20	1.856	55
1250	0.50	0.908	81
1500	0.28	0.57	103
1750	0.19	0.377	98
2000	0.13	0.279	114
2250	0.10	0.189	89
2500	0.08	0.182	127
2750	0.07	0.214	205
3000	0.06	0.137	128
4000	0.001	0.002	100

Table 8.12: Expected 95% confidence limits on $\sigma \times BR$ for all investigated Z' boson masses with the 2015 and 2016 datasets. The last column indicates the relative change.

9 Conclusion and Outlook

Two main studies constitute the results of this thesis. The first presented study is a measurement of the top quark tagging and mistag efficiency using the HEPTopTagger algorithm with the full 2012 dataset (20.3 fb^{-1}) collected by the ATLAS experiment at $\sqrt{s} = 8$ TeV. For the top tagging efficiency measurement, an isolated lepton and missing transverse energy provides a samples dominated by lepton plus jets $t\bar{t}$ final states. The requirement of b-tagged jets further increases the $t\bar{t}$ purity. The high $t\bar{t}$ purity of this channel makes it ideal for detailed top tagging studies. The top quark tagging efficiency is measured down to a transverse momentum of 200 GeV, taking into account all relevant systematic uncertainties. For the mistag efficiency measurement, an electron trigger is used. Using an electron trigger allows for a mistag rate measurement of large-R jets with $p_{\mathrm{T}} > 200$ GeV while avoiding trigger bias caused by the jet triggers. To avoid $t\bar{t}$ contamination, offline reconstructed electrons are vetoed. Remaining $t\bar{t}$ contributions are subtracted from the data. For both the top quark tagging and mistag efficiency, the HEPTopTagger proves to be robust against pile-up. The results of these measurements have been published in [85].

The second study presented is a search of new resonances, Z' bosons, decaying to the fully hadronic $t\bar{t}$ final state with the full 2015 dataset (3.2 fb^{-1}) collected by the ATLAS experiment at $\sqrt{s} = 13$ TeV. The HEPTopTagger is used in this search to identify two hadronically decaying top quarks. After top quark identification, the original large-R used by the HEPTopTagger is filtered as described in [79] and used to reconstruct the $m_{t\bar{t}}$ variable. It is shown that this new approach improves the $m_{t\bar{t}}$ resolution significantly. To further increase the top quark purity in the fully hadronic channel, two additional b-tagged jets are required. The b-tagging performance using calorimeter jets is compared to track jets. It is shown that using track jets for b-tagging improves the $m_{t\bar{t}}$ reconstruction efficiency by a factor between 1.3 and 2 and increases $S/\sqrt{B}$ by 40%. The observed $m_{t\bar{t}}$ spectrum is compatible to the Standard Model $t\bar{t}$ and multijet production expectation. Therefore, 95% CL on the cross section times branching fraction are calculated. The

cross section limits translate into a mass exclusion from $0.75 < m_{Z'} < 1.65$ TeV at 95% CL. At the moment of writing, this in the only result existing in the fully hadronic channel within the ATLAS collaboration. The most recent results presented by the CMS collaboration [105] in the $t\bar{t}$ fully hadronic channel achieve a mass exclusion range $1.30 < m_{Z'} < 1.71$ TeV. Finally, using an integrated luminosity of 11.5 fb^{-1} from 2016 dataset, expected mass limits from $0.83 < m_{Z'} < 2.37$ TeV have been evaluated.

The HEPTopTagger proves to be a well established jet substructure technique that can be used for a wide variety of top quark tagging studies. Many improvements are still possible: for example an updated version of the HEPTopTagger, the HEPTopTagger2 is proposed [79]. Among many other improvements, the HEPTopTagger2 adjusts the jet distance parameter of the initial large-R according to the reconstructed top quark candidate mass. The adjustable jet distance parameter allows for a substantial suppression of multijet background at high top quark p_{T}. while keeping a high top quark tagging efficiency. The HEPTopTagger2 offers several options to increase signal efficiency while keeping the background constant. These options should be explored for the future of the fully hadronic $t\bar{t}$ resonance search.

A combination with the $t\bar{t}$ resonance search in lepton+jets channel is in progress and will certainly improve the chances of discovery. The LHC is having an outstanding performance delivering pp collisions at an unprecedented rate. At the moment of writing, the ATLAS detector has recorded an integrated luminosity of 29.3 fb^{-1} [26], approximately 3 times the amount presented in this thesis. The combination of full 2016 and 2016 data sets will greatly increase the discovery potential of New Physics.

Acknowledgements

I am very grateful to Prof. Dr. André Schöning for giving me the opportunity to pursue research in the energy frontier. It is truly a privilege to be able to do research at CERN and something I do not take for granted. Big thanks also to Prof. Dr. Tilman Plehn for the discussion and insights for improving top tagging. I am also very grateful to Dr. Sebastian Schätzel for his patience and guidance during a large period of my master and doctoral thesis. I also want to thank Dr. Gregor Kasieczka. The lessons learned during my master thesis still help me today. I am truly grateful to my great colleagues Dr. Christoph Anders, Dr. Danilo Ferreira, Maddalena Giulini, Dr. Misha Lisovyi, Arthur Bolz, Dr. Rohin Narayan and Mathis Kolb. You have have my period in Heidelberg very enjoyable. Finally, I want to thank my family, Jorge, Imelda, Luis and Andrea. Without their unconditional support I would not have made it.

A Systematic Smoothing

The $m_{t\bar{t}}$ spectra obtained from systematics variations can suffer from statistical fluctuations. An overestimation of uncertainties would result from the large number of systematics considered in this analysis, Moreover, these fluctuations are misleading when the systematics are profiled, and this leads to over-constraint of the nuisance parameters or failure of fitting convergence. A smoothing procedure is applied on all systematics is applied to remedy this issue. In the smoothing procedure, bins with statistically insignificant systematic variations are merged and their average impact is used as a more reliable estimation. A more specific description of the procedure follows. First, loop over all bins on each systematic spectra, starting from the one with largest relative statistical uncertainty. If the systematic variation in the considered bin is smaller than twice of the statistical uncertainty, consider merging this bin with one of its neighbors to improve the statistical significance. Merging with a neighbor bin is done only if the neighbor bin also exhibits insignificant systematic variation or the relatively systematic uncertainty after merging does not exceed twice the statistical uncertainty of current bin. If both neighbor bins meet these criteria, the side with larger relative statistical uncertainty is taken for merging. If this bin has statistically significant systematic variation or if neither of its neighbor bins is good for merging, then skip this bin and move to the bin with next largest relative statistical uncertainty. When a merging occurs, the loop restarts on the new spectra with one less bin than last iteration. The procedure terminated when there is no more bins to merge.

References

[1] "Standard Model. Universität Zürich." http://www.physik.uzh.ch/groups/serra/StandardModel.html.

[2] D. H. Perkins, *Introduction to high-energy physics; 4th ed.* Cambridge Univ. Press, Cambridge, 2000. https://cds.cern.ch/record/396126.

[3] F. Halzen and A. D. Martin, *Quarks and Leptons: an Introductory Course in Modern Particle Physics*. John Wiley, 1984.

[4] "The ATLAS Collaboration. Standard Model PublicResults." https://twiki.cern.ch/twiki/bin/view/AtlasPublic/StandardModelPublicResults. Accessed: 2016-07-06.

[5] "Physics Stack Exchange. Electromagnetic Interaction." http://physics.stackexchange.com/questions/122425/how-do-different-fields-interact-with-each-other.

[6] Particle Data Group Collaboration, K. A. Olive et al., *Review of Particle Physics*, Chin. Phys. **C38** (2014) 090001.

[7] ATLAS Collaboration, *Observation of a new particle in the search for the Standard Model Higgs boson with the ATLAS detector at the LHC*, Phys. Lett. B **716** (2012) 1, arXiv:1207.7214 [hep-ex].

[8] CMS Collaboration, *Observation of a new boson at a mass of 125 GeV with the CMS experiment at the LHC*, Phys. Lett. B **716** (2012) 30, arXiv:1207.7235 [hep-ex].

[9] ATLAS, CDF, CMS, D0 Collaboration, *First combination of Tevatron and LHC measurements of the top-quark mass*, arXiv:1403.4427 [hep-ex].

[10] CDF, D0 Collaboration, B. Stelzer, *Review of Top Quark Measurements*, in *29th International Conference on Physics in Collision (PIC 2009) Kobe, Japan,*

August 30-September 2, 2009. 2010. arXiv:1004.5368 [hep-ex]. https://inspirehep.net/record/853375/files/arXiv:1004.5368.pdf.

[11] "Useful Diagrams of Top Signals and Backgrounds." http://www-d0.fnal.gov/Run2Physics/top/top_public_web_pages/top_feynman_diagrams.html.

[12] ATLAS, CMS Collaboration, T. Golling and o. b. o. t. ATLAS, *LHC searches for physics beyond the Standard Model with top quarks*, J. Phys. Conf. Ser. **452** (2013) 012010, arXiv:1302.0295 [hep-ex].

[13] S. Weinberg, *Implications of Dynamical Symmetry Breaking*, Phys. Rev. **D13** (1976) 974–996.

[14] L. Susskind, *Dynamics of Spontaneous Symmetry Breaking in the Weinberg-Salam Theory*, Phys. Rev. **D20** (1979) 2619–2625.

[15] C. T. Hill and E. H. Simmons, *Strong dynamics and electroweak symmetry breaking*, Phys. Rept. **381** (2003) 235–402, arXiv:hep-ph/0203079 [hep-ph]. [Erratum: Phys. Rept.390,553(2004)].

[16] R. M. Harris, C. T. Hill, and S. J. Parke, *Cross-section for topcolor Z-prime(t) decaying to t anti-t: Version 2.6*, arXiv:hep-ph/9911288 [hep-ph].

[17] C. T. Hill, *Topcolor: Top quark condensation in a gauge extension of the standard model*, Phys. Lett. **B266** (1991) 419–424.

[18] C. T. Hill, *Topcolor assisted technicolor*, Phys. Lett. **B345** (1995) 483–489, arXiv:hep-ph/9411426 [hep-ph].

[19] L. Evans and P. Bryant, *LHC Machine*, JINST **3** (2008) S08001.

[20] J.-L. Caron, "Overall view of LHC experiments.. Vue d'ensemble des experiences du LHC.." AC Collection. Legacy of AC. Pictures from 1992 to 2002., May, 1998.

[21] ALICE Collaboration, K. Aamodt et al., *The ALICE experiment at the CERN LHC*, JINST **3** (2008) S08002.

[22] ATLAS Collaboration, *The ATLAS Experiment at the CERN Large Hadron Collider*, JINST **3** (2008) S08003.

[23] CMS Collaboration, *The CMS experiment at the CERN LHC*, JINST **3** (2008) S08004.

[24] LHCb Collaboration, A. A. Alves, Jr. et al., *The LHCb Detector at the LHC*, JINST **3** (2008) S08005.

[25] F. Marcastel, *CERN's Accelerator Complex. La chaîne des accélérateurs du CERN*,. https://cds.cern.ch/record/1621583. General Photo.

[26] "The atlas collaboration. luminosity public results." https://twiki.cern.ch/twiki/bin/view/AtlasPublic/LuminosityPublicResults. Accessed: 2016-07-06.

[27] "The atlas collaboration. luminosity public results for run2." https://twiki.cern.ch/twiki/bin/view/AtlasPublic/LuminosityPublicResultsRun2. Accessed: 2016-07-06.

[28] M. Lamont, *Status of the LHC*, Journal of Physics: Conference Series **455** no. 1, (2013) 012001. http://stacks.iop.org/1742-6596/455/i=1/a=012001.

[29] "Beam parameters and machine performance to be reached in 2010." http://lhc-commissioning.web.cern.ch/lhc-commissioning/luminosity/MG_2010_parameters.pdf.

[30] "Lhc: The machine." https://www-conf.slac.stanford.edu/ssi/2012/Presentations/Zimmermann.pdf.

[31] G. Brandt, "HERA Physics Feynman Diagram Gallery." http://www.desy.de/~gbrandt/feyn/.

[32] C. Diaconu, *Structure Functions*, Int. J. Mod. Phys. **A24** (2009) 1069–1086, arXiv:0901.0046 [hep-ex].

[33] J. Pumplin et al., *New generation of parton distributions with uncertainties from global QCD analysis*, JHEP **0207** (2002) 012, arXiv:hep-ph/0201195 [hep-ph].

[34] P. M. Nadolsky et al., *Implications of CTEQ global analysis for collider observables*, Phys. Rev. **D 78** (2008) 013004, arXiv:0802.0007 [hep-ph].

[35] G. Watt and R. Thorne, *Study of Monte Carlo approach to experimental uncertainty propagation with MSTW 2008 PDFs*, JHEP **1208** (2012) 052, arXiv:1205.4024 [hep-ph].

[36] NNPDF Collaboration, M. Ubiali, R. D. Ball, L. Del Debbio, S. Forte, A. Guffanti, J. I. Latorre, A. Piccione, and J. Rojo, *Recent progress on NNPDF for LHC*, p. , 32. 2008. arXiv:0805.3100 [hep-ph]. http://inspirehep.net/record/786280/files/arXiv:0805.3100.pdf. [,32(2008)].

[37] ZEUS, H1 Collaboration, F. D. Aaron et al., *Combined Measurement and QCD Analysis of the Inclusive e+- p Scattering Cross Sections at HERA*, JHEP **01** (2010) 109, arXiv:0911.0884 [hep-ex].

[38] B. Andersson et al., *Parton fragmentation and string dynamics*, Phys. Rep. **97** (1983) 31–145.

[39] J.-C. Winter, F. Krauss, and G. Soff, *A Modified cluster hadronization model*, Eur. Phys. J. **C36** (2004) 381–395, arXiv:hep-ph/0311085 [hep-ph].

[40] R. Field, *Min-Bias and the Underlying Event at the LHC*, in *Proceedings, 31st International Conference on Physics in collisions (PIC 2011): Vancouver, Canada, August 28-September 1, 2011*. 2012. arXiv:1202.0901 [hep-ph]. https://inspirehep.net/record/1087901/files/arXiv:1202.0901.pdf.

[41] T. Sjostrand, S. Mrenna, and P. Z. Skands, *PYTHIA 6.4 Physics and Manual*, JHEP **0605** (2006) 026, arXiv:hep-ph/0603175 [hep-ph].

[42] T. Sjostrand, S. Mrenna, and P. Z. Skands, *A Brief Introduction to PYTHIA 8.1*, Comput. Phys. Commun. **178** (2008) 852–867, arXiv:0710.3820 [hep-ph].

[43] ATLAS Collaboration, *ATLAS tunes for Pythia6 and Pythia8 for MC11*, ATLAS-PHYS-PUB-2011-009. http://cdsweb.cern.ch/record/1363300.

[44] ATLAS Collaboration, *Summary of ATLAS Pythia 8 tunes*, ATL-PHYS-PUB-2012-003. http://cdsweb.cern.ch/record/1474107.

[45] G. Corcella et al., *HERWIG 6.5 release note*, arXiv:0210213 [hep-ph].

[46] J. M. Butterworth, J. R. Forshaw, and M. H. Seymour, *Multiparton interactions in photoproduction at HERA*, Z. Phys. C **72** (1996) 637, arXiv:9601371 [hep-ph].

[47] C. Oleari, *The POWHEG-BOX*, Nucl. Phys. Proc. Suppl. **205-206** (2010) 36–41, arXiv:1007.3893 [hep-ph].

[48] S. Frixione and B. R. Webber, *Matching NLO QCD computations and parton shower simulations*, JHEP **06** (2002) 029, arXiv:hep-ph/0204244 [hep-ph].

[49] M. Capeans, G. Darbo, K. Einsweiller, M. Elsing, T. Flick, M. Garcia-Sciveres, C. Gemme, H. Pernegger, O. Rohne, and R. Vuillermet, *ATLAS Insertable B-Layer Technical Design Report*, Tech. Rep. CERN-LHCC-2010-013. ATLAS-TDR-19, CERN, Geneva, Sep, 2010. https://cds.cern.ch/record/1291633.

[50] E. Simioni, S. Artz, B. Bauss, V. Büscher, K. Jakobi, A. Kaluza, C. Kahra, A. Reiss, J. Schäffer, A. Schulte, M. Simon, S. Tapprogge, A. Vogel, M. Zinser, and M. Palka, *Upgrade of the ATLAS Level-1 Trigger with event topology information*, Tech. Rep. ATL-DAQ-PROC-2015-017. 8, CERN, Geneva, May, 2015. https://cds.cern.ch/record/2016644.

[51] GEANT4 Collaboration, *GEANT4: A simulation toolkit*, Nucl. Instrum. Meth. **A 506** (2003) 250.

[52] ATLAS Collaboration, *The simulation principle and performance of the ATLAS fast calorimeter simulation FastCaloSim*, ATL-PHYS-PUB-2010-013. http://cds.cern.ch/record/1300517.

[53] P. Andrade et al., *Distributed monitoring infrastructure for worldwide LHC computing grid*, J. Phys. Conf. Ser. **396** (2012) 032002.

[54] ATLAS Collaboration, *Electron reconstruction and identification efficiency measurements with the ATLAS detector using the 2011 LHC proton–proton collision data*, Eur. Phys. J. C **74** (2014) 2941, arXiv:1404.2240 [hep-ex].

[55] W. Lampl et al., *Calorimeter clustering algorithms: description and performance*, ATL-LARG-PUB-2008-002. http://cdsweb.cern.ch/record/1099735.

[56] ATLAS Collaboration, *Electron and photon energy calibration with the ATLAS detector using LHC Run 1 data*, Eur. Phys. J. C **74** (2014) 3071, arXiv:1407.5063 [hep-ex].

[57] ATLAS Collaboration, G. Aad et al., *Search for $t\bar{t}$ resonances in the lepton plus jets final state with ATLAS using 4.7 fb^{-1} of pp collisions at $\sqrt{s} = 7$ TeV*, Phys. Rev. **D88** no. 1, (2013) 012004, arXiv:1305.2756 [hep-ex].

[58] ATLAS Collaboration, G. Aad et al., *Jet energy measurement with the ATLAS detector in proton-proton collisions at $\sqrt{s} = 7$ TeV*, Eur. Phys. J. **C73** no. 3, (2013) 2304, arXiv:1112.6426 [hep-ex].

[59] ATLAS Collaboration, G. Aad et al., *Topological cell clustering in the ATLAS calorimeters and its performance in LHC Run 1*, arXiv:1603.02934 [hep-ex].

[60] ATLAS Collaboration, "Commissioning of the ATLAS high performance b-tagging algorithms in the 7 TeV collision data." ATLAS-CONF-2011-102, 2011. http://cdsweb.cern.ch/record/1369219.

[61] ATLAS Collaboration, "Performance and Calibration of the JetFitterCharm Algorithm for c-Jet Identification." ATL-PHYS-PUB-2015-001, 2015. http://cdsweb.cern.ch/record/1980463.

[62] ATLAS Collaboration, "Expected performance of the ATLAS b-tagging algorithms in Run-2." ATL-PHYS-PUB-2015-022, 2015. http://cdsweb.cern.ch/record/2037697.

[63] ATLAS Collaboration, "Flavor Tagging with Track-Jets in Boosted Topologies with the ATLAS Detector." ATL-PHYS-PUB-2014-013, 2014. https://atlas.web.cern.ch/Atlas/GROUPS/PHYSICS/PUBNOTES/ATL-PHYS-PUB-2014-013.

[64] "B Tagging Benchmarks." https://twiki.cern.ch/twiki/bin/view/AtlasProtected/BTaggingBenchmarks#MV2c20_tagger_AntiKt2PV0TrackJet. Accessed: 2016-06-28.

[65] ATLAS Collaboration, "Performance of Missing Transverse Momentum Reconstruction in ATLAS studied in Proton–Proton Collisions recorded in 2012 at $\sqrt{s} = 8$ TeV." ATLAS-CONF-2013-082, 2013. http://cdsweb.cern.ch/record/1570993.

[66] G. P. Salam, *Towards Jetography*, Eur. Phys. J. **C67** (2010) 637–686, arXiv:0906.1833 [hep-ph].

[67] M. Cacciari, G. P. Salam, and G. Soyez, *FastJet User Manual*, Eur. Phys. J. **C 72** (2012) 1896, arXiv:1111.6097 [hep-ph].

[68] S. Catani, Y. L. Dokshitzer, M. Seymour, and B. Webber, *Longitudinally invariant K_t clustering algorithms for hadron hadron collisions*, Nucl.Phys. **B406** (1993) 187–224.

[69] M. Wobisch and T. Wengler, *Hadronization corrections to jet cross sections in deep- inelastic scattering*, arXiv:hep-ph/9907280 [hep-ph].

[70] M. Wobisch, *Measurement and QCD analysis of jet cross sections in deep inelastic positron proton collisions at s = 300 GeV*, Tech. Rep. PITHA 00/12, Aachen, 2000. Zugl.: Aachen, Techn. Hochsch., Diss., 2000.

[71] M. Cacciari, G. P. Salam, and G. Soyez, *The anti-k_t jet clustering algorithm*, JHEP **04** (2008) 063, arXiv:0802.1189 [hep-ph].

[72] A. Altheimer et al., *Jet Substructure at the Tevatron and LHC: New results, new tools, new benchmarks*, J. Phys. **G39** (2012) 063001, arXiv:1201.0008 [hep-ph].

[73] E. Thompson, "BOOST!." http://www.quantumdiaries.org/2012/08/05/boost/.

[74] J. M. Butterworth et al., *Jet substructure as a new Higgs search channel at the LHC*, Phys. Rev. Lett. **100** (2008) 242001, arXiv:0802.2470 [hep-ph].

[75] D. Krohn, J. Thaler, and L.-T. Wang, *Jet Trimming*, JHEP **02** (2010) 084, arXiv:0912.1342 [hep-ph].

[76] ATLAS Collaboration, *Performance of jet substructure techniques for large-R jets in proton–proton collisions at $\sqrt{s} = 7$ TeV using the ATLAS detector*, JHEP **1309** (2013) 076, arXiv:1306.4945 [hep-ex].

[77] ATLAS Collaboration, *Performance of jet substructure techniques for large-R jets in proton-proton collisions at $\sqrt{s} = 7$ TeV using the ATLAS detector*, JHEP **1309** (2013) 076, arXiv:1306.4945 [hep-ex].

[78] T. Plehn et al., *Stop Reconstruction with Tagged Tops*, JHEP **10** (2010) 078, arXiv:1006.2833 [hep-ph].

[79] G. Kasieczka, T. Plehn, T. Schell, T. Strebler, and G. P. Salam, *Resonance Searches with an Updated Top Tagger*, JHEP **06** (2015) 203, arXiv:1503.05921 [hep-ph].

[80] A. Altheimer et al., *Jet Substructure at the Tevatron and LHC: New results, new tools, new benchmarks*, J. Phys. **G 39** (2012) 063001, arXiv:1201.0008 [hep-ph].

[81] C. Anders, "Projects." http://www.physi.uni-heidelberg.de/Forschung/he/ATLAS/projects/.

[82] J. M. Butterworth, B. E. Cox, and J. R. Forshaw, *WW scattering at the CERN LHC*, Phys. Rev. **D 65** (2002) 096014, arXiv:hep-ph/0201098 [hep-ph].

[83] J. Thaler and K. Van Tilburg, *Identifying Boosted Objects with N-subjettiness*, JHEP **03** (2011) 015, arXiv:1011.2268 [hep-ph].

[84] J. Thaler and K. Van Tilburg, *Maximizing Boosted Top Identification by Minimizing N-subjettiness*, JHEP **02** (2012) 093, arXiv:1108.2701 [hep-ph].

[85] ATLAS Collaboration, G. Aad et al., *Identification of high transverse momentum top quarks in pp collisions at $\sqrt{s}$ = 8 TeV with the ATLAS detector*, JHEP **06** (2016) 093, arXiv:1603.03127 [hep-ex].

[86] ATLAS Collaboration, *Improved luminosity determination in pp collisions at $\sqrt{s} = 7$ TeV using the ATLAS detector at the LHC*, submitted to Eur. Phys. J. (2013), arXiv:1302.4393 [hep-ex].

[87] ATLAS Collaboration, "Performance of primary vertex reconstruction in proton–proton collisions at $\sqrt{s} = 7$ TeV in the ATLAS experiment." ATLAS-CONF-2010-069, 2010. http://cdsweb.cern.ch/record/1281344.

[88] ATLAS Collaboration, *Jet energy measurement and its systematic uncertainty in proton–proton collisions at $\sqrt{s} = 7$ TeV with the ATLAS detector*, Eur. Phys. J. C **75** (2015) 17, arXiv:1406.0076 [hep-ex].

[89] ATLAS Collaboration, "Electron efficiency measurements with the ATLAS detector using the 2012 LHC proton–proton collision data." ATLAS-CONF-2014-032, 2014. http://cdsweb.cern.ch/record/1706245.

[90] CMS Collaboration, C. Collaboration, *Top Tagging with New Approaches*,.

[91] ATLAS Collaboration, "Search for heavy particles decaying to pairs of highly-boosted top quarks using lepton-plus-jets events in proton-–proton collisions at $\sqrt{s} = 13$ TeV with the ATLAS detector." ATLAS-CONF-2016-014, 2016. http://cdsweb.cern.ch/record/2141001.

[92] ATLAS Collaboration, *Search for resonances decaying into top-quark pairs using fully hadronic decays in pp collisions with ATLAS at* $\sqrt{s} = 7$ *TeV*, JHEP **1301** (2013) 116, arXiv:1211.2202 [hep-ex].

[93] CMS Collaboration, V. Khachatryan et al., *Search for resonant* $t\bar{t}$ *production in proton-proton collisions at* $\sqrt{s} = 8$ TeV, Phys. Rev. **D93** no. 1, (2016) 012001, arXiv:1506.03062 [hep-ex].

[94] G. Kasziecska, *Search for Resonances Decaying into Top Quark Pairs Using Fully Hadronic Decays in pp Collisions with ATLAS at* $\sqrt{s} = 7$ TeV. PhD thesis, University of Heidelberg, 2013.

[95] ATLAS Collaboration, "Measurement of the Mistag Rate of b-tagging algorithms with 5 fb^{-1} of Data Collected by the ATLAS Detector." ATLAS-CONF-2012-040, 2012. http://cdsweb.cern.ch/record/1435194.

[96] ATLAS Collaboration, "Calibration of b-tagging using dileptonic top pair events in a combinatorial likelihood approach with the ATLAS experiment." ATLAS-CONF-2014-004, 2014. http://cdsweb.cern.ch/record/1664335.

[97] ATLAS Collaboration, "Measuring the b-tag efficiency in a $t\bar{t}$ sample with 4.7 fb^{-1} of data from the ATLAS detector." ATLAS-CONF-2012-097, 2012. http://cdsweb.cern.ch/record/1460443.

[98] "b-tagging calibration plots using dileptonic tt events produced in pp collisions at sqrts=13 TeV and a combinatorial likelihood approach." http://atlas.web.cern.ch/Atlas/GROUPS/PHYSICS/PLOTS/FTAG-2016-002/.

[99] ATLAS Collaboration, M. Aaboud et al., *Luminosity determination in pp collisions at $\sqrt{s}$ = 8 TeV using the ATLAS detector at the LHC*, arXiv:1608.03953 [hep-ex].

[100] M. Botje, J. Butterworth, A. Cooper-Sarkar, A. de Roeck, J. Feltesse, et al., *The PDF4LHC Working Group Interim Recommendations*, arXiv:1101.0538 [hep-ph].

[101] J. Butterworth et al., *PDF4LHC recommendations for LHC Run II*, J. Phys. **G43** (2016) 023001, arXiv:1510.03865 [hep-ph].

[102] R. D. Ball, L. Del Debbio, S. Forte, A. Guffanti, J. I. Latorre, J. Rojo, and M. Ubiali, *A first unbiased global NLO determination of parton distributions and their uncertainties*, Nucl. Phys. **B838** (2010) 136–206, arXiv:1002.4407 [hep-ph].

[103] J. H. Kühn, A. Scharf, and P. Uwer, *Weak Interactions in Top-Quark Pair Production at Hadron Colliders: An Update*, Phys. Rev. **D91** no. 1, (2015) 014020, arXiv:1305.5773 [hep-ph].

[104] O. Behnke, K. Kröninger, T. Schörner-Sadenius, and G. Schott, eds., *Data analysis in high energy physics*. Wiley-VCH, Weinheim, Germany, 2013. http://www.wiley-vch.de/publish/dt/books/ISBN3-527-41058-9.

[105] CMS Collaboration Collaboration, *Search for top quark-antiquark resonances in the all-hadronic final state at sqrt(s)=13 TeV*, Tech. Rep. CMS-PAS-B2G-15-003, CERN, Geneva, 2016. https://cds.cern.ch/record/2160237.